

UC San Diego

UC San Diego Electronic Theses and Dissertations

Title

Probing the Structure, Organization, and Oligomerization of Biomolecular Ligands on Silica Surfaces with an Emphasis in Origin of Life

Permalink

<https://escholarship.org/uc/item/61n7w8mn>

Author

Swanson, Haley

Publication Date

2022

Peer reviewed|Thesis/dissertation

UNIVERSITY OF CALIFORNIA SAN DIEGO

SAN DIEGO STATE UNIVERSITY

Probing the Structure, Organization, and Oligomerization of Biomolecular Ligands on Silica
Surfaces with an Emphasis in Origin of Life

A dissertation submitted in partial satisfaction of the
requirements for the degree Doctor of Philosophy

in

Chemistry

by

Haley Laurent Swanson

Committee in charge:

University of California San Diego

Professor Michael K. Gilson
Professor Ulrich Friedrich Muller
Professor Wei Xiong

San Diego State University

Professor Gregory P. Holland, Chair
Professor Diane Smith

2022

The dissertation of Haley Laurent Swanson is approved, and it is acceptable in quality and form for publication on microfilm and electronically:

Chair

University of California San Diego

San Diego State University

2022

Dedication

To my parents, Bob and Michele Swanson, who encouraged me to go to college and helped me afford my dream school. To my undergraduate advisor, Dr. Steven Hendrix, who encouraged me to “tackle the beast” and seek the ultimate academic challenge. And to my husband, Omar Diaz, whose never ending support, belief, and occasional teasing is the reason why I finished.

Epigraph

Remember to look up at the stars and not down at your feet. Try to make sense of what you see, and wonder about what makes the universe exist. Be curious.

– Stephen Hawking

Table of Contents

Dissertation Approval Page.....	iii
Dedication.....	iv
Epigraph.....	v
Table of Contents.....	vi
List of Abbreviations.....	ix
List of Figures.....	x
List of Tables.....	xiv
Acknowledgements.....	xv
Vita.....	xvi
Abstract of the Dissertation.....	xvii
Chapter 1 Introduction.....	1
Silica	2
Surface chemistry of silica.....	6
Origin of life.....	8
Techniques.....	9
References.....	25
Chapter 2 Probing the binding modes and dynamics of histidine on fumed silica surfaces by solid-state NMR.....	34
Abstract.....	35
Introduction.....	36
Experimental.....	38
Results and Discussion.....	44
Conclusions.....	67

Acknowledgements.....	68
Supplemental Information.....	69
References.....	76
Chapter 3 The impact of metal doping on fumed silica structure and amino acid thermal condensation catalytic properties.....	82
Abstract.....	83
Introduction.....	84
Experimental.....	85
Results and Discussion.....	90
Conclusions.....	105
Acknowledgements.....	106
Supplemental Information.....	107
References.....	108
Chapter 4 Assembly and thermal-induced polymerization of histidine on fumed silica surfaces.....	113
Abstract.....	114
Introduction.....	115
Experimental.....	117
Results.....	122
Discussion.....	137
Conclusions.....	143
Acknowledgements.....	145
Supplemental Information.....	145
References.....	150

Chapter 5 Future direction in prebiotic systems.....	154
Introduction.....	155
Experimental.....	158
Results and Discussion.....	162
Conclusions.....	170
Future directions.....	171
Acknowledgements.....	172
References.....	173

List of Abbreviations

°C	Degree Celsius
3MR	3-membered ring
4MR	4-membered ring
Al	Aluminum
Ala	Alanine
B ₀	External magnetic field
CP-MAS	Cross polarization magic angle spinning
CTAB	N-Cetyltrimethylammonium bromide
d1	Recycle delay
D ₂ O	Deuterium oxide
DFT	Density functional theory
DI	Deionized water
DP-MAS	Direct polarization magic angle spinning
DTG	First derivative thermogravimetric analysis
FSN	Fumed silica nanoparticles
FWHM	Full width at half maximum
HETCOR	Heteronuclear correlation
His	Histidine
HisHClH ₂ O	Histidine monohydrochloride monohydrate
HPLC	High-performance liquid chromatography
Hz	Hertz
kHz	Kilohertz
L	Liter
MAS	Magic angle spinning
mg	Milligram
MHz	Megahertz
mL	Milliliter
MS	Mass spectrometry
MSN	Mesoporous silica nanoparticles
NASA	National Aeronautics and Space Administration
nm	nanometer
NMR	Nuclear magnetic resonance
ppm	Parts per million
ROS	Reactive oxygen species
rf	Radio frequency
SSNMR	Solid-state nuclear magnetic resonance
sw	Sweep width
TEM	Transmission electron microscopy
TEOS	Tetraethyl orthosilicate
TGA	Thermogravimetric analysis
Ti	Titanium
UV	Ultraviolet
μL	Microliter

List of Figures

Figure 1.1. TEM imaging of synthetic and naturally occurring silica nanostructures.....	3
Figure 1.2. Schematic of fumed silica nanoparticle synthesis.....	4
Figure 1.3. Silicon coordination environments. The number in the subscript represents the number of bridging siloxane bonds.....	7
Figure 1.4. TGA and DTG curves for Ala on FSN with a thermal condensation schematic.....	10
Figure 1.5. Total electric and magnetic effects and their relative contributions that arise when NMR active nuclei interact with B_0	14
Figure 1.6. ^1H MAS SSNMR of MgAl-33 at different spinning speeds to highlight the power of MAS.....	15
Figure 1.7. SSNMR pulse sequences for direct-polarization magic angle spinning and cross-polarization magic angle spinning.....	17
Figure 1.8. Nuclear shape and Zeeman energy splitting for (left) $I = \frac{1}{2}$ and (right) $I > \frac{1}{2}$ nuclei...	19
Figure 1.9. ^{27}Al DP-MAS of γ -alumina with tetrahedral and octahedral coordination sites.....	20
Figure 1.10. Diffusion NMR data and fit for measuring free diffusion of His in water at various concentrations.....	22
Figure 1.11. (top) Depicts accuracy of approximating STOs with GTOs. (bottom) Example of Pople-style basis set nomenclature and total functions.....	24
Figure 2.1. Free His conformations and adsorbed His – FSN models as a function of concentration.....	45
Figure 2.2. DTG curves of free and adsorbed His as a function of concentration.....	47
Figure 2.3. ^{13}C and ^{15}N CP-MAS of free and adsorbed His in 2 protonation states, hydrated.....	49
Figure 2.4. ^{13}C DP-MAS of adsorbed His in 2 protonation states with decoupling and MAS switched on/off, hydrated.....	52
Figure 2.5. ^{13}C and ^{15}N CP-MAS and DP-MAS with short recycle delay of adsorbed His in 2 protonation states, hydrated.....	56
Figure 2.6. ^{13}C and ^{15}N CP-MAS and DP-MAS of adsorbed His at pH 4 in hydrated & dried environments with deconvolution.....	58

Figure 2.7. ^{13}C and ^{15}N CP-MAS and DP-MAS of amorphous and adsorbed His at pH 7.6 in hydrated & dried environments with deconvolution.....	63
Figure 2.8. $^1\text{H} - ^{13}\text{C}$ and $^1\text{H} - ^{15}\text{N}$ HETCOR of adsorbed His at pH 7.6 in hydrated & dried environments with corresponding ^1H slices.....	65
Figure 2.9. Proposed model of His – FSN interactions in 2 protonation states, in hydrated & dried environments.....	66
Figure 2.S1. TGA and DTG curves of His/FSN adsorptions at pH 7.6 using natural abundance L-histidine·HCl·H ₂ O (fully protonated crystal) or L-histidine (neutral powder)	70
Figure 2.S2. ^1H NMR of HisHCl untreated and HisHCl after 24 h heating at 165 °C.....	71
Figure 2.S3. DFT His models with N – H perturbations and resulting NMR chemical shift calculations. The calculated ^{15}N chemical shift is plotted as a function of N – H bond length.....	72
Figure 2.S4. Data processing and direct polarization pulse sequence of the ^{13}C saturation recovery experiment used to selectively measure T_1 of the adsorbed layer.....	74
Figure 2.S5. Full spectrum $^1\text{H} - ^{15}\text{N}$ and $^1\text{H} - ^{13}\text{C}$ HETCOR of U-His/FSN-7.6 in the hydrated state.....	74
Figure 2.S6. Full spectrum $^1\text{H} - ^{15}\text{N}$ and $^1\text{H} - ^{13}\text{C}$ HETCOR of U-His/FSN-7.6 in the dried state.....	75
Figure 2.S7. Variable contact $^1\text{H} - ^{13}\text{C}$ HETCOR of U-His/FSN-7.6 in the hydrated state. Corresponding ^1H slices and intermolecular interactions are illustrated that provide strong evidence for horizontal arrangement of His on FSN.....	75
Figure 3.1. ^{29}Si CP-MAS NMR of Al- and Ti-doped samples with 0%FSN.....	89
Figure 3.2. ^{29}Si DP-MAS NMR of Al- and Ti-doped samples with 0%FSN.....	94
Figure 3.3. ^{27}Al DP-MAS NMR of Al-doped samples collected at 15 kHz MAS with a recycle delay of a) 0.25 sec and b) variable delay.....	97
Figure 3.4. ^{27}Al CP-MAS NMR of 10% Al- doped samples after heating and rehydration.....	98
Figure 3.5. Raman spectra of 0%FSN and Ti-doped FSN.....	100
Figure 3.6. DTG curves of 0%FSN and a) Al- and b) Ti-doped FSN with 0.10M Ala adsorbed.....	103
Figure 3.S1. Raman spectra of 0%FSN and Al-doped FSN.....	107

Figure 3.S2. Thermograms of 0.10M ala adsorbed on 0%FSN, Al-doped FSN, and Ti-doped FSN.....	107
Figure 4.1. Free His model and ¹ H solution NMR of His/FSN thermal condensation products after various heating times at 160 °C.....	123
Figure 4.2. His DKP model and ¹ H – ¹ H TOCSY of His/FSN thermal condensation product after 24 hr thermal treatment at 160 °C.....	124
Figure 4.3. ¹ H NMR of free His and thermal condensation products after 24 hr at 160 °C and 3 hr at 200 °C.....	126
Figure 4.4. His DKP and linear 3D conformations derived from DFT computational modeling.....	129
Figure 4.5. ¹ H NMR of free His and His/FSN after various low temperature thermal treatments. Grey traces are scaled 500% to display presence of minor product peaks.....	133
Figure 4.6. DTG of His/FSN at pH 7.6 in hydrated and dried conditions.....	134
Figure 4.7. DTG of His/FSN adsorptions at pH 4, pH 7.6, and pH 10 as a function of His loading.....	136
Figure 4.8. DTG curves of various amino acids adsorbed on FSN at 0.05M.....	140
Figure 4.S1. ¹ H – ¹⁵ N HMBC of the His DKP thermal condensation product created after 24 hr heating on FSN at 160 °C.....	145
Figure 4.S2. (top) ¹⁵ N and ¹³ C CP-MAS of His/FSN before and after thermal treatments. (bottom) HPLC of thermal condensation products after 160 °C/3 hr and 200 °C/3 hr.....	146
Figure 4.S3. MS-ESI Direct injection of the fraction-collected product peak after 160 °C/24 hr.....	147
Figure 4.S4. Diffusion coefficients calculated from diffusion NMR experiments vs concentration.....	148
Figure 4.S5. ¹ H NMR spectra of isothermal vs ramped thermal treatments on His/FSN-0.05M adsorptions performed for method validation.....	149
Figure 5.1. DTG of L-ala adsorbed on various silica substrates at 0.05M concentration.....	156
Figure 5.2. (top) DTG thermograms of β-ala/FSN-0.03M, L-ala/FSN-0.03M, and mixed (1:1) β/L-ala/FSN at 0.03M each. (bottom) Thermal condensation schemes of each reaction.....	163
Figure 5.3. DTG thermograms using a slow (1 °C/min) ramp rate.....	164

Figure 5.4. (left) ^{13}C and (right) ^{15}N CP-MAS of free β -ala and FSN adsorptions before and after thermal treatments.....	165
Figure 5.5. $^1\text{H} - ^{13}\text{C}$ HSQC and $^1\text{H} - ^{13}\text{C}$ HMBC of β -ala/FSN after 135 $^\circ\text{C}/21$ hr.....	166
Figure 5.6. (left) ^{13}C and (right) ^{15}N CP-MAS SSNMR of free β -ala and FSN adsorptions before and after thermal treatments.....	168
Figure 5.7. ^1H NMR of free β -ala, L-ala, L-ala DKP, and thermal condensation products.....	169
Figure 5.8. $^1\text{H} - ^1\text{H}$ COSY of β /L-ala/FSN after heating at 140 $^\circ\text{C}/21$ hr.....	169

List of Tables

Table 1.1. NMR active nuclei and spin properties.....	18
Table 2.1. ^{13}C and ^{15}N solution and SSNMR chemical shifts (reported in ppm) of free and adsorbed His in 2 protonation states.....	50
Table 2.2. ^{13}C solid and solution state T_1 relaxation (reported in seconds) of free and adsorbed His in 2 protonation states.....	54
Table 2.3. ^{13}C and ^{15}N SSNMR chemical shifts (reported in ppm) of adsorbed His in 2 protonation states, hydrated and dried.....	61
Table 2.S1. Sample abbreviations and preparation methods.....	69
Table 2.S2. NMR computational results from DFT calculations of His models with N – H perturbations.....	73
Table 3.1. ^{29}Si CP-MAS SSNMR data for doped samples.....	92
Table 3.2. ^{29}Si Q_4 isotropic chemical shift from DP-MAS and predicted Si-O-T bond angle calculated from the equation derived by Smith & Blackwell ¹	95
Table 3.3. BET analysis and TGA calculations.....	102
Table 4.1. ^1H NMR chemical shifts, molecular radius, and energy of theoretical conformers predicted by DFT, experimental His DKP after 24 hr thermal treatment, and literature values...	130
Table 5.1. Prebiotic molecules to be investigated in future research (Y = Yes, N = No, R = Racemic).....	158

Acknowledgements

I would like to acknowledge Professor Greg Holland, Dr. Lynn Rothschild, Dr. J. Bennett Addison, Professor Chengchen Guo, and for their continual support and guidance. Without them, I wouldn't have made it this far. I would also like to acknowledge support from NASA Fellowship 80NSSC19K0064 which funded the last 3 years of my research and provided support for personal development seminars and scientific conferences.

Chapter 2, in full, is a reprint of the material as it appears published by Royal Society of Chemistry in the journal of Physical Chemistry Chemical Physics 2020. The dissertation author Haley L. Swanson was the primary investigator and author of this paper. Supporting authors include Chengchen Guo, Michael Cao, J. Bennett Addison, and Gregory P. Holland.

Chapter 3, in full, is a reprint of the material as it appears published by Springer in the Journal of Materials Science 2021. The dissertation author Haley L. Swanson was the primary investigator and author of this paper. Supporting authors include Suman Pokhrel, Stephen K. Davidowski, Lutz Mädler, C. Jeffrey Brinker, and Gregory P. Holland.

Chapter 4, in full, has been submitted for publication as it may appear in ACS Earth and Space Chemistry 2022. The dissertation author Haley L. Swanson was the primary investigator and author of this material. Supporting authors include Elizabeth A. Couri, Christian James P. Sabando, and Gregory P. Holland.

Vita

Education

- 2021 Doctor of Philosophy in Chemistry
University of California San Diego, San Diego State University
- 2013 Bachelor of Science in Chemistry
University of Tampa

Awards

- 2018 – 2020 NASA MUREP Research Fellowship
Awarded by National Aeronautics & Space Administration
- 2015 Graduate Student Travel Fund Award
Awarded by San Diego State University
- 2009 – 2013 Dean's Scholarship for Academics
Awarded by University of Tampa

Publications

Swanson, H. L., Holland, G. P. "Thermal condensation of β -alanine and L-alanine on fumed silica" (in preparation)

Swanson, H. L., Couri, E. A., Sabando, C. J. P., Holland, G. P. "Assembly and thermal-induced polymerization of histidine on fumed silica surfaces" *ACS Earth Space Chem.*, 2022, **submitted**

Swanson, H. L., Pokhrel, S., Davidowski, S. K., Mädler, L., Brinker, C. J., Holland, G.P. "The impact of metal doping on fumed silica structure and amino acid thermal condensation catalytic properties" *J. Mater. Sci.*, 2021, **56**, 16916

Swanson, H. L., Guo, C., Cao, M., Addison, J. B., Holland, G.P. "Probing the binding modes and dynamics of histidine on fumed silica surfaces by solid-state NMR" *Phys. Chem Chem. Phys.*, 2020, **22**, 20349

ABSTRACT OF THE DISSERTATION

Probing the Structure, Organization, and Oligomerization of Biomolecular Ligands on Silica Surfaces with an Emphasis in Origin of Life

by

Haley Laurent Swanson

Doctor of Philosophy in Chemistry

University of California San Diego, 2022
San Diego State University, 2022

Professor Gregory Holland, Chair

Nanotechnology is an integral part of advancements in material science and biomedical devices. The surface of nanomaterials govern how they behave in various media and what properties they possess. Decades of research have gone into fine tuning nanomaterial production for various applications, but the fundamental understanding of the chemistry that occurs at the interface is surprisingly underdeveloped. Achieving atomic-level resolution is possible with few analytical techniques. Systems that are amorphous and/or dynamic are even more challenging to characterize. Solid-state nuclear magnetic resonance is a vital tool capable of bridging this gap. The work presented in this dissertation has three objectives: (1) understand how different biomolecular ligands organize on the surface of silica nanoparticles (2) characterize structural

differences among silica nanomaterials, and (3) apply these techniques to prebiotic systems to investigate possible avenues of chemical evolution and the origin of life on Earth.

Silica, or SiO_2 , was selected as the focus of this investigation because it is ubiquitous in natural and synthetic forms. Synthetic SiO_2 is widely used for industrial and biomedical applications due to high surface area, tunable features, and biocompatibility. Natural polymorphs of SiO_2 are the primary minerals in the Earth's crust. Many origins of life researchers have explored the role of silica-based clays in prebiotic reactions, but the impact of other amorphous silica forms is far less developed. Investigating the relationship between biomolecular ligands and amorphous SiO_2 is the focus of this dissertation as it applies to our fundamental understanding in advancements for industrial and biomedical applications and also evaluating the potential impact of amorphous SiO_2 in directing the self-assembly and oligomerization of small molecules in prebiotic conditions.

Chapter 1

Introduction

Silica

The research presented in this dissertation seeks to gain a fundamental understanding of molecular assembly and oligomerization of amino acids on silica nanostructured surfaces. Atomic-level resolution is required to identify site-specific interactions that occur at an interface between substrate and ligand. Silica (SiO_2) was selected as the substrate for this investigation for its ubiquity in our world today. SiO_2 is the most abundant inorganic oxide in the Earth's crust^{1, 2} and exists in many natural and synthetic morphologies. See **Figure 1.1** for microscopy imaging of silica substrates that were analyzed during the course of this research. This dissertation analyzes the interactions between amino acids and SiO_2 with two backgrounds in mind. First, understanding how the presence of synthetic silica nanoparticles influences biochemistry is a primary concern for evaluating their potential in biomedical advancements and evaluating health and safety concerns from exposure and consumption. Fumed silica nanoparticles (FSN), discussed below, are generally recognized as safe (GRAS) by the Food and Drug Administration (FDA) despite documented cytotoxicity and inflammatory responses.³⁻⁶ This sets the stage for the work described in Chapter 3. Second, silica exhibits catalytic properties that may have played a key role in directing prebiotic chemical reactions. The Miller-Urey experiments demonstrated that amino acids readily form from the condensation of organic gases and electricity and their presence in the prebiotic time period is widely accepted.⁷ Over half of Earth's crust is composed of silica-based minerals so it is logical to think that prebiotic interactions between silica and amino acids must have occurred.^{1, 2} In 1951, Bernal first suggested that silicate clays have the ability to concentrate and assemble organic molecules in otherwise dilute solutions and may have played a key role in early polymerization processes.⁸ Lahav et al in 1978 demonstrated that wet-dry temperature cycles provide enough energy to polymerize amino acids on clay surfaces,⁹ and this phenomenon has

been explored extensively. With these backgrounds in mind, three main objectives are presented that direct the focus of this dissertation: (1) characterize ligand assembly on SiO₂ nanoparticles with various perturbations, (2) characterize structural differences and surface reactivities among amorphous silica morphologies, and (3) apply these techniques to prebiotically relevant systems to explore possible avenues of chemical evolution.

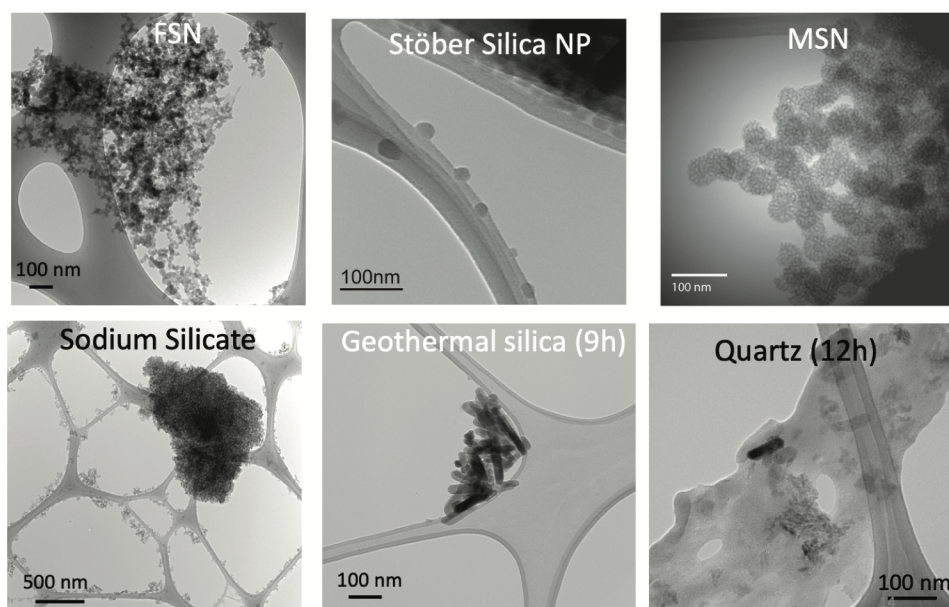


Figure 1.1. Transmission electron microscopy (TEM) imaging of silica nanostructures displaying clear differences in morphology. (top) Common synthetic SiO₂ nanoparticles and (bottom) naturally occurring SiO₂ substrates have been studied over the course of this work. Geothermal silica and quartz were homogenized by ball milling and the length of time the sample was milled is indicated in parenthesis.

Silica nanoparticles are used in this investigation because they provide a sufficient model for natural, amorphous archetypes (i.e. glasses) with an incredibly high surface area which facilitates the analysis of small molecule interactions on the surfaces. During my research, I analyzed 3 common synthetic SiO₂ nanoparticles: fumed, Stöber, and mesoporous silica (MSN).

Fumed (or pyrolytic) silica is produced through a rapid process of SiCl_4 combustion and quenching (**Figure 1.2**). In contrast, Stöber (or colloidal) silica nanoparticles are synthesized by the controlled hydrolysis of a silica precursor, usually tetraethyl orthosilicate (TEOS), in an alcoholic solution containing water and ammonia.^{10, 11} These mild conditions produce a colloidal suspension containing spherical silica nanoparticles with a tunable, narrow size distribution and stable amorphous siloxane network.^{12, 13} Similarly, MSN are produced by a modified Stöber method that includes a surfactant templating agent. The surfactants self-assemble in solution and the silica precursor co-condenses around the template, creating an ordered, tunable porous structure.¹⁴⁻¹⁷ While Stöber and MSN have been influential in the development of nanocomposites in medicine and biotechnology, only studies done on FSN are included in this dissertation for reasons discussed below.

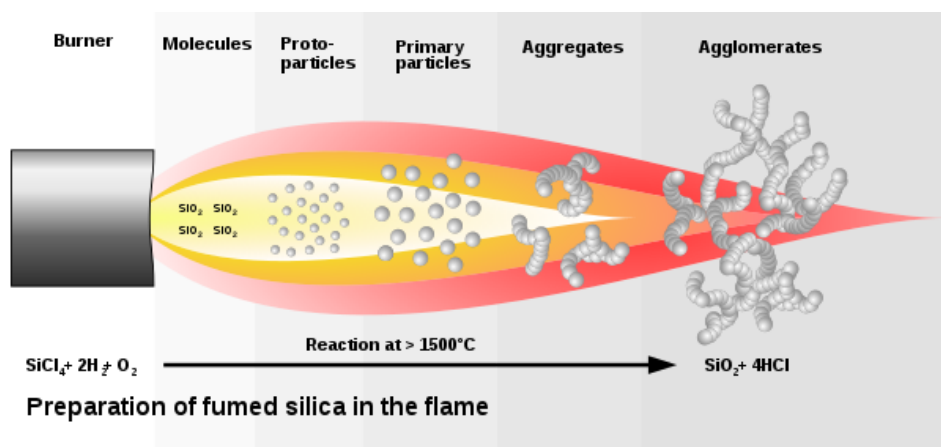


Figure 1.2. Schematic of fumed silica nanoparticle synthesis.¹⁸

FSN have a highly disordered amorphous siloxane network that aggregates in three-dimensional (3D) branch-like structures (**Figure 1.1**).¹⁹ Quenching takes place over a few milliseconds which locks in unfavorable surface siloxane conformations. The siloxane network contains populations of strained 3 and 4 membered rings (3MR and 4MR, respectively) made up of reactive oxygen species (ROS) that easily cleave to form radicals.⁵ It is hypothesized that these strained ring defects and radicals are the source of undesirable biochemical reactions upon exposure such as apoptosis, cytotoxicity, and pro-inflammatory responses.^{3, 5, 6, 20} FSN have also demonstrated the ability to catalyze peptide bonds with high efficiency compared to their sol-gel synthesized colloidal counterparts.²¹⁻²⁴ The exact mechanism for this is unclear but is hypothesized to be the result of high surface area, ROS, aggregation-prone qualities, or a combination of these properties.

FSN can be found in everything from paint and cement to toothpaste and pharmaceuticals.²⁵ The fumed silica market has been steadily growing and is projected to be worth over \$2.3 billion by the year 2027.²⁶ As an additive, FSN improves physical properties of materials such as durability, stability, shelf life, and consistency. It is the efficacy as an additive combined with the low cost of manufacturing that makes FSN an attractive option for foods, beverages, and personal care items despite the toxicity effects stated above. Because FSN is so common worldwide and produced at such a large scale, substitutes and alternative production methods are being explored to ameliorate the unintended biochemical responses. One promising alternative is the inclusion of metal doping during pyrolysis which is detailed in Chapter 3.

Surface chemistry of silica

The bulk of silica nanoparticles is composed of a repeating network of silicon-oxygen rings with varying bond angle. The termination of these substrates play a key role in directing its function and behavior and can be modified to promote various interactions like controlled drug release, cellular uptake, hydrophobic/hydrophilic binding, etc.^{12, 27, 28} Silicon environments at the surface can exist in three types of coordination, shown in **Figure 1.3**: geminal silanols (Q_2), vicinal silanols (Q_3), or siloxane bridges (Q_4) which are easily distinguishable by ^{29}Si magic angle spinning (MAS) solid-state nuclear magnetic resonance (SSNMR).^{28, 29} The surplus of hydroxyls creates a hydrophilic, biocompatible layer with many potential binding sites for organic and biomolecular ligands. The total surface area combined with the number of hydroxyls/nm² gives an indication of the total available binding sites. A hydrophobic interface can be created through simple dehydration to remove hydroxyls and increase Q_4 populations at the surface^{28, 29} or by functionalizing the surface with hydrophobic molecules.^{12, 30, 31} This has become incredibly important in the efficacy as drug delivery vehicles for drug loading and cellular uptake, but will not be discussed further in this dissertation.

Reactivity is an important consideration in evaluating SiO_2 in biological context and can be indicated by the disorder of the silanols and siloxane bonds near the surface. Exposure to high heat and rehydration causes the interface groups to condense and/or cleave, which can generate a variety of different oxyradical species.⁵ FSN contains a high population of strained 3MR and 4MR which readily cleave to form radicals on the surface.⁵ Stöber colloidal silica exhibits strained 3MR only after thermal treatments $>600\text{ }^\circ\text{C}$.^{3, 5, 20} We hypothesize that it is the population of 3MR and 4MR defects or ROS generation that create the highly reactive surface inherent to FSN.

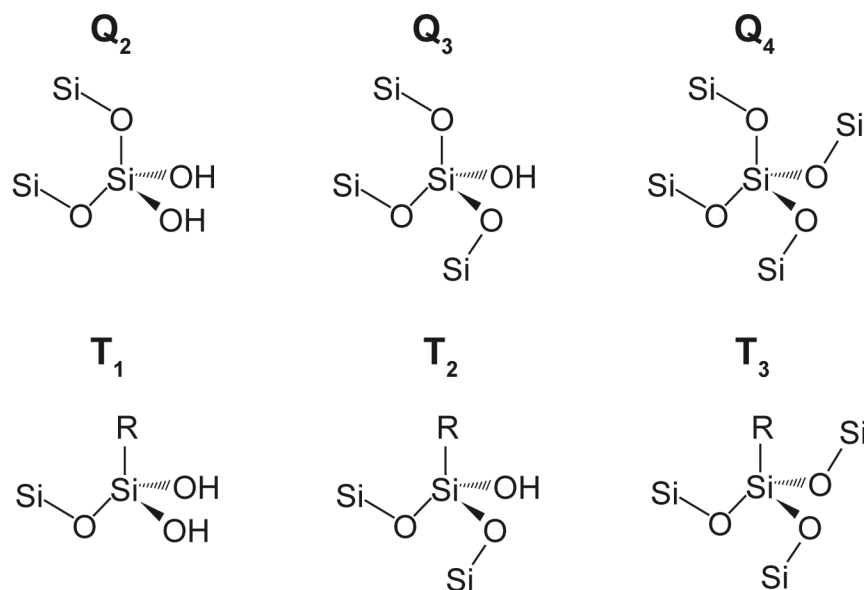


Figure 1.3. Silicon coordination environments. The number in the subscript corresponds to the number of directly bound bridging siloxane bonds.

A reactive surface combined with high surface area is a good indication of how well an SiO_2 substrate will catalyze the formation of peptide bonds which is an important aspect in origin of life research. Mineral oxides have long been used as catalysts for various purposes, and silica and clays have shown excellent potential in catalyzing the polymerization of amino acids, nucleotides, and other prebiotic molecules.^{24, 32, 33} Crystalline silica polymorphs are highly ordered and occur naturally most commonly as quartz, tridymite, and cristobalite.¹² Amorphous silica and silicates exist in many forms, including clays, basalts, sand, rocks, and chondrites.^{1, 34-39} The work presented here uses FSN to model natural, amorphous (glassy), defective forms of silica which are underrepresented in studies involving polymerization of prebiotic molecules.

Origins of life

The origin of life on Earth remains one of science's most elusive yet important unanswered questions. Over a century of research has identified several constraints that we can use to develop a timeline and explore plausible scenarios surrounding the emergence of life on Earth. The first constraint to consider is the Theia impact which created our moon and heated Earth's crust to a molten state (4.51 bya).⁴⁰ The upper limit for the emergence of life then rests on the solidification of Earth's crust and formation of liquid hydrosphere, which is placed at 4.4 ± 0.8 bya evidenced by the discovery and analysis of Jack Hills zircons.⁴¹ The lower limit, placed at 3.48 bya, is determined by the earliest fossil indicating life which has been identified as the presence of microbial organisms and biofilms that alter sedimentary structures (stromatolites).^{34, 42} Therefore, it is generally agreed upon that life emerged somewhere between 3.5 and 4.5 bya, but the specific point in time is still debated.

Similar constraints have been developed for environmental conditions such as temperature, atmosphere, radiation, minerality, pH, and salinity.^{37, 38, 40, 43-45} These constraints are necessary to shape the arena of origins research, but still cast a wide net for exploration once the full extent of diversity in climates and microenvironments across the planet is considered.^{46, 47} Each of the environmental conditions listed above have a large impact on the outcome of chemical reactions, specifically polymerization mechanisms. It is possible that multiple evolutionary pathways were occurring simultaneously and while we don't know which exact pathway gave rise to life, we emphasize the importance of identifying promising conditions and guiding principles to understand how life could have originated.

Minerology records provide additional insight to the emergence of life and explicitly demonstrate the co-evolution of life and the environment. Prebiotic Hadean Earth (>4 bya) was

covered in black basalt, a mineral-rich silicate formed from molten magma and lava.³⁶ The biodiversity and mineral diversity that exist on Earth today are the culmination of billions of years of evolution in an oxygen-rich environment. Over 4000 different mineral species have been catalogued on Earth, many of which were formed after our oxygen-rich atmosphere appeared.³⁶ Other rocky planets like Mercury, Mars, and our moon are estimated to contain no more than a few hundred different mineral species.³⁶ This suggests that mineral diversity can be a valuable signature for determining the potential of a planet to host (or have previously) hosted life. Silica has been identified as the primary component in rocky crusts, and it is important to explore many different surfaces, crystalline and amorphous, for understanding the importance of the role silica may have played in directing prebiotic chemistry and promoting chemical evolutionary pathways. This dissertation is motivated by the surprising lack of data that exists on amorphous, glassy silica types in prebiotic oligomerization which must be considered for a complete picture in chemical evolution.

Techniques

Thermogravimetric analysis

Thermogravimetric analysis (TGA) is a thermal analytical technique where sample mass is recorded as a function of temperature. Every organic material has a characteristic thermogram made up of discrete thermal events. The temperature at which these events occur is influenced by the controlled rate ($^{\circ}\text{C}/\text{min}$) of temperature change. This is the preferred method of quantifying how much material is adsorbed in organic – inorganic composites, sometimes referred to as loading capacity. Since silica has a high thermal stability and does not decompose at temperatures below $1600\text{ }^{\circ}\text{C}$, any weight loss can be attributed to the desorption of water, catalytic events and/or

decomposition of adsorbed ligands (**Figure 1.4, left**). Our experiments are typically performed under an inert atmosphere ($N_2(g)$) but air or $O_2(g)$ can also be used.

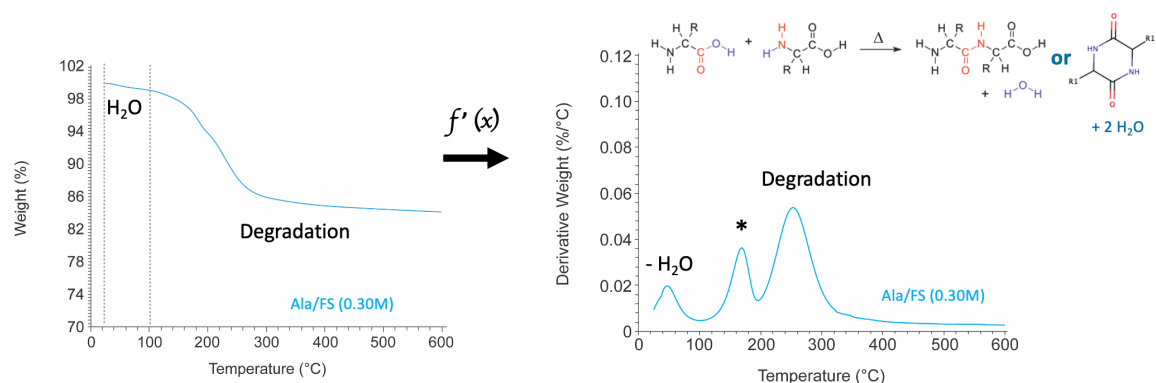


Figure 1.4. (left) Typical TGA curve for amino acids on silica nanoparticles and (right) the first derivative curve with expected peaks. The asterisk (*) indicates water loss from a thermal condensation reaction shown above which results in a single peptide bond, or more commonly with amino acids on silica, DKP.

It is useful to express TGA data as the first derivative (DTG) to visualize each thermal event which appear as peaks in the curve (**Figure 1.4, right**). A peak indicates a rapid change in weight loss and can be quantified by integration, rate of change, and peak maximum. The linewidth also gives a qualitative measure of disorder at the interface over which the reaction proceeds. In amino acid adsorptions on silica, a typical DTG curve has three peaks. The first peak (~ 50 °C) represents the desorption of physisorbed water, a second peak in the range of 150 to 200 °C indicates water loss from adsorbed amino acid thermal condensation reactions that result in peptide bond formation^{21-24, 48, 49}, and any peaks above 200 °C are attributed to decomposition of organic

matter. DTG presents a simple and effective way to identify the presence of oligomerization reactions and indicate the efficacy of each substrate in catalyzing these reactions.

Solution state nuclear magnetic resonance

Nuclear magnetic resonance (NMR) is a non-destructive spectroscopic technique that exploits the intrinsic nuclear spin property of NMR active nuclei and can be used to gain a wealth of atomic- and molecular-level information about a sample. The gyromagnetic ratio (γ) is often used to describe NMR active nuclei, which is simply the ratio of nuclear magnetic moment to spin angular momentum. When nuclei with a magnetic moment are placed in an external magnetic field (B_0) the nuclear spins will align with a Boltzmann distribution creating a net magnetization vector aligned along B_0 .^{50, 51} The spins precess at a frequency, referred to as the Larmor frequency (ω_L), that is proportional to the strength of the magnetic field. The equation is shown below:⁵⁰

$$\omega_L = -\gamma B_0$$

A pulse of radio frequency radiation is applied that perturbs the equilibrium state and tips the magnetization vector usually into the xy plane. The magnetization vector can then be manipulated in a variety of ways, described by the applied pulse sequence, to yield different information. Even simple 1-dimensional (1D) experiments typically consist of multiple pulses aimed at increasing signal to noise, removing intramolecular J-coupling interactions (i.e. proton decoupling), or suppressing signals from the solvent. After the pulse sequence is applied, time is allowed for data acquisition of the isolated spin system followed by a delay (recycle delay, or d1) to allow the nuclear spins to return to equilibrium with B_0 . The amount of time it takes the spins to return to the Boltzmann distribution is referred to as T_1 or “spin-lattice” relaxation.⁵²

T_1 relaxation is temperature dependent and can be quantified, usually with saturation recovery experiments (shown in **Figure 2.S4**) which gives some indication on the rotational dynamics of the molecular species.⁵² Most T_1 relaxation times in solutions range from 0.1 to 10 seconds. Local dynamics, chemical exchange, nuclear spin, and viscosity are just some of the factors that affect T_1 relaxation. In solids T_1 can range from milliseconds in hydrated and/or dynamic environments to a few hundred seconds in rigid, crystalline material. The length of the recycle delay is generally set to $5 \times T_1$ and largely impacts the total experiment time.

Magnetization can be transferred through-bond (scalar or J- coupling) or through-space (dipolar coupling) between nuclei to view correlations with nearby spins. In liquids, magnetization transfer typically occurs through-bond with an upper limit of 5-6 bonds. Pulse sequences often contain delays that depend on the scalar coupling values and can be edited to filter for specific interactions. Homonuclear magnetization transfer can be viewed as a 1D or 2D spectrum with correlations between coupled atoms of the same type (i.e. ^1H to ^1H). $^1\text{H} - ^1\text{H}$ correlation spectroscopy (COSY) is a 2D technique that yields cross-peaks between coupled proton groups that are separated by 2-3 bonds.⁵³ COSY experiments provide information about the connectivity within a molecule and is one of the most frequently used 2D NMR techniques.⁵⁴ Similarly, $^1\text{H} - ^1\text{H}$ total correlation spectroscopy (TOCSY) experiments display coupling within an entire spin system.^{55, 56} Cross-peaks will appear between scalar coupled proton groups up to 5-6 bonds away, as long as they do not cross a non-protonated group. This technique is commonly applied to peptides, proteins and oligosaccharides.⁵⁴ The nuclear overhauser enhancement spectroscopy (NOESY) experiment is a homonuclear technique that relies on dipole coupling to show through-space correlations.^{57, 58} The intensities of the cross-peaks are proportional to the distance between the groups (r^6), and the delay in the pulse sequence can be varied to view short- and long-range

correlations. For these reasons, NOESY experiments are often used to identify tertiary structures in proteins and stereochemistry in small molecules.

Magnetization transfer can also occur between different nuclei within a molecule. Heteronuclear single quantum coherence (HSQC) experiments produce a 2D spectrum, with ^1H in the direct (F_2) dimension, and X in the indirect (F_1) dimension (X is any less abundant nuclei, see **Table 1.1**).⁵⁹ A correlation will appear at the chemical shifts of each unique ^1H environment and the directly bound X group. Phase sensitive HSQC is commonly used to aid in structural assignment, where CH and CH_3 groups appear with positive phase, and CH_2 groups with negative phase.^{60, 61} Similarly, heteronuclear multiple bond correlation (HMBC) is a 2D heteronuclear technique used to view long range J-coupling, with correlations between ^1H and X 2-3 bonds away.⁶² The pulse sequence suppresses 1-bond correlations, so HSQC and HMBC are often used in combination for structural assignment.

Nitrogen's ability to participate in hydrogen bonding allows for rapid exchange of any directly bound protons. Direct $^1\text{H} - ^{15}\text{N}$ correlations are not visible in exchangeable solvents such as 90:10 $\text{H}_2\text{O}:\text{D}_2\text{O}$ or 100% D_2O if the sample does not exhibit secondary or tertiary structure. For this reason, $^1\text{H} - ^{15}\text{N}$ HMBC experiments are particularly useful in peptide and protein backbone assignments where amide protons undergo rapid chemical exchange. The resulting spectrum displays correlations at the ^{15}N chemical shift and neighboring ^1H groups a few bonds away. 2D heteronuclear techniques such as the ones listed above provide a great way to obtain X chemical shifts indirectly since magnetization transfer experiments are dictated by the properties of ^1H . ^1H exhibits high natural abundance leading to increased signal to noise, and short T_1 relaxation allowing for faster experiments.

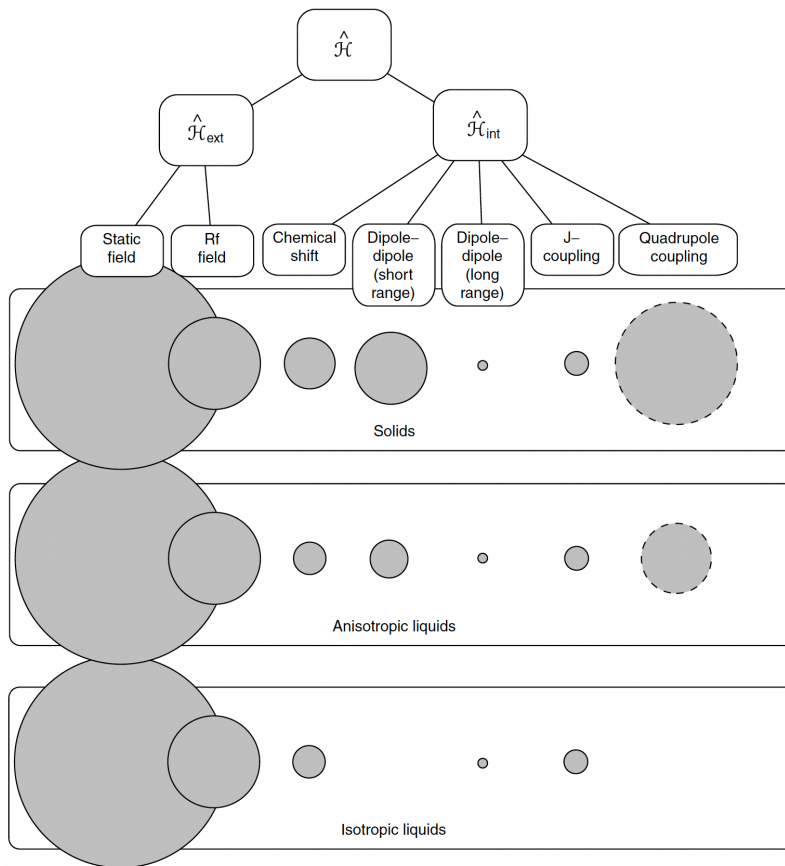


Figure 1.5. Electric and magnetic effects and their relative contributions that arise when NMR active nuclei interact with B_0 . Each interaction is described by a Hamiltonian operator (\mathcal{H}). Quadrupole coupling is eliminated if $I=1/2$.⁵⁰

Solid-state NMR

A number of electric and magnetic interactions occur when a sample with a nuclear spin (I) is placed in an external magnetic field (**Figure 1.5**). The largest electric contribution is quadrupole coupling, which is eliminated completely in nuclei with $I = 1/2$. Quadrupole effects are discussed in detail in the section below. Each electric and magnetic interaction is described by a spin Hamiltonian operating on vectors in space. Some of these magnetic interactions have an angular dependence, which is averaged in liquids by molecular tumbling.⁵⁰ The result is sharp,

well-resolved resonances at the isotropic chemical shift with a narrow linewidth usually spanning a few Hertz (Hz). In the solid-state, however, molecules are locked into a 3D spatial arrangement and line broadening occurs due to chemical shift anisotropy (CSA) and dipolar coupling for spin $\frac{1}{2}$ nuclei.⁶³ These interactions convolute solid-state NMR (SSNMR) spectra and produce broad powder patterns due to the summation of magnetic contributions from all orientations. CSA and dipolar coupling Hamiltonians have a $(3\cos^2\theta-1)/2$ dependence which can be set equal to zero by rotating the sample at the magic angle of 54.7° relative to B_0 .⁶⁴⁻⁶⁶ The rate of magic angle spinning (MAS) can be selected within the capabilities of the hardware, with faster MAS yielding better resolution (**Figure 1.6**). As a rule of thumb, the magic angle spinning rotor frequency (ν_R) needs to exceed the magnitude of the strongest anisotropic interactions in kHz to obtain well-resolved solid-state NMR spectra.

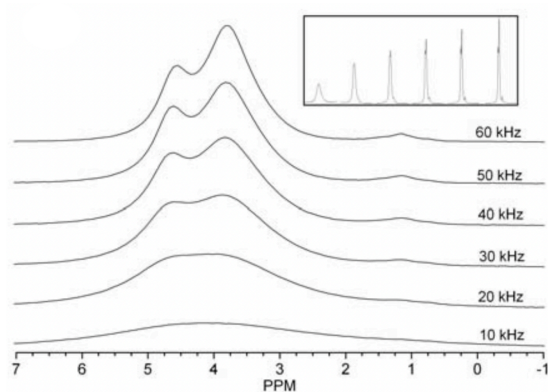


Figure 1.6. ^1H MAS SSNMR of MgAl-33 (a layered double hydroxide) at different spinning speeds to highlight the power of MAS. The inset shows the same spectra side by side to emphasize the gain in resolution.⁶⁷

The two most common SSNMR techniques will be discussed here and their pulse sequences are shown in **Figure 1.7**. Direct polarization magic angle spinning (DP-MAS) in simplest form is a single $\pi/2$ pulse experiment with proton heteronuclear decoupling applied during acquisition. If the recycle delay is sufficiently long for full T_1 relaxation, DP-MAS can be used for quantitative insight since signal intensity is dependent solely on the abundance of each unique chemical environment. In materials containing low natural abundance NMR active nuclei (e.g. ^{29}Si , ^{13}C and ^{15}N) isotopically enriched materials are commonly available for purchase to maximize signal intensity.

Alternatively, signals for less abundant nuclei (referred to as “X” nuclei in **Figure 1.7**) can be enhanced by through-space dipolar polarization transfer from abundant nuclei (usually ^1H) to dilute isotopes.⁶⁸ Polarization transfer occurs when the precessional frequencies of local magnetic fields are matched. This condition is called Hartman Hahn matching⁶⁹ and it is dependent on ν_R . X nuclei with a close proton spin bath are detected, and the theoretical signal enhancement is the ratio of the two gyromagnetic ratios. The duration of the cross polarization or “spin-lock” pulse can be varied to gain intra- and intermolecular distance information since polarization transfer occurs through space.⁶⁸ In the case of ^{29}Si CP-MAS NMR on silica or silicates where the only source of ^1H exists at the surface from hydroxyls or water, the technique is surface-selective, probing only silicon environments on the silica surface. The signal intensity depends on many factors such as distance from the proton spin bath, local dynamics, Hartman Hahn matching conditions, and CP efficiency to name a few.⁷⁰ CP-MAS NMR has made a significant contribution to the advancement of NMR techniques in solids and serves as the basis for most 2D and 3D SSNMR experiments.⁷¹⁻⁷³ Similar to heteronuclear correlation experiments in liquids, CP-MAS

SSNMR has the benefit of exploiting the properties of ^1H nuclei, leading to increased (although selective) signal intensity and faster experimental time.

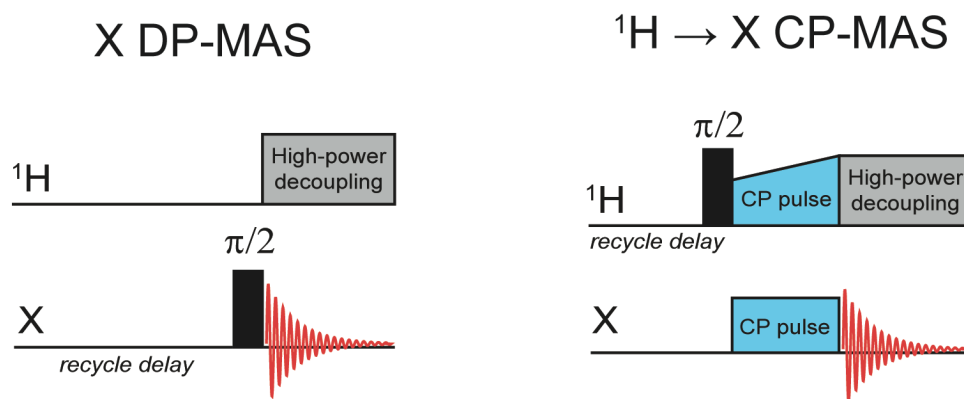


Figure 1.7. Basic SSNMR pulse sequences: (left) direct-polarization magic angle spinning (DP-MAS) and (right) cross-polarization magic angle spinning (CP-MAS).

Quadrupolar nuclei

Table 1.1 displays properties of the nuclei analyzed in this dissertation by NMR. The best NMR nuclei are ones that have a large gyromagnetic ratio, high natural abundance, and nuclear spin I equal to $\frac{1}{2}$. Materials comprised of spin $> \frac{1}{2}$ nuclei can still be analyzed by NMR but present additional challenges due to the presence of quadrupolar interactions that arise from the local electron cloud and a non-spherical nucleus (see **Figure 1.5** to view the relative contribution of quadrupolar effects, **Figure 1.8**). The ground state energy is split into $(2I+1)$ sublevels in the presence of an external magnetic field, so for spins = $\frac{1}{2}$ normal Zeeman splitting occurs (**Figure 1.8, left**). In the case of ^{27}Al ($I = \frac{5}{2}$), for example, the nuclear ground state splits into 6 sublevels

$(2 * 5/2 + 1)$ which allows for additional magnetic interactions (first and second order) that lead to line broadening and complex quadrupolar splitting patterns (**Figure 1.8, right**).

Table 1.1. NMR active nuclei and their properties that were analyzed in this dissertation.

Nuclei	γ (10^6 rad/sT)	Natural Abundance	Nuclear Spin
^1H	267	99.98%	$1/2$
^{13}C	67	1.1%	$1/2$
^{15}N	-27	0.37%	$1/2$
^{29}Si	-53	4.7%	$1/2$
^{27}Al	70	100%	$5/2$

Each quadrupolar isotope has a fixed quadrupole moment (units of length²) associated with it. The magnitude of the quadrupolar interaction then varies as a function of the electric field gradient (EFG), which is highly sensitive to the local symmetry around the nucleus⁷⁴ (**Figure 1.8**). Two other variables used to describe quadrupolar interactions are the nuclear quadrupolar coupling constant (C_Q) which describes the magnitude of the quadrupole-EFG interaction, and the dimensionless asymmetry parameter (η_Q) which describes the symmetry of the EFG tensor.⁷⁴ These values can be determined experimentally and are necessary to understand the magnitude of the first- and second-order quadrupolar effects, perform Hartman Hahn matching, and to quantify relative populations in quadrupolar SSNMR spectra.⁷⁴⁻⁷⁷ **Figure 1.9** shows ^{27}Al DP-MAS of γ -alumina which was used as a standard in the work outlined in Chapter 3. Two Al-coordination types are present. Peaks are asymmetric and significantly broadened due to C_Q .

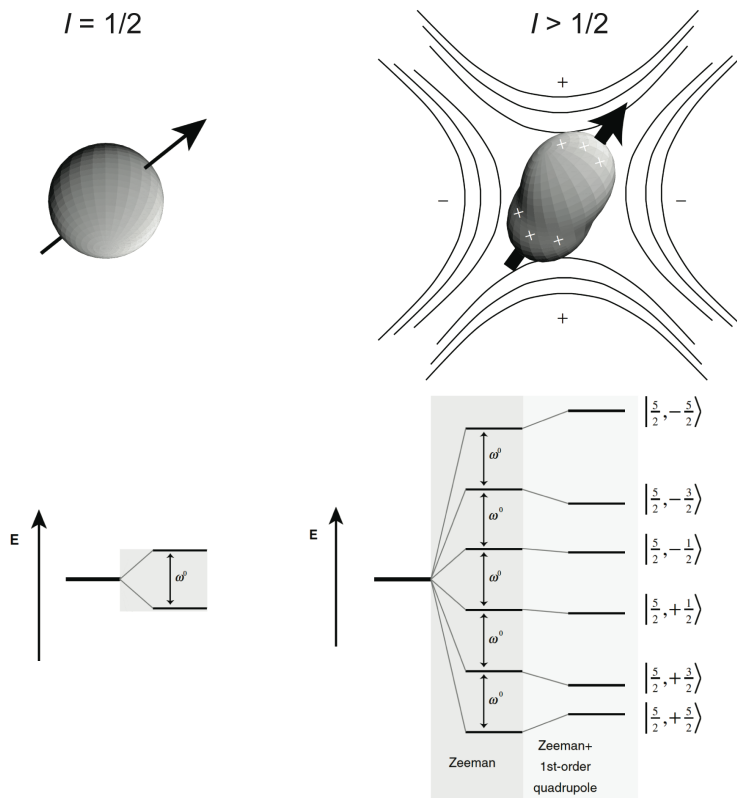


Figure 1.8. (left) Spin = $\frac{1}{2}$ nuclear shape and Zeeman energy splitting. (right) Quadrupolar, spin $> \frac{1}{2}$ nuclear shape and electric field gradient. The Zeeman energy splitting is representative of a nuclei $I = \frac{5}{2}$.⁵⁰

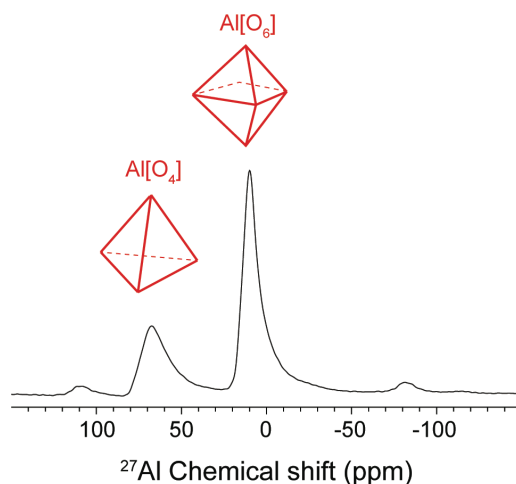


Figure 1.9. ^{27}Al DP-MAS of γ -alumina collected at 15 kHz MAS. Tetrahedral and octahedral coordination sites are present at 67 ppm and 10 ppm, respectively.

Diffusion NMR

In addition to structural analysis, another benefit of NMR is high accuracy quantification of local and global molecular dynamics. Molecules tumble freely in solution at a rate dependent on the size of the molecule and viscosity of the liquid.⁵⁰ The rate of diffusion can be quantified using a pulsed field gradient spin-echo (PGSE) experiment, which applies a 90° ^1H excitation pulse followed by a non-uniform gradient field to encode the spatial position of each spin.^{78, 79} A 180° refocusing pulse and opposing gradient field are applied to cancel or zero any spins with little to no free self-diffusion. ^1H signal intensity changes as the strength of the gradient field is varied over the course of the experiment (**Figure 1.10**). The duration of the applied gradient field (δ) and the diffusion period (Δ) remain constant, and together these values can be used to calculate the diffusion coefficient (D) using the Stejskal-Tanner equation:

$$S = S_0 * \exp [-(\gamma\delta g)^2 * D * \left(\Delta - \frac{\delta}{3}\right)]$$

where S is the measured signal intensity, S_0 is the signal intensity when the gradient strength is 0, γ is the gyromagnetic ratio of the nucleus, and g is the variable gradient field strength.^{78, 79} The gradient field strength is usually calibrated using the known self-diffusion coefficient of water in D_2O .⁸⁰ The diffusion coefficient can then be applied to the Stokes-Einstein equation (below) to approximate the size of the molecule:

$$D = \frac{k_B T}{6\pi\eta r}$$

where k_B is the Boltzmann constant, T is temperature, η is solvent viscosity, and r is the approximate hydrodynamic radius of the molecule, assuming a spherical particle.⁸¹ The Stejskal-Tanner equation provides an incredibly precise measurement of molecular self-diffusion. Diffusion ordered spectroscopy (DOSY) experiments create a pseudo-2D spectrum where different components within a mixture are separated by diffusion coefficients.^{82, 83} 1H signals are plotted against $\log(D)$ in the indirect dimension, so 1H groups within the same molecule can be easily identified.

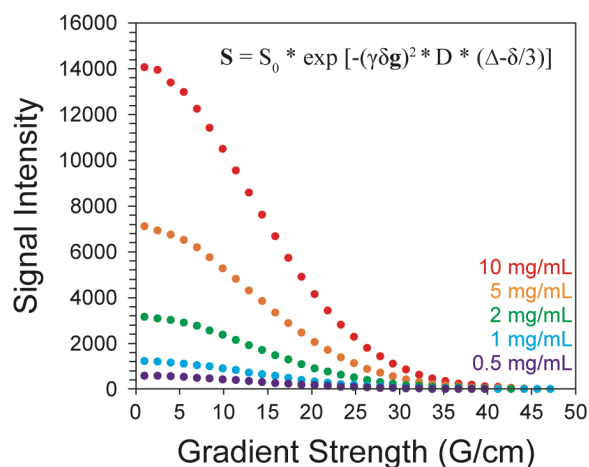


Figure 1.10. Diffusion NMR data and fit calculation for measuring the free diffusion of His in water at various concentrations.

Theoretical analysis

Computational chemistry occurs on a simulated molecular system designed within a software program. Small systems ranging from a few atoms up to ~ 100 atoms are calculated at the quantum mechanical level using software packages like Gaussian,⁸⁴ Gamess,⁸⁵ or Spartan.⁸⁶ A series of functions are applied to perturb the system until a minimum energy state is reached. This process is referred to as energy or geometry optimization.⁸⁷ After optimization, experimental parameters such as spectroscopy frequencies, orbital populations, and thermochemistry values, can be calculated or predicted based on the final 3D conformation. Computational chemistry provides compelling evidence for molecular structure and atomic interactions especially when paired with real experimental results.

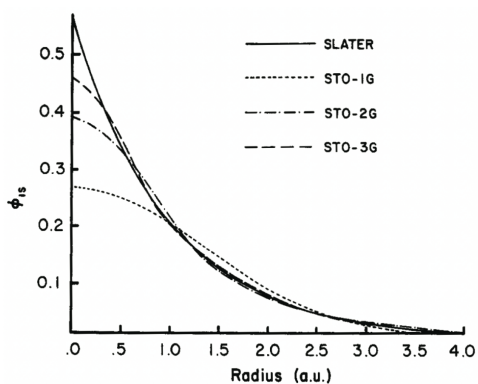
Larger systems such as proteins and lipid bilayers can be visualized and manipulated using molecular dynamics (MD) programs like GROMACS,⁸⁸ NAMD,⁸⁹ or AutoDock.⁹⁰ MD relies on classical mechanics to simplify the computational costs of such large systems. Similarly, energy

minimization is performed first. After the structure is optimized, a controlled perturbation is applied such as pressure, temperature, solvent, surface charge etc and changes in dynamics are simulated. While it is important to highlight the diverse applications of computational chemistry, molecular mechanics will not be discussed further in this dissertation.

An appropriate theoretical model should be selected based on the size of the system. Four main theoretical models exist, which define what approximations are used in the calculations: molecular mechanics⁹¹ (Harmonic oscillator, classical mechanics approximation), semi-empirical^{92, 93} (uses experimentally obtained data as fixed values), density functional^{94, 95} (local density approximation), and *ab initio*^{96, 97} (central field approximation). Generally, the higher the level of theory the greater the computational cost. The work presented in this dissertation was performed on systems comprising of 50 atoms or less using the density functional (DFT) level of theory and a hybrid B3LYP 6-31G+(d,p) basis set.⁹⁸ While the level of theory defines the set of underlying approximations used to describe the chemical system, the basis set defines how many functions are applied to describe the electronic wave function. Atomic orbitals are most accurately described using Slater-type orbitals (STOs) which are computationally intensive and can be well approximated by combining multiple Gaussian-type orbitals (GTOs)⁹⁹ (**Figure 1.11**). The nucleus region ($0.0 < r < 0.5$ in **Figure 1.11**) is not well approximated until a linear combination of 3 or more GTOs are used. The tail-end ($1.5 < r < 4.0$) is arguably the most important area to model accurately as it dictates molecular properties and is directly involved in intermolecular interactions.

In efforts to increase accuracy with reasonable computational times, John Pople first proposed split-valence basis sets¹⁰⁰ which are still widely used today. Pople-style basis sets apply different numbers of functions to model the core and valence orbitals, which helps account for polarizability and hybridization in the valence orbitals that participate in bonding. Polarization and

diffuse functions can be added as well to enhance the “flexibility” of atoms to form chemical bonds in any direction, and improve calculations in the outer limits of the atomic orbitals which become increasingly important in systems with long range electron densities like anions or hydrogen bonding. **Figure 1.11** (bottom) depicts the nomenclature and number of GTOs used in a split-valence triple-zeta Pople-style basis set.



6-311G+(d,p)

Atomic number	1-2		3-10	
	Basis functions	Constructed of	Basis functions	Constructed of
	1s	3 gaussians	1s	6 gaussians
	1s'	1 gaussian	2s, 2p _x , 2p _y , 2p _z	3 gaussians
	1s''	1 gaussian	2s', 2p _x ', 2p _y ', 2p _z '	1 gaussian
	2p _x , 2p _y , 2p _z	1 gaussian	2s'', 2p _x '', 2p _y '', 2p _z ''	1 gaussian
			3d _{xx} , 3d _{yy} , 3d _{zz}	1 gaussian
			3d _{xy} , 3d _{xz} , 3d _{yz}	1 gaussian
			3s, 3p _x , 3p _y , 3p _z	1 gaussian
Total number	6	8	23	36

Figure 1.11. (top) Depicts accuracy of approximating STOs with GTOs.¹⁰¹ (bottom) Example of a Pople-style triple zeta basis set nomenclature and how many functions are applied to each atom.⁸⁴

The basis set and level of theory should remain consistent in any calculations following optimization. In this dissertation, DFT with a 6-31G+(d,p) basis set was used with the gauge-including atomic orbital (GIAO) method¹⁰² to predict the NMR chemical shifts of the model system and compare to real, experimental results. Water was selected as the solvent system which is consistent with our solution NMR data, and a reference molecule was created in Gaussian and optimized at the same level of theory (tetramethylsilane for ¹H and ¹³C). The calculated NMR chemical shifts were extrapolated from the predicted shielding values using the equation below:

$$\delta_{calc} = \sigma_{ref} - \sigma_{calc} + \delta_{ref}$$

where δ_{calc} is the calculated chemical shift for the model, σ_{ref} is the calculated shielding value of the reference, σ_{calc} is the calculated shielding value of the model, and δ_{ref} is the experimental chemical shift of the reference (0 ppm for TMS).^{22, 103, 104} NMR chemical shifts calculated in this way are more accurate than using the standard reference molecules in Gaussian which are often calculated at a different level of theory.

References

1. Clarke, F. W.; Washington, H. S. *The composition of the Earth's crust*; 127; 1924.
2. Kuhlmann, A. M., The Second Most Abundant Element in the Earth's Crust. *JOM* **1963**, *15* (7), 502-505.
3. Croissant, J. G.; Butler, K. S.; Zink, J. I.; Brinker, C. J., Synthetic amorphous silica nanoparticles: toxicity, biomedical and environmental implications. *Nat Rev Mater* **2020**, *5* (12), 886-909.
4. Sun, B.; Pokhrel, S.; Dunphy, D. R.; Zhang, H.; Ji, Z.; Wang, X.; Wang, M.; Liao, Y. P.; Chang, C. H.; Dong, J.; Li, R.; Madler, L.; Brinker, C. J.; Nel, A. E.; Xia, T., Reduction of Acute Inflammatory Effects of Fumed Silica Nanoparticles in the Lung by Adjusting Silanol Display through Calcination and Metal Doping. *ACS Nano* **2015**, *9* (9), 9357-72.
5. Zhang, H.; Dunphy, D. R.; Jiang, X.; Meng, H.; Sun, B.; Tarn, D.; Xue, M.; Wang, X.; Lin, S.; Ji, Z.; Li, R.; Garcia, F. L.; Yang, J.; Kirk, M. L.; Xia, T.; Zink, J. I.; Nel,

A.; Brinker, C. J., Processing pathway dependence of amorphous silica nanoparticle toxicity: colloidal vs pyrolytic. *J Am Chem Soc* **2012**, *134* (38), 15790-804.

6. Sun, B.; Wang, X.; Liao, Y. P.; Ji, Z.; Chang, C. H.; Pokhrel, S.; Ku, J.; Liu, X.; Wang, M.; Dunphy, D. R.; Li, R.; Meng, H.; Madler, L.; Brinker, C. J.; Nel, A. E.; Xia, T., Repetitive Dosing of Fumed Silica Leads to Profibrogenic Effects through Unique Structure-Activity Relationships and Biopersistence in the Lung. *ACS Nano* **2016**, *10* (8), 8054-66.

7. Miller, S. L.; Urey, H. C., Organic compound synthesis on the primitive earth. *Science* **1959**, *130* (3370), 245-51.

8. Bernal, J. D., *The Physical Basis of Life*. Routledge and Paul: 1951.

9. Lahav, N.; White, D.; Chang, S., Peptide formation in the prebiotic era: thermal condensation of glycine in fluctuating clay environments. *Science* **1978**, *201* (4350), 67-9.

10. Bogush, G. H.; Tracy, M. A.; Zukoski IV, C. F., Preparation Of Monodisperse Silica Particles: Control of Size and Mass Fraction. *J Non Cryst Solids* **1988**, *104*, 95-106.

11. Sato-Berrú, R.; Saniger, J. M.; Flores-Flores, J.; Sanchez-Espíndola, M., Simple Method for the Controlled Growth of SiO₂ Spheres. *J Mater Sci Eng A* **2013**, *3* (4), 237-242.

12. Rahman, I. A.; Padavettan, V., Synthesis of Silica Nanoparticles by Sol-Gel: Size-Dependent Properties, Surface Modification, and Applications in Silica-Polymer Nanocomposites—A Review. *J Nanomater* **2012**, *2012*, 1-15.

13. Stöber, W.; Fink, A., Controlled growth of monodisperse silica spheres in the micron size range. *J Colloid Interface Sci* **1968**, *26*, 62-69.

14. Paris, J. L.; Vallet-Regi, M., Mesoporous Silica Nanoparticles for Co-Delivery of Drugs and Nucleic Acids in Oncology: A Review. *Pharmaceutics* **2020**, *12* (6).

15. Narayan, R.; Nayak, U. Y.; Raichur, A. M.; Garg, S., Mesoporous Silica Nanoparticles: A Comprehensive Review on Synthesis and Recent Advances. *Pharmaceutics* **2018**, *10* (3).

16. Tang, F.; Li, L.; Chen, D., Mesoporous silica nanoparticles: synthesis, biocompatibility and drug delivery. *Adv Mater* **2012**, *24* (12), 1504-34.

17. Argyo, C.; Weiss, V.; Bräuchle, C.; Bein, T., Multifunctional Mesoporous Silica Nanoparticles as a Universal Platform for Drug Delivery. *Chem Mater* **2013**, *26* (1), 435-451.

18. Bellardita, M.; Di Paola, A.; Yurdakal, S.; Palmisano, L., Preparation of Catalysts and Photocatalysts Used for Similar Processes. 2019; pp 25-56.

19. Ulrich, G. D., Theory of Particle Formation and Growth in Oxide Synthesis Flames. *Combust Sci Technol* **1971**, *4* (1), 47-57.

20. Brinker, C. J.; Kirkpatrick, R. J.; Tallant, D. R.; Bunker, B. C.; Montez, B., NMR Confirmation of Strained “Defects” in Amorphous Silica. *J Non Cryst Solids* **1988**, *99*, 418-428.
21. Bouchoucha, M.; Jaber, M.; Onfroy, T.; Lambert, J.-F.; Xue, B., Glutamic Acid Adsorption and Transformations on Silica. *J Phys Chem C* **2011**, *115* (44), 21813-21825.
22. Swanson, H. L.; Guo, C.; Cao, M.; Addison, J. B.; Holland, G. P., Probing the binding modes and dynamics of histidine on fumed silica surfaces by solid-state NMR. *Phys Chem Chem Phys* **2020**, *22* (36), 20349-20361.
23. Guo, C.; Jordan, J. S.; Yarger, J. L.; Holland, G. P., Highly Efficient Fumed Silica Nanoparticles for Peptide Bond Formation: Converting Alanine to Alanine Anhydride. *ACS Appl Mater Interfaces* **2017**, *9* (20), 17653-17661.
24. Lambert, J. F.; Jaber, M.; Georgelin, T.; Stievano, L., A comparative study of the catalysis of peptide bond formation by oxide surfaces. *Phys Chem Chem Phys* **2013**, *15* (32), 13371-80.
25. *Fumed Silica Market by Type (Hydrophilic and Hydrophobic), Application (Silicone Elastomers, Paints, Coatings & Inks, Adhesives & Sealants, UPR & Composites), End-Use Industry, and Region - Global Forecast to 2026*; CH 5373; June 2021, p 195.
26. Inc, G. M. I. Fumed Silica Market projected to exceed \$2.3 billion by 2027, Says Global Market Insights Inc. <https://www.globenewswire.com/news-release/2021/03/09/2189246/0/en/Fumed-Silica-Market-projected-to-exceed-2-3-billion-by-2027-Says-Global-Market-Insights-Inc.html> (accessed 11/1/2021).
27. Matsumoto, A.; Tsutsumi, K.; Schumacher, K.; Unger, K. K., Surface Functionalization and Stabilization of Mesoporous Silica Spheres by Silanization and Their Adsorption Characteristics. *Langmuir* **2002**, *18*, 4014-4019.
28. Rimola, A.; Costa, D.; Sodupe, M.; Lambert, J. F.; Ugliengo, P., Silica surface features and their role in the adsorption of biomolecules: computational modeling and experiments. *Chem Rev* **2013**, *113* (6), 4216-313.
29. Liu, C. H. C.; Maciel, G. E., The fumed silica surface: A study by NMR. *J Am Chem Soc* **1996**, *118* (21), 5103-5119.
30. Hoffmann, F.; Cornelius, M.; Morell, J.; Froba, M., Silica-based mesoporous organic-inorganic hybrid materials. *Angew Chem Int Ed Engl* **2006**, *45* (20), 3216-51.
31. Burkett, S. L.; Sims, S. D.; Mann, S., Synthesis of hybrid inorganic-organic mesoporous silica by co-condensation of siloxane and organosiloxane precursors. *ChemComm* **1996**, (11), 1367-1368.
32. Huang, W.; Ferris, J. P., Synthesis of 35-40 mers of RNA oligomers from unblocked monomers. A simple approach to the RNA world. *ChemComm* **2003**, (12), 1458-9.

33. Lambert, J. F., Adsorption and polymerization of amino acids on mineral surfaces: a review. *Orig Life Evol Biosph* **2008**, *38* (3), 211-42.
34. Mojzsis, S. J.; Arrhenius, G.; McKeegan, K. D.; Harrison, T. M.; Nutman, A. P.; Friend, C. R. L., Evidence for life on Earth before 3,800 million years ago. *Nature* **1996**, *7*, 55.
35. Pizzarello, S., The Chemistry of Life's Origin: a Carbonaceous Meteorite Perspective. *Acc Chem Res* **2006**, *39* (4), 231-7.
36. Hazen, R. M., Evolution of minerals. *Sci Am* **2010**, *302* (3), 58-65.
37. Kasting, J. F., The Goldilocks Planet? How Silicate Weathering Maintains Earth "Just Right". *Elements* **2019**, *15* (4), 235-240.
38. Jones, C.; Nomosatryo, S.; Crowe, S. A.; Bjerrum, C. J.; Canfield, D. E., Iron oxides, divalent cations, silica, and the early earth phosphorus crisis. *Geology* **2015**, *43* (2), 135-138.
39. Boehnke, P.; Bell, E. A.; Stephan, T.; Trappitsch, R.; Keller, C. B.; Pardo, O. S.; Davis, A. M.; Harrison, T. M.; Pellin, M. J., Potassic, high-silica Hadean crust. *Proc Natl Acad Sci USA* **2018**, *115* (25), 6353-6356.
40. Benner, S. A.; Bell, E. A.; Biondi, E.; Brassler, R.; Carell, T.; Kim, H. J.; Mojzsis, S. J.; Omran, A.; Pasek, M. A.; Trail, D., When Did Life Likely Emerge on Earth in an RNA-First Process? *ChemSystemsChem* **2020**, *2* (2), e1900035.
41. Wilde, S. A.; Valley, J. W.; Peck, W. H.; Graham, C. M., Evidence from detrital zircons for the existence of continental crust and oceans on the Earth 4.4 Gyr ago. *Nature* **2001**, *409* (6817), 175-8.
42. Noffke, N.; Christian, D.; Wacey, D.; Hazen, R. M., Microbially induced sedimentary structures recording an ancient ecosystem in the ca. 3.48 billion-year-old Dresser Formation, Pilbara, Western Australia. *Astrobiology* **2013**, *13* (12), 1103-24.
43. Farquhar, J.; Bao, H.; Thiemens, M., Atmospheric influence of Earth's earliest sulfur cycle. *Science* **2000**, *289* (5480), 756-9.
44. Halevy, I.; Bachan, A., The geologic history of seawater pH. *Science* **2017**, *355* (6329), 1069-1071.
45. Akoopie, A.; Muller, U. F., Lower temperature optimum of a smaller, fragmented triphosphorylation ribozyme. *Phys Chem Chem Phys* **2016**, *18* (30), 20118-25.
46. Ruiz-Mirazo, K.; Briones, C.; de la Escosura, A., Prebiotic Systems Chemistry: New Perspectives for the Origins of Life. *Chem Rev* **2014**, *114*, 285-366.

47. Hazen, R. M., Presidential Address to the Mineralogical Society of America, Salt Lake City, October 18, 2005: Mineral surfaces and the prebiotic selection and organization of biomolecules. *American Mineralogist* **2006**, *91* (11-12), 1715-1729.
48. Meng, M.; Stievano, L.; Lambert, J.-F., Adsorption and Thermal Condensation Mechanisms of Amino Acids on Oxide Supports. 1. Glycine on Silica. *Langmuir* **2004**, *20* (22), 914-923.
49. Fuchida, S.; Masuda, H.; Shinoda, K., Peptide formation mechanism on montmorillonite under thermal conditions. *Orig Life Evol Biosph* **2014**, *44* (1), 13-28.
50. Levitt, M. H., *Spin Dynamics: Basics of Nuclear Magnetic Resonance*. Wiley: 2008; p 744.
51. Edwards, C. J., Principles of NMR. Process NMR Associates LLC: pp 1-51.
52. Bloembergen, N.; Purcell, E. M.; Pound, R. V., Relaxation Effects in Nuclear Magnetic Resonance Absorption. *Phys Rev* **1948**, *73* (7), 679-712.
53. Aue, W. P.; Bartholdi, E.; Ernst, R. R., Two-dimensional spectroscopy. Application to nuclear magnetic resonance. *J Chem Phys* **1976**, *64* (5), 2229-2246.
54. Berger, S.; Braun, S., *200 and More NMR Experiments: A Practical Course*. 3rd ed.; Wiley-VCH: 2004; p 632-632.
55. Braunschweiler, L.; Ernst, R. R., Coherence transfer by isotropic mixing: Application to proton correlation spectroscopy. *J Chem Phys* **1983**, *53* (3), 521-528.
56. Bax, A.; Davis, D. G., MLEV-17-Based Two-Dimensional Homonuclear Magnetization Transfer Spectroscopy. *J Magn Reson* **1985**, *65*, 355-360.
57. States, D. J.; Haberkorn, R. A.; Ruben, D. J., A Two-Dimensional Nuclear Overhauser Experiment with Pure Absorption Phase in Four Quadrants. *J Magn Reson* **1982**, *48*, 286-292.
58. Jeener, J.; Meier, B. H.; Bachmann, P.; Ernst, R. R., Investigation of exchange processes by two-dimensional NMR spectroscopy. *J Chem Phys* **1979**, *71* (11), 4546-4553.
59. Bodenhausen, G.; Ruben, D. J., Natural abundance nitrogen-15 NMR by enhanced heteronuclear spectroscopy. *Chem Phys Lett* **1980**, *69* (1), 185-189.
60. Palmer, A. G.; Cavanagh, J.; Wright, P. E.; Rance, M., Sensitivity improvement in proton-detected two-dimensional heteronuclear correlation NMR spectroscopy. *J Magn Reson* **1991**, *93* (1), 151-170.
61. Kay, L.; Keifer, P.; Saarinen, T., Pure absorption gradient enhanced heteronuclear single quantum correlation spectroscopy with improved sensitivity. *J Am Chem Soc* **1992**, *114* (26), 10663-10665.

62. Bax, A.; Summers, M. F., Proton and carbon-13 assignments from sensitivity-enhanced detection of heteronuclear multiple-bond connectivity by 2D multiple quantum NMR. *J Am Chem Soc* **1986**, *108* (8), 2093-2094.
63. Schaefer, J.; Stejskal, E. O.; Buchdahl, R., High-Resolution Carbon-13 Nuclear Magnetic Resonance Study of Some Solid, Glassy Polymers. *Macromolecules* **1975**, *8* (3), 291-296.
64. Andrew, E. R.; Bradbury, A.; Eades, R. G., Nuclear magnetic spectra from a crystal rotated at high speed. *Nature* **1958**, *182*, 1659-1659.
65. Andrew, E. R.; Bradbury, A.; Eades, R. G., Removal of Dipolar Broadening of Nuclear Magnetic Resonance Spectra of Solids by Specimen Rotation. *Nature* **1959**, *183* (4678), 1802-1803.
66. Lowe, I. J., Free Induction Decays of Rotating Solids. *Phys Rev Lett* **1959**, *2* (7), 285-287.
67. Sideris, P. J.; Nielsen, U. G.; Gan, Z.; Grey, C. P., Mg/Al ordering in layered double hydroxides revealed by multinuclear NMR spectroscopy. *Science* **2008**, *321* (5885), 113-7.
68. Pines, A.; Gibby, M. G.; Waugh, J. S., Proton-Enhanced Nuclear Induction Spectroscopy. A Method for High Resolution NMR of Dilute Spins in Solids. *J Chem Phys* **1972**, *56* (4), 1776-1777.
69. Hartmann, S. R.; Hahn, E. L., Nuclear Double Resonance in the Rotating Frame. *Phys Rev* **1962**, *128* (5), 2042-2053.
70. Chuang, I.-S.; Maciel, G. E., Probing Hydrogen Bonding and the Local Environment of Silanols on Silica Surfaces via Nuclear Spin Cross Polarization Dynamics. *J Am Chem Soc* **1996**, *118*, 401-406.
71. Caravatti, P.; Bodenhausen, G.; Ernst, R. R., Heteronuclear solid-state correlation spectroscopy. *Chem Phys Lett* **1982**, *89* (5), 363-367.
72. Takegoshi, K.; Nakamura, S.; Terao, T., ¹³C-¹H dipolar-assisted rotational resonance in magic-angle spinning NMR. *Chem Phys Lett* **2001**, *344* (5), 631-637.
73. Gullion, T.; Schaefer, J., Rotational-echo double-resonance NMR. *J Magn Reson* **1989**, *81* (1), 196-200.
74. Autschbach, J.; Zheng, S.; Schurko, R. W., Analysis of electric field gradient tensors at quadrupolar nuclei in common structural motifs. *Concepts Magn Reson A* **2010**, *36A* (2), 84-126.
75. Ashbrook, S. E.; Duer, M. J., Structural information from quadrupolar nuclei in solid state NMR. *Concepts Magn Reson A* **2006**, *28A* (3), 183-248.

76. Kentgens, A. P. M., A practical guide to solid-state NMR of half-integer quadrupolar nuclei with some applications to disordered systems. *Geoderma* **1997**, *80* (3-4), 271-306.
77. Massiot, D.; Bessada, C.; Coutures, J. P.; Taulelle, F., Quantitative study of ^{27}Al MAS NMR in crystalline YAG. *J Chem Phys* **1990**, *90*, 231-242.
78. Stejskal, E. O.; Tanner, J. E., Spin Diffusion Measurements: Spin Echoes in the Presence of a Time-Dependent Field Gradient. *J Chem Phys* **1965**, *42* (1), 288-292.
79. Sinnaeve, D., The Stejskal-Tanner equation generalized for any gradient shape-an overview of most pulse sequences measuring free diffusion. *Concepts Magn Reson A* **2012**, *40A* (2), 39-65.
80. Mills, R., Self-Diffusion in Normal and Heavy Water in the Range 1-45. *J Phys Chem* **1973**, *77* (5), 685-688.
81. Miller, C. C.; Walker, J., The Stokes-Einstein law for diffusion in solution. *Proceedings of the Royal Society of London. Series A, Containing Papers of a Mathematical and Physical Character* **1924**, *106* (740), 724-749.
82. Johnson, C. S., Diffusion ordered nuclear magnetic resonance spectroscopy: principles and applications. *Prog Nucl Magn Reson Spectrosc* **1999**, *34* (3-4), 203-256.
83. Morris, K. F.; Johnson, C. S., Diffusion-ordered two-dimensional nuclear magnetic resonance spectroscopy. *J Am Chem Soc* **1992**, *114* (8), 3139-3141.
84. Frisch, M. J.; Trucks, G. W.; Schlegel, H. B.; Scuseria, G. E.; Robb, M. A.; Cheeseman, J. R.; Scalmani, G.; Barone, V.; Petersson, G. A.; Nakatsuji, H.; Li, X.; Caricato, M.; Marenich, A. V.; Bloino, J.; Janesko, B. G.; Gomperts, R.; Mennucci, B.; Hratchian, H. P.; Ortiz, J. V.; Izmaylov, A. F.; Sonnenberg, J. L.; Williams, D.; Ding, F.; Lipparini, F.; Egidi, F.; Goings, J.; Peng, B.; Petrone, A.; Henderson, T.; Ranasinghe, D.; Zakrzewski, V. G.; Gao, J.; Rega, N.; Zheng, G.; Liang, W.; Hada, M.; Ehara, M.; Toyota, K.; Fukuda, R.; Hasegawa, J.; Ishida, M.; Nakajima, T.; Honda, Y.; Kitao, O.; Nakai, H.; Vreven, T.; Throssell, K.; Montgomery Jr., J. A.; Peralta, J. E.; Ogliaro, F.; Bearpark, M. J.; Heyd, J. J.; Brothers, E. N.; Kudin, K. N.; Staroverov, V. N.; Keith, T. A.; Kobayashi, R.; Normand, J.; Raghavachari, K.; Rendell, A. P.; Burant, J. C.; Iyengar, S. S.; Tomasi, J.; Cossi, M.; Millam, J. M.; Klene, M.; Adamo, C.; Cammi, R.; Ochterski, J. W.; Martin, R. L.; Morokuma, K.; Farkas, O.; Foresman, J. B.; Fox, D. J. *Gaussian 16 Rev. C.01*, Wallingford, CT, 2016.
85. Barca, G. M. J.; Bertoni, C.; Carrington, L.; Datta, D.; De Silva, N.; Deustua, J. E.; Fedorov, D. G.; Gour, J. R.; Gunina, A. O.; Guidez, E.; Harville, T.; Irle, S.; Ivanic, J.; Kowalski, K.; Leang, S. S.; Li, H.; Li, W.; Lutz, J. J.; Magoulas, I.; Mato, J.; Mironov, V.; Nakata, H.; Pham, B. Q.; Piecuch, P.; Poole, D.; Pruitt, S. R.; Rendell, A. P.; Roskop, L. B.; Ruedenberg, K.; Sattasathuchana, T.; Schmidt, M. W.; Shen, J.; Slipchenko, L.; Sosonkina, M.; Sundriyal, V.; Tiwari, A.; Galvez Vallejo, J. L.; Westheimer, B.; Wloch, M.; Xu, P.; Zahariev, F.; Gordon, M. S., Recent developments in the general atomic and molecular electronic structure system. *J Chem Phys* **2020**, *152* (15), 154102.

86. Shao, Y.; Molnar, L. F.; Jung, Y.; Kussmann, J.; Ochsenfeld, C.; Brown, S. T.; Gilbert, A. T.; Slipchenko, L. V.; Levchenko, S. V.; O'Neill, D. P.; DiStasio, R. A., Jr.; Lochan, R. C.; Wang, T.; Beran, G. J.; Besley, N. A.; Herbert, J. M.; Lin, C. Y.; Van Voorhis, T.; Chien, S. H.; Sodt, A.; Steele, R. P.; Rassolov, V. A.; Maslen, P. E.; Korambath, P. P.; Adamson, R. D.; Austin, B.; Baker, J.; Byrd, E. F.; Dachsel, H.; Doerksen, R. J.; Dreuw, A.; Dunietz, B. D.; Dutoi, A. D.; Furlani, T. R.; Gwaltney, S. R.; Heyden, A.; Hirata, S.; Hsu, C. P.; Kedziora, G.; Khalliulin, R. Z.; Klunzinger, P.; Lee, A. M.; Lee, M. S.; Liang, W.; Lotan, I.; Nair, N.; Peters, B.; Proynov, E. I.; Pieniazek, P. A.; Rhee, Y. M.; Ritchie, J.; Rosta, E.; Sherrill, C. D.; Simmonett, A. C.; Subotnik, J. E.; Woodcock, H. L., 3rd; Zhang, W.; Bell, A. T.; Chakraborty, A. K.; Chipman, D. M.; Keil, F. J.; Warshel, A.; Hehre, W. J.; Schaefer, H. F., 3rd; Kong, J.; Krylov, A. I.; Gill, P. M.; Head-Gordon, M., Advances in methods and algorithms in a modern quantum chemistry program package. *Phys Chem Chem Phys* **2006**, *8* (27), 3172-91.
87. Cooksy, A., *Physical Chemistry: Quantum Chemistry and Molecular Interactions*. Pearson: 2014.
88. BEKKER, H.; BERENDSEN, H.; DIJKSTRA, E.; ACHTEROP, S.; VONDRUMEN, R.; VANDERSPOEL, D.; SIJBERS, A.; Keegstra, H.; RENARDUS, M. In *GROMACS - A PARALLEL COMPUTER FOR MOLECULAR-DYNAMICS SIMULATIONS*, 4th International Conference on Computational Physics (PC 92), Czech Republic, RA DeGroot, J. N., Ed. World Scientific Publishing: Czech Republic, 1992; pp 252-256.
89. Phillips, J. C.; Hardy, D. J.; Maia, J. D. C.; Stone, J. E.; Ribeiro, J. V.; Bernardi, R. C.; Buch, R.; Fiorin, G.; Henin, J.; Jiang, W.; McGreevy, R.; Melo, M. C. R.; Radak, B. K.; Skeel, R. D.; Singharoy, A.; Wang, Y.; Roux, B.; Aksimentiev, A.; Luthey-Schulten, Z.; Kale, L. V.; Schulten, K.; Chipot, C.; Tajkhorshid, E., Scalable molecular dynamics on CPU and GPU architectures with NAMD. *J Chem Phys* **2020**, *153* (4), 044130.
90. Goodsell, D. S.; Olson, A. J., Automated docking of substrates to proteins by simulated annealing. *Proteins* **1990**, *8* (3), 195-202.
91. Boyd, D. B.; Lipkowitz, K. B., Molecular Mechanics The Method and Its Underlying Philosophy. *J Chem Educ* **1982**, *59* (4), 269-274.
92. Hückel, E., Quantentheoretische Beiträge zum Benzolproblem. *Zeitschrift für Physik* **1931**, *70* (3), 204-286.
93. Thiel, W., Semiempirical quantum-chemical methods. *WIREs Computational Molecular Science* **2013**, *4* (2), 145-157.
94. Hohenberg, P.; Kohn, W., Inhomogeneous Electron Gas. *Phys Rev* **1964**, *136* (3B), B864-B871.
95. Mardirossian, N.; Head-Gordon, M., Thirty years of density functional theory in computational chemistry: an overview and extensive assessment of 200 density functionals. *Molecular Physics* **2017**, *115* (19), 2315-2372.

96. Hehre, W. J., Ab Initio Molecular Orbital Theory. *Acc Chem Res* **1976**, *9*, 399-406.
97. Friesner, R. A., Ab initio quantum chemistry: methodology and applications. *Proc Natl Acad Sci USA* **2005**, *102* (19), 6648-53.
98. Stephens, P. J.; Devlin, F. J.; Chabalowski, C. F.; Frisch, M. J., Ab Initio Calculation of Vibrational Absorption and Circular Dichroism Spectra Using Density Functional Force Fields. *J Phys Chem* **1994**, *98* (45), 11623-11627.
99. Chong, D. P.; Gruning, M.; Baerends, E. J., STO and GTO field-induced polarization functions for H to Kr. *J Comput Chem* **2003**, *24* (13), 1582-91.
100. Hehre, W. J.; Stewart, R. F.; Pople, J. A., Self-Consistent Molecular-Orbital Methods. I. Use of Gaussian Expansions of Slater-Type Atomic Orbitals. *J Chem Phys* **1969**, *51* (6), 2657-2664.
101. Szabo, A.; Ostlund, N. S., *Modern Quantum Chemistry: Introduction to Advanced Electronic Structure Theory*. Dover Publications: 2012.
102. Wolinski, K.; Hinton, J. F.; Pulay, P., Efficient implementation of the gauge-independent atomic orbital method for NMR chemical shift calculations. *J Am Chem Soc* **2002**, *112* (23), 8251-8260.
103. Gervais, C.; Dupree, R.; Pike, K. J.; Bonhomme, C.; Profeta, M.; Pickard, C. J.; Mauri, F., Combined first-principles computational and experimental multinuclear solid-state NMR investigation of amino acids. *J Phys Chem A* **2005**, *109* (31), 6960-9.
104. Gervais, C.; Profeta, M.; Lafond, V.; Bonhomme, C.; Azais, T.; Mutin, H.; Pickard, C. J.; Mauri, F.; Babonneau, F., Combined ab initio computational and experimental multinuclear solid-state magnetic resonance study of phenylphosphonic acid. *Magn Reson Chem* **2004**, *42* (5), 445-52.

Chapter 2

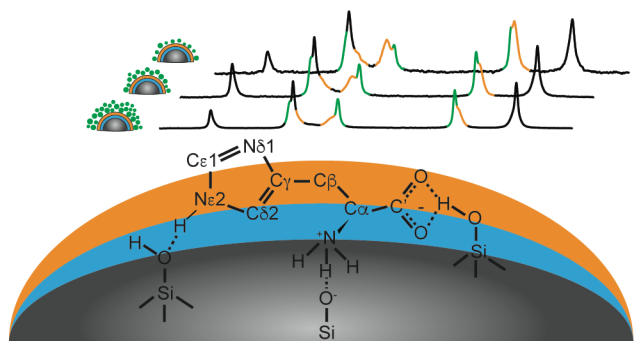
Probing the binding modes and dynamics of histidine on fumed silica surfaces by solid-state NMR

Abstract

Silica nanoparticles can be designed to exhibit a diverse range of morphologies (e.g. non-porous, mesoporous), physical properties (e.g. hydrophobic, hydrophilic) and a wide range of chemical and biomolecular surface functionalizations. In the present work, the adsorption complex of histidine (His) and fumed silica nanoparticles (FSN) is probed using thermal analysis (TGA/DTG) and a battery of solid-state (SS) NMR methods supported by DFT chemical shift calculations. Multinuclear ($^1\text{H}/^{13}\text{C}/^{15}\text{N}$) one- and two dimensional magic angle spinning (MAS) SSNMR experiments were applied to determine site-specific interactions between His and FSN surfaces as a function of adsorption solution concentration, pH and hydration state. By directly comparing SSNMR observables (linewidth, chemical shift and relaxation parameters) for His–FSN adsorption complexes to various crystalline, amorphous and aqueous His forms, the His structural and dynamic environment on FSN surfaces could be determined at an atomic level. The observed ^{13}C and ^{15}N MAS NMR chemical shifts, linewidths and relaxation parameters show that the His surface layer on FSN has a significant dependence on pH and hydration state. His is highly dynamic on FSN surfaces under acidic conditions (pH 4) as evidenced by sharp resonances with near isotropic chemical shifts regardless of hydration level indicating a non-specific binding arrangement while, a considerably more rigid His environment with defined protonation states is observed at near neutral pH with subtle variations between hydrated and anhydrous complexes. At near neutral pH, less charge repulsion occurs on the FSN surface and His is more tightly bound as evidenced by considerable line broadening likely due to chemical shift heterogeneity and a distribution in hydrogen-bonding strengths on the FSN surface. Multiple His sites exchange with a tightly bound water layer in hydrated samples while, direct interaction with the FSN surface and significant chemical shift perturbations for imidazole ring nitrogen sites and some carbon

resonances are observed after drying. The SSNMR data was used to propose an interfacial molecular binding model between His and FSN surfaces under varying conditions setting the stage for future multinuclear, multidimensional SSNMR studies of His-containing peptides on silica nanoparticles and other nanomaterials of interest.

Graphical Abstract



Introduction

Silica nanoparticles can be designed to exhibit a diverse range of morphologies (e.g. non-porous, mesoporous), physical properties (e.g. hydrophobic, hydrophilic) and a wide range of therapeutics,^{6,10-14} and noninvasive sensors and detectors.^{10,15} However, the site-specific, molecular-level interactions that occur This method produces spherical, monodisperse particles at a desired size in the nanometer to micron length scale (Stöber, colloidal silica).²⁴⁻²⁶ Pyrolysis produces silica nanoparticles from silicon tetrachloride heated in a flame followed by rapid quenching (fumed silica nanoparticles, FSN). The process of rapid quenching creates an agglomerated, branched nanomaterial with a high population of strained siloxane rings which makes these nanoparticles more reactive.²⁷ Mesoporous silica nanoparticles (MSN) are another widely used type of silica nanoparticle with uniform and tunable hollow pore networks formed by

using a surfactant-based templating agent, commonly cetyltrimethylammonium bromide (CTAB).^{3,8,28–30} MSN can provide a platform for catalytic reactions, encapsulation, and controlled drug release.^{3,14,28,31–35} MSN have excellent biocompatibility, high drug loading capacity, and flexible mechanisms for drug deployment including pH, light, redox, temperature, or enzyme-triggered reactions.^{4,14,32,35} In one example, Bilalis et al. grafted poly(L-histidine) to the MSN surface to provide a pH-controlled gatekeeper for the release of the anticancer drug doxorubicin.⁹ Despite these advances, it remains a challenge to characterize histidine (His) binding to the silica surface at an atomic, site-specific level. His has multiple available hydrogen bonding sites on the imidazole sidechain ring and backbone (**Figure 2.1, Top**), making it one of the more complicated amino acids to investigate on nanoparticle surfaces. The pK_a of the side chain is near physiological pH which makes it relatively easy to move protons on and off. This flexible charge transfer is one reason why His is a common residue in protein binding sites.³⁶ Understanding how His binds and organizes on silica surfaces will aid the prediction of possible binding modes for His-containing peptides on silica surfaces and should impact the development of drug delivery system.

FSN displays an intrinsically disordered surface where strained rings easily cleave to form radicals at the nanoparticle interface upon rehydration.^{27,37} The presence of these radicals may play a key role in amino acid adsorption and thermal condensation on FSN when mild heat treatment is applied.³⁸ The latter is particularly important to the Origin of Life field and FSN appears to be a suitable model for carbonaceous chondrites, volcanic silica, or other prebiotic silica surfaces formed under extreme conditions and temperatures similar to FSN. FSN is a highly efficient peptide bond catalyst compared to other silica forms³⁸ and related prebiotic silicates could have been involved in accumulating and catalyzing amino acids into the first peptides on prebiotic Earth. Thus, understanding how different amino acids bind is important in this context as well.

SSNMR offers unique advantages to elucidate site-specific, atomic-level intermolecular interactions at the bio-nano interface and are not readily probed with other techniques. In the present work, one (1D) and two-dimensional (2D) SSNMR methods were utilized to identify interactions at the His–FSN interface. The protonation state and structure of various His forms in the solid-state (L-His, HCl salt, amorphous form) and in aqueous solution as a function of pH were determined with NMR. Chemical shift (^1H , ^{13}C , ^{15}N) information from these experiments were then used to aid the understanding of the His–FSN adsorption complexes produced at various pH, loading levels, and hydration state. The NMR results together with chemical shift calculations were used to propose a site-specific molecular binding model for His–FSN at pH 4 and 7.6 in hydrated and dehydrated forms.

Experimental

Materials

FSN (~7 nm) with Brunauer, Emmett, and Teller (BET) surface area of $395 \pm 25 \text{ m}^2 \text{ g}^{-1}$, natural abundance L-histidine monohydrochloride monohydrate ($\geq 99.5\%$), and natural abundance pure L-histidine ($\geq 99.5\%$) were purchased from Sigma-Aldrich. Fully labeled U- ^{15}N , ^{13}C -L-histidine monohydrochloride monohydrate (98%) was purchased from Cambridge Isotopes Inc. All materials were used as received. In the present work, silica or SiO_2 refers to FSN.

Sample preparation

His was analyzed as a crystalline solid (HCl salt), noncrystalline powder (zwitterionic form), entrapped amorphous form (encapsulated in sucrose), and in aqueous solution. U-HisHCl refers to the fully protonated crystal of labeled U- ^{13}C , ^{15}N -L-histidineHClH₂O, analyzed as

received. U-His will refer to labeled L-histidine·HCl·H₂O that was adjusted to pH 7.6 ± 0.2 and resembles a non-crystalline powder. Amorphous His was formed by entrapping U-HisHCl in a sucrose solution (33% w/w) followed by flash freezing in liquid nitrogen and lyophilization.³⁹ Isotropic His was produced by dissolving U-HisHCl in a 90:10 mixture of H₂O:D₂O and adjusting to pH 4 or pH 7.6 ± 0.2 . His–FSN adsorption complexes were prepared as follows. FSN was heated at 500 °C for 15 hours to activate the silica and remove impurities and adsorbates from the surface. For SSNMR analysis, 30 mg of FSN were added to aqueous solutions of 0.05 M U-HisHCl in 2.00 mL aliquots. The pH was adjusted to pH 1, 4, 7.6, or 10 ± 0.2 using either 1 M HCl or 1 M NaOH as needed and the solutions were stirred at room temperature for 3 hours. Nanoparticles were separated by centrifugation then dried under vacuum at room temperature for over 24 hours. “Hydrated” samples were analyzed directly following preparation. While the powder appears dry, it is hydrated by physisorbed water. “Dry” samples were packed in the NMR rotor then dried under high vacuum for 4 weeks at room temperature. Rotors were capped and SSNMR experiments were carried out immediately after drying. ¹H spectra were collected at the beginning and end of dry sample analysis to verify that rehydration did not occur during data collection. A similar procedure was followed for samples prepared for TGA. His was adsorbed by adding 150 mg of FSN to a 10.00 mL aqueous solution of natural abundance L-histidine·HCl·H₂O or natural abundance pure L-histidine at various concentrations. The pH was adjusted as needed to 7.6 ± 0.2 , corresponding to the isoelectric point of His. All experiments were carried out in millipore DI water. The notation HisHCl/FSN-*x*M and His/FSN-*x*M will be used for the natural abundance adsorptions, where *x* refers to the initial His concentration (in moles per liter). U-His/FSN-*x* represents the ubiquitous isotopically (¹³C/¹⁵N) labeled His adsorptions where *x* refers to pH. A loading level of 0.05 M was selected for SSNMR analysis because prior experiments (not shown)

determined this concentration yields a fully saturated surface (approximately a monolayer) with minimal crystalline excess. NMR and TGA data support that 2 states with different properties emerge at higher loading levels. “Adsorbed” will refer to the interfacial layer of His closest to the silica surface and “excess” will refer to the remaining, bulk-like deposits that could not be removed by washing. For convenience, a table with all abbreviations and preparation methods is included in the supplemental (**Table 2.S1**).

Thermal gravimetric analysis (TGA)

TGA of His/FSN-*x*M samples were performed with a TA2910 (TA Instruments Inc.) instrument under a steady nitrogen flow (60 mL min⁻¹ for furnace and 40 mL min⁻¹ for balance). Prior to analysis, the sample was kept under N₂ flow for 30 minutes to remove weakly-bound, physisorbed water and obtain a stable baseline. A sample mass of 12–15 mg was used in each experiment and a heating rate of 5 °C min⁻¹ was applied from 25–800 °C.

Computational DFT chemical shift calculations

All computational analysis was performed with the Gaussian16 software package. Geometry optimization and NMR chemical shift tensors were calculated at the density functional level of theory (DFT) with a B3LYP 6-31G+(d,p) basis set.⁴⁰ To reduce computational costs, calculations were performed on a single His molecule. Geometry was optimized to an energy minimum without any constraints. Then a perturbation was applied to one N–H bond length and the resulting chemical shift tensors were calculated using the gauge-including atomic orbital (GIAO) method at the same level of theory.⁴¹ Geometry optimization and NMR shielding calculations were also done on tetramethylsilane (TMS) and nitromethane reference molecules

with the same basis set. Shielding values for each histidine model were converted to chemical shift using equation (1) where δ_{calc} is the calculated chemical shift for the model, σ_{ref} is the calculated shielding value of the reference (TMS for ^1H , ^{13}C and nitromethane for ^{15}N), σ_{calc} is the calculated shielding value of the model, and δ_{ref} is the experimental chemical shift of the reference (0 ppm for TMS or 380.6 ppm for nitromethane).^{18,42–44}

$$\delta_{calc} = \sigma_{ref} - \sigma_{calc} + \delta_{ref} \quad (1)$$

Solid-State NMR Spectroscopy

U-His/FSN adsorptions, U-HisHCl, U-His, and sucrose – encapsulated amorphous U-His were analyzed on a 600 MHz Bruker Avance IIIHD spectrometer equipped with a 1.9 mm triple resonance ($^1\text{H}/^{13}\text{C}/^{15}\text{N}$) probe with 30 kHz magic angle spinning (MAS) unless otherwise noted. A 300 ppm or 400 ppm spectral window (sw) was used for ^{13}C and ^{15}N experiments, respectively. Cross polarization (CP) experiments were collected using a 30% ramped pulse on ^1H and a square pulse on ^{13}C matched to the -1 Hartman Hann condition. Two pulse phase modulated (TPPM) ^1H decoupling was used in all experiments with a radio frequency (rf) field strength of 112 – 120 kHz.⁴⁵ Spectra were processed with 10 Hz exponential line broadening unless otherwise stated. ^{13}C CP-MAS experiments were collected with a 3 or 5 sec recycle delay (d1). An initial ^1H $\pi/2$ pulse of 2.25 – 2.45 μs was applied followed by a 1.75 – 2 ms ramped ^1H spin-lock pulse with a rf field strength of 97 – 118 kHz. ^{13}C direct polarization (DP-MAS) experiments were collected with varying recycle delays [0.25, 10 sec] and a ^{13}C $\pi/2$ pulse of 2.4 μs . ^{15}N CP-MAS experiments were collected at 12 kHz MAS. An initial ^1H $\pi/2$ pulse of 2.4 μs was applied followed by a 1.5 ms

ramped ^1H spin-lock pulse with a rf field strength of 83 – 104 kHz. ^{15}N DP-MAS experiments were collected with varying recycle delays [0.25, 2 sec] followed by a $5.75\ \mu\text{s}$ $\pi/2$ pulse.

Pseudo 2D saturation recovery experiments were used to measure longitudinal (T_1) relaxation of the adsorbed layer using either 16 or 12 tau delays for ^{13}C or ^{15}N , respectively. A d1 of 5 sec (pH 4) or 10 sec (pH 7.6) was used to selectively measure the fast-relaxing, adsorbed layer and remove the long relaxing bulk-like material. The saturation pulse train comprised of 128 pulses with phase cycling. A $2.5\ \mu\text{s}$ $\pi/2$ pulse was used for ^{13}C with 120 kHz ^1H decoupling during acquisition, and a $4.7\ \mu\text{s}$ $\pi/2$ pulse was used for ^{15}N experiments with 120 kHz ^1H decoupling. Spectra were processed in MestreNova and the peak integrals were exported to Matlab and fit to a single component equation. Pseudo 2D inversion recovery experiments by the Torchia method were used to obtain an estimate of T_1 relaxation of excess His.⁴⁶ Due to the inherently long relaxation of crystalline His environments it was not feasible to wait for the full decay but we were able to collect enough points to predict a T_1 several orders of magnitude larger than the adsorbed layer (~ 100 s). 10 tau delays and a d1 of 5 sec were used. Spectra were processed in MestreNova and the peak integrals were exported to Matlab and fit to a two-component equation. ^{13}C T_1 relaxation of U-HisHCl and U-His were estimated in a similar fashion and fit to a single-component equation in Matlab.

2D $^1\text{H} - ^{13}\text{C}$ heteronuclear correlation (HETCOR) and $^1\text{H} - ^{15}\text{N}$ HETCOR experiments were performed on a 400 MHz Varian VNMRS spectrometer with a 1.6 mm triple-resonance ($^1\text{H} / ^{13}\text{C} / ^{15}\text{N}$) probe at 35 kHz MAS. The CP condition for $^1\text{H} - ^{13}\text{C}$ experiments include a $1.75\ \mu\text{s}$ ^1H $\pi/2$ pulse, followed by a ramped (7%) ^1H spin-lock pulse with rf field strength of 128 kHz at the ramp maximum. For $^1\text{H} - ^{15}\text{N}$ HETCOR, the CP condition consisted of a $1.75\ \mu\text{s}$ ^1H $\pi/2$ pulse, followed by a ramped (10%) ^1H spin-lock pulse with a rf field strength of 85 kHz at the ramp

maximum with a variable contact time (0.25, 1.0, 3.0 ms). A TPPM ^1H decoupling level of 130 kHz was applied during acquisition with a 9.2° phase shift.

In all solid-state experiments the chemical shifts of ^1H , ^{13}C , and ^{15}N were indirectly referenced to adamantane ^1H (1.63 ppm), ^{13}C (38.48 ppm) and glycine ^{15}N (31.6 ppm).^{47,48} All NMR experiments were conducted at room temperature (25 °C).

Solution NMR Spectroscopy

Solution NMR experiments were performed with a 600 MHz Advance IIIHD Bruker spectrometer equipped with a 5 mm triple resonance probe operating in triple resonance ($^1\text{H}/^{13}\text{C}/^{15}\text{N}$) mode. All samples were dissolved in 90:10 $\text{H}_2\text{O}:\text{D}_2\text{O}$. ^1H and ^{13}C spectra were referenced to a 10% DSS internal standard (0 ppm) and ^{15}N spectra were externally referenced to nitromethane (380.6 ppm) in deuterated chloroform.¹⁸ ^1H 1D spectra were collected using nuclear Overhauser effect (NOE) transfer with pre-saturation during the recycle delay and mixing time to suppress water signals, 9 – 64 scans, 2 – 5 sec d1, 65536 points, and 16 – 20 ppm spectral width. ^{13}C experiments were collected using a 1D pulse sequence with a 30° flip angle and power-gated decoupling, 16 – 256 scans, 2 – 15 sec d1, 16384 – 65536 points, and 240 ppm sw. ^{15}N 1D spectra were extracted from the F_1 dimension of $^1\text{H} - ^{15}\text{N}$ heteronuclear multiple bond correlation (HMBC) experiments collected with 32 scans, 2 sec d1, 4096 points, 128 (pH 7.6) or 256 (pH 4) complex points, and a 14 ppm / 300 ppm sw in the direct/indirect dimensions. T_1 relaxation of ^{13}C was measured by inversion recovery using 4 scans, 50 sec d1, 16384 points, 12 tau delays, and 240 ppm sw.

Results and Discussion

TGA of His-FSN Complexes

Natural abundance L-His·HCl·H₂O and pure L-His were adsorbed on FSN at various concentrations (pH 7.6 ± 0.2) and analyzed with TGA. The amount of His and water adsorbed on the FSN surface can be quantified as the weight losses observed in TGA curves. As expected, surface coverage increases as loading level increases. Once all surface sites are occupied, excess His is likely deposited around the adsorbed layer as large, non-uniform solid domains and is discussed below in the SSNMR sections. In **Figure 2.1**, surface coverage is expressed as the number of adsorbed His molecules/nm² of FSN, plotted against the initial His concentration in the adsorption solution. These values are calculated using the weight loss of His from the TGA curve (100 – 800 °C) along with the BET surface area of the fumed silica surface and adjusted for our finding that 1 His molecule anchors to 2 hydroxyl groups on the surface. The quantification of adsorbed His molecules in **Figure 2.1** is similar for the HisHCl salt and neutral His starting material, indicating that the presence of salt (NaCl) does not inhibit bulk His adsorption, which was observed for L-lysine on FSN.⁴⁹ Each sample is equilibrated under N₂ flow for a minimum of 30 minutes to remove weakly bound physisorbed water. Equilibration is considered complete when a stable mass persists. Any water loss that occurs during the TGA experiment can then be attributed to the adsorption complex that includes bound water and His. Bound water loss is quantified as the weight loss between 25 – 100 °C, which remains constant (~1.3%) across all His concentrations. Interestingly, we also measure a 1.3% weight loss on bulk FSN (no His). These results support the presence of a water layer at the FSN interface following amino acid adsorption. The full TGA and DTG plots are shown in **Figure 2.S1**.

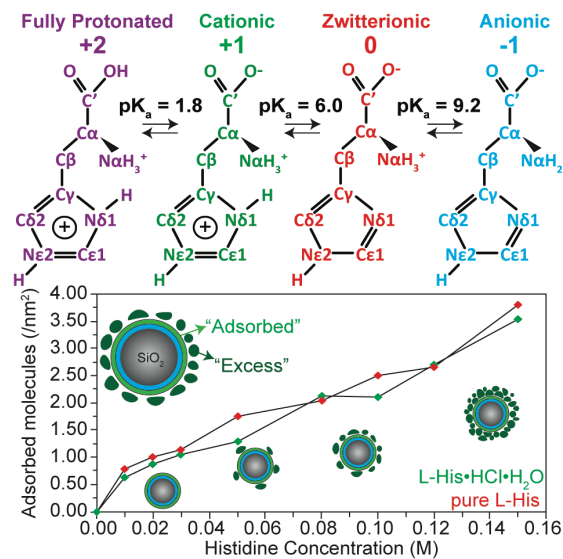


Figure 2.1. (top) Protonation states of L-His and (bottom) surface coverage of His/FSN complexes vs the concentration of the His adsorption solution at pH 7.6. Adsorbed molecules nm^{-2} for each concentration were calculated from TGA data. His/FSN complexes are depicted with an interfacial water layer (blue), His “adsorbed” layer (light green), and His “excess” or bulk-like deposits (dark green).

The first derivative (DTG) curve allows for easy visualization of the weight loss by plotting the change in weight percent vs temperature (**Figure 2.2**). A large peak centered around $60\text{ }^{\circ}\text{C}$ is attributed to evaporation of the water layer at the interface. Our focus is on the $150\text{--}250\text{ }^{\circ}\text{C}$ range where peaks are formed by water loss from thermal condensation reactions between neighboring molecules.⁵⁰⁻⁵² Peptide bond formation through this mechanism has been observed for a number of amino acids adsorbed on FSN including Gly, Ala, Lys, Leu, Glu, Asp, and Phe.⁵⁰⁻⁵⁴ We observe a thermal condensation reaction between adjacent His molecules $\sim 170\text{ }^{\circ}\text{C}$ in HisHCl/FSN adsorptions and $\sim 160\text{ }^{\circ}\text{C}$ in His/FSN adsorptions. The peak temperature is consistent across all concentrations of HisHCl/FSN and His/FSN adsorptions. However, when natural abundance bulk His is heated without silica, this thermal transition does not occur. It is important to point out that a sharp peak at $171\text{ }^{\circ}\text{C}$ is observed for bulk His·HCl·H₂O due to the evaporation of lattice water

in the crystal.⁵⁵ This should not be confused with a thermal condensation reaction, which was verified by solution NMR of heated bulk L-His·HCl·H₂O (**Figure 2.S2**). The intensity of the thermal condensation peak ~165 °C increases as concentration increases up to 0.10M. The area under this condensation peak then remains constant as concentration increases from 0.10 – 0.15M (**Figure 2.2**). This result agrees with previous findings that suggest silica plays a key role in promoting amino acid thermal condensation reactions.^{27,38,56-58} A second peak ~210 °C is observed at HisHCl/FSN concentrations above 0.12M and in His/FSN adsorptions above 0.05M. This is likely due to a second thermal condensation reaction, possibly resulting in the diketopiperazine (DKP) or cyclic dimer product. It is interesting to note that the second thermal condensation peak appears at much lower concentrations in the zwitterionic His sample and only arises in high (> 0.12M) concentrations of HisHCl. One possibility for this phenomenon could be that a low presence of salt (NaCl) stabilizes the thermal condensation product and inhibits or prevents it from readily undergoing a second condensation reaction. A full characterization of these products is underway and will be discussed in a follow up manuscript. The last peak ~ 270 °C is due to decomposition of histidine molecules.

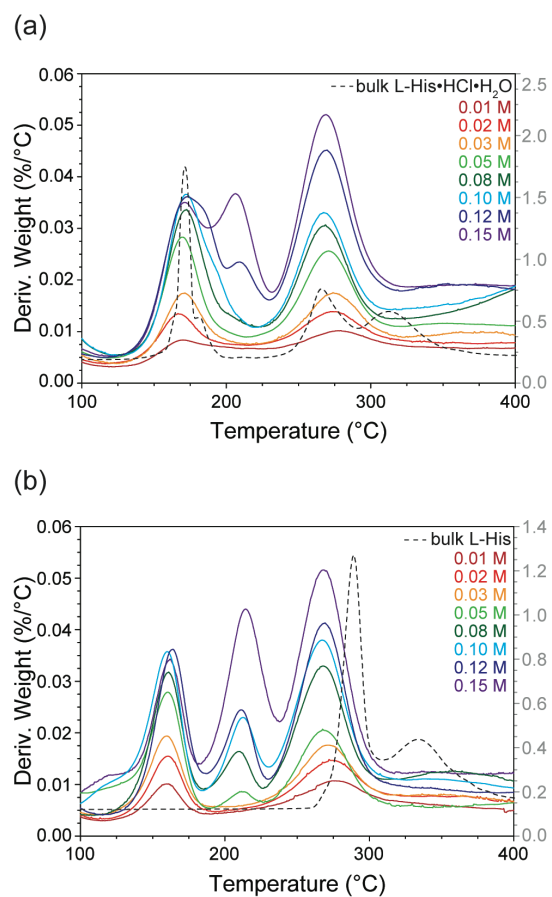


Figure 2.2. First derivative DTG curves are displayed for His/FSN complexes as a function of adsorption solution concentration. DTG curves for the (a) HCl salt and (b) bulk L-His adsorption complexes.

NMR Characterization of His Structure and Dynamics on FSN in the Hydrated State

The protonation states of His are shown in **Figure 2.1 (top)**. ¹³C and ¹⁵N CP-MAS NMR spectra were collected on U-HisHCl and U-His samples to determine chemical shifts of His in fully protonated and zwitterionic forms which are in good agreement with literature values⁵⁹ (**Table 2.1**). U-HisHCl has a uniform and rigid crystalline structure and shows good CP efficiency and sharp resonances with enough resolution to measure J_{CC}-coupling. Some line broadening and reduced signal to noise is observed for the zwitterionic U-His form where crystal packing has been

disrupted. **Figure 2.3** shows ^{13}C and ^{15}N CP-MAS NMR spectra of U-HisHCl, U-His, and U-His/FSN in the hydrated state at near neutral and an acidic pH 4. In acidic conditions (pH 4), seven carbon resonances are observed. Six of the resonances agree with the chemical shifts for U-HisHCl (**Table 2.1**). An additional resonance is observed for site $\text{C}_{\epsilon 1}$ indicating differences in the electronic environment between adsorbed and excess His. One possibility why only the $\text{C}_{\epsilon 1}$ adsorbed resonance is unique could be because this carbon neighbors 2 nitrogens in the imidazole ring and could be most impacted by changes due to imidazole ring hydrogen bonding and interactions with the water layer on the FSN surface. ^{15}N CP-MAS NMR agrees with the ^{13}C data, showing a set of sharp resonances that match U-HisHCl indicating protonated, well-ordered excess His, and an additional set of unique resonances that are attributed to the adsorbed layer. $\text{N}_{\alpha, \text{ads}}$ at pH 4 is shifted upfield which is likely caused by hydrogen bond interactions with water and/or the FSN surface. Sharp lines of the adsorbed layer at acidic pH 4 are due to enhanced liquid-like dynamics at the interface and will be discussed further in the dynamics section below where NMR relaxation times are reported and discussed. Lastly, it is clear from the NMR data that binding to the surface is stronger and His is less dynamic when adsorbed in zwitterionic form as evidenced by the considerably broader lines and further supported by the relaxation measurements discussed below.

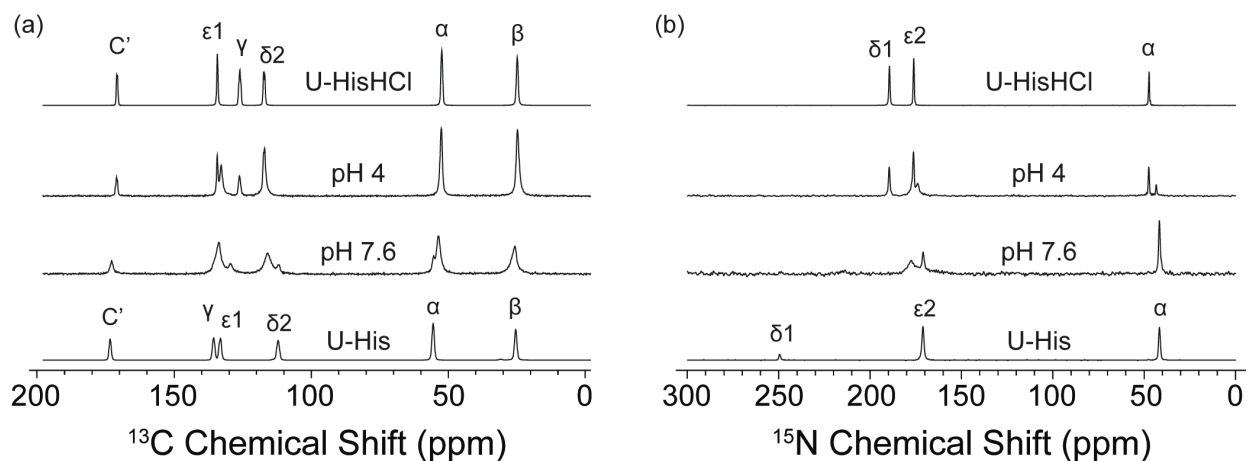


Figure 2.3. (a) ^{13}C CP-MAS and (b) ^{15}N CP-MAS NMR spectra of crystalline U-HisHCl, U-His, and U-His/FSN at pH 4 and pH 7.6 in the hydrated state. U-HisHCl was analyzed as received, and U-His was prepared by adjusting U-HisHCl to pH 7.6.

At pH 7.6, unique ^{13}C resonances are observed for multiple sites suggesting that adsorbed and excess groups are no longer chemically equivalent. ^{13}C and ^{15}N chemical shifts of excess His are easily determined by varying His concentration and watching the peak intensities of the sharp components vary (data not shown). The chemical shifts of excess His agree with U-His, indicating that bulk His is zwitterionic at pH 7.6 as would be expected since the excess material is crystallized from a near neutral pH solution. ^{13}C sites are significantly broadened due to chemical shift heterogeneity from tighter binding in the adsorbed layer as well as variation in protonation states. C_β broadens the most with a full width at half maximum (FWHM) of 320 Hz, compared to 180 Hz for C_β at pH 4. $\text{N}_{\delta 1}$ shows the largest shift (~ 50 ppm) from U-HisHCl to U-His because it is the site that becomes deprotonated. Resonances of the adsorbed layer shift toward U-HisHCl but do not reach these values, probably due to partial hydrogen bonding of the imidazole ring or differences in hydrogen bond strength where the crystalline form is expected to have the strongest hydrogen bonding and thus, largest chemical shift changes. To support this assessment, DFT

chemical shift calculations were performed on simplified His models to observe the effect of hydrogen bond strength on chemical shift (**Figure 2.S3**). After geometry optimization, either the N ϵ ₂-H or N δ ₁-H bond was stretched systematically up to 2 Å. The calculated chemical shielding values of the molecule were converted to chemical shift using equation (1). A nearly linear relationship between ¹⁵N chemical shift and N-H bond distance is observed for the imidazole nitrogens for both protonated and zwitterionic His forms. However, N α is largely unaffected by N ϵ ₂-H and N δ ₁-H perturbations.

Table 2.1. ¹³C and ¹⁵N SSNMR chemical shifts of bulk His in protonated (U-HisHCl) and zwitterionic (U-His) forms, and adsorbed (ads) and excess (exc) layers of U-His/FSN complexes in the hydrated state at near neutral pH and pH 4. Solution NMR chemical shifts are also listed for aqueous (isotropic) His at pH 4 and pH 7.6. The chemical shifts were extracted from a combination of CP-MAS and DP-MAS experiments presented in Figure 2.3 and Figure 2.5 and are reported in ppm.

	Site	U-HisHCl	U-His	Isotropic His (pH 4)	Isotropic His (pH 7.6)	U-His/FSN-4		U-His/FSN-7.6	
						His _{ads}	His _{exc}	His _{ads}	His _{exc}
¹³ C	C'	172.9	175.3	172.6	174.2	173.4	173.0	174.8	175.4
	C ϵ 1	136.3	135.1	134.0	136.5	134.9	136.3	136.1	135.5
	C γ	128.2	137.7	127.5	132.2	128.4	128.2	131.5	137.4
	C δ 2	119.3	114.3	117.6	116.9	119.0	119.1	118.0	113.8
	C α	54.4	57.6	53.6	55.0	54.7	54.5	55.6	57.3
	C β	26.9	27.3	25.8	28.3	26.4	26.7	28.4	27.4
¹⁵ N	N δ 1	189.4	249.4	177.1	233.0	177.3	189.5	216.6	249.6
	N ϵ 2	176.1	171.1	174.1	178.3	174.0	176.2	178.1	171.1
	N α	47.2	41.5	40.8	40.2	43.6	47.4	41.7	41.8

Under acidic conditions (pH 4), His is positively charged and the FSN surface is neutral and terminated by hydroxyls.⁶⁰ Electrostatic repulsion among His molecules on a neutral surface would then provide an unfavorable binding environment and lead to a highly dynamic adsorbed layer under hydrated conditions. This is likely the reason for the sharp, liquid-like line shapes observed in ¹³C and ¹⁵N CP-MAS spectra at low pH (**Figure 2.3**). To investigate this further, ¹³C direct polarization experiments were collected at 30 kHz MAS with high power decoupling, 30 kHz MAS with no decoupling, and no MAS with high power decoupling (**Figure 2.4**). At pH 4, ¹J_{CC} coupling constants are measured ~ 50 Hz for C', C_γ, and C_{δ2} in DP-MAS spectrum with high-powered decoupling (**Figure 2.4, "DP-MAS"**). When decoupling is turned off, ¹J_{CH} coupling constants can be measured at pH 4 indicating liquid like behavior, whereas no decoupling on U-His/FSN-7.6 exhibits much broader lines with an inability to resolve ¹J_{CH} coupling constants (**Figure 2.4, "HPD off"**). Static DP experiments also confirm that the adsorbed layer is bound more tightly at pH 7.6. MAS is used in SSNMR to average out chemical shift anisotropy and dipolar coupling which are inherently averaged by the isotropic tumbling of liquids in solution NMR. U-His/FSN-7.6 collected under static conditions shows significant line broadening compared to pH 4 due to the reasons stated above, which is expected for a more rigid, dynamically restricted sample. However, U-His/FSN-4 resonances exhibit minimal line broadening under static conditions and 6 carbon peaks are still clearly observed. Molecular tumbling must be present to some degree to average out these effects and produce resolvable resonances under static conditions.

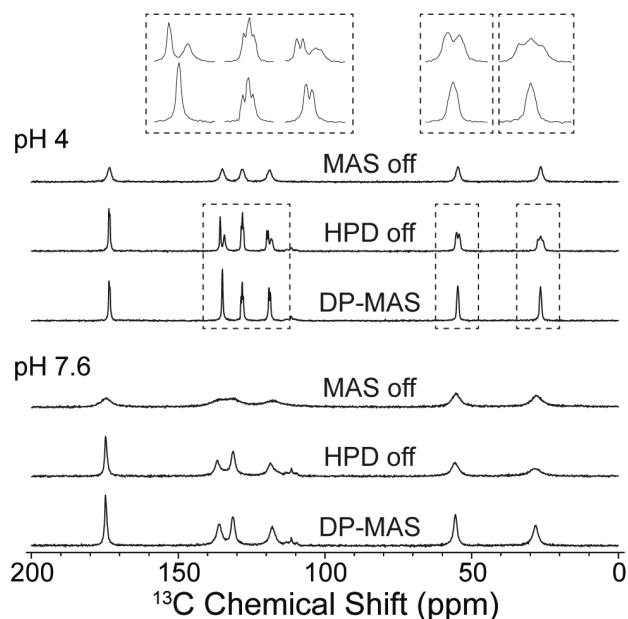


Figure 2.4. ^{13}C DP-MAS of U-His/FSN-4 and U-His/FSN-7.6 in the hydrated state collected with 30 kHz MAS and high-power decoupling (DP-MAS), 30 kHz MAS and no decoupling (HPD off), and no MAS with high-power decoupling (MAS off). U-His/FSN-4 spectra are blown up in the inset to show the J-splitting. A 2 s recycle delay was used and no line broadening was applied.

^{13}C T_1 relaxation measurements also support tighter binding to the silica surface for U-His/FSN-7.6 compared to U-His/FSN-4. T_1 was measured for hydrated U-His/FSN-1, U-His/FSN-4, and U-His/FSN-7.6 using saturation recovery, details displayed in **Figure 2.S4**. On average, T_1 increases as pH increases for all ^{13}C sites measured at room temperature. A complete list of ^{13}C T_1 values are reported in **Table 2.2**. T_1 relaxation is ~ 0.5 sec for most ^{13}C sites at pH 4 and increases to ~ 1.6 sec at pH 7.6. Longer T_1 relaxation is consistent with restricted motion and tighter binding interactions proposed for U-His/FSN-7.6. ^{13}C T_1 relaxation at room temperature for U-His/FSN-4 and U-His/FSN-7.6 are near the T_1 minimum, confirmed by variable temperature experiments (not shown). Since His_{ads} is near the T_1 minimum, we estimate a rotational correlation time for adsorbed His in a hydrated state to be ~ 5 ns in a 600 MHz (150 MHz ^{13}C) magnetic field.⁶¹

^{13}C T_1 relaxation was estimated using CP inversion recovery for excess His, U-HisHCl, and U-His. A CP based experiment was necessary since the relaxation of ^1H is considerably shorter than ^{13}C in crystalline states. Even with the faster relaxation of ^1H , it was not feasible for the delay list to encompass the full signal decay of ^{13}C . Enough points were collected to estimate excess His T_1 at two to three orders of magnitude greater than the adsorbed layer and in line with the long T_1 observed for His as a rigid solid. T_1 relaxation of aqueous His, amorphous His, and solid His (protonated and zwitterionic) were also measured for comparison.

Amorphous His (pH 7.6), interestingly, has an average T_1 that falls in between the very rigid crystal and highly dynamic adsorbed layers. ^{13}C and ^{15}N CP-MAS experiments of amorphous His were collected with varying number of scans and recrystallization was observed as scans increased. This is due to sample heating from MAS rotation and high-power ^1H decoupling that provides enough energy for the disperse His molecules (only 33% w/w) to rearrange into the energetically favorable crystalline form. Rotameric conformers are present in His at neutral pH⁵⁹ so additional enhanced dynamics must be contributing to reduced T_1 relaxation in the amorphous state. T_1 was also determined for aqueous His in a standard solution state at pH 4 and pH 7.6 where the molecular tumbling rate is rapid and T_1 relaxation gets longer. pH did not impact relaxation rates of His in a liquid state and ranged from 1 – 12 sec for each ^{13}C site with the C_β , C_α , and $C_{\delta 2}$ on the order of 1-2 s. The latter further supports the near isotropic mobility of the adsorbed layer of U-His/FSN-4 in the hydrated state where the same sites have $T_1 \sim 0.5\text{s}$.

Table 2.2. ^{13}C longitudinal (T_1) relaxation reported in seconds for hydrated His/FSN and standard His samples in solid and aqueous states at pH 4 and 7.6.

Site	U-His/FSN-4		U-His/FSN-7.6		U-HisHCl	U-His	Amorphous His (pH 7.6)	Isotropic His (pH 4)	Isotropic His (pH 7.6)
	His _{sads}	His _{exc}	His _{sads}	His _{exc}					
C'	0.46	101	1.71	105	157	108	26	12	12
C ϵ 1	0.52	142	1.45	53	197	221	24	2	2
C γ	0.61	105	1.64	22	196	216	17	9	7
C δ 2	0.57	115	1.74	58	197	220	22	2	2
C α	0.43	51	1.61	11	54	45	21	2	2
C β	0.42	52	1.76	7	57	48	22	1	1

In U-His/FSN-4 and U-His/FSN-7.6 hydrated samples, T_1 of the adsorbed layer is several orders of magnitude shorter than excess His. We used this large difference in relaxation to isolate the adsorbed layer resonances by collecting ^{13}C and ^{15}N DP-MAS with a short recycle delay to saturate and remove signals from the excess, crystalline-like deposits. With a 0.25 sec recycle delay, 6 carbon peaks are distinguished in both samples. All sites are fully relaxed when the recycle delay is increased to 1 sec. Each resonance corresponds to one unique carbon site in a histidine molecule and should integrate to 1 when fully relaxed (maximum signal achieved). Similarly, ^{15}N DP-MAS experiments with a 0.25 sec recycle delay show 3 resonances for ^{15}N which represent the nitrogen shifts of the adsorbed layer; these sites are fully relaxed (integrate to 1) after a 2 sec recycle delay. At pH 4, excess His chemical shifts are nearly identical to U-HisHCl indicating that excess His is protonated and has a similar packing structure to crystalline U-HisHCl. The excess is so well ordered that C' and C δ 2 resonances are sharp enough to observe homonuclear J_{CC} -coupling. C ϵ 1,ads is shifted from the excess layer, causing 7 peaks to be observed in CP-MAS. The “fast repetition” or short recycle delay DP-MAS experiments reveal only 6 resonances which correspond to the resonances of the adsorbed layer. This establishes that the upfield C ϵ 1 peak at

134.9 ppm, which persists in DP-MAS, originates from the adsorbed layer and the downfield $C_{\epsilon 1}$ peak at 136.3 ppm (identical chemical shift to U-HisHCl $C_{\epsilon 1}$) is from the excess layer.

Fast repetition ^{15}N DP-MAS experiments were needed to resolve U-His/FSN-4 chemical shifts of adsorbed $N_{\delta 1}$ and $N_{\epsilon 2}$ that are convoluted with excess His in the CP-MAS spectrum. Perturbations in resonance chemical shifts are more apparent in the ^{15}N dimension because the chemical shift range is larger (300 ppm) and because nitrogen sites are directly involved in hydrogen bonding interactions that perturb its electronic environment more so than ^{13}C . The isotropic peaks of the imidazole nitrogen sites are nearly indistinguishable at acidic pH suggesting that their chemical environments are nearly identical. Isotropic $N_{\delta 1}$ and $N_{\epsilon 2}$ differ by only 2 ppm at pH 4 due to molecular tumbling and near isotropic dynamics which make the electronic environment of the 2 protonated sites nearly equivalent. In solid U-HisHCl, where motion is restricted, the protonated imidazole nitrogens differ by 13 ppm. In the adsorbed layer of U-His/FSN-4, $N_{\delta 1}$ shifts upfield by 12 ppm and is only 3.3 ppm away from $N_{\epsilon 2}$. This trend supports the proposal of a highly dynamic, liquid-like adsorbed layer at pH 4. The imidazole ring is fully protonated, His molecules are likely experiencing charge-charge repulsion leading to increased dynamics with no preferred binding orientation, which is evidenced by the ^{13}C and ^{15}N chemical shifts close to the isotropic values (marked by blue dashed lines in **Figure 2.5**). $N_{\alpha, \text{ads}}$ is also shifted upfield from the U-HisHCl crystal but does not quite reach the isotropic shift. A small residual $N_{\alpha, \text{exc}}$ peak comes through in the DP-MAS spectrum because NH_3 undergoes free rotation and is inherently more dynamic (and thus faster relaxing) than amides and other amine bonds even in crystalline solids.⁶²

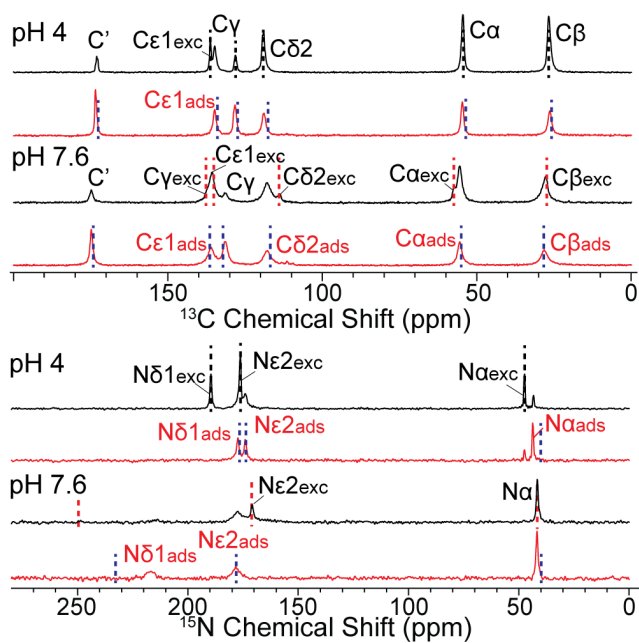


Figure 2.5. ^{13}C and ^{15}N (black) CP-MAS and (red) DP-MAS SSNMR spectra of hydrated 0.05M-UHis/FSN samples at pH 4 and pH 7.6. CP-MAS spectra show all signals, while DP-MAS collected with a fast recycle delay selects only the adsorbed layer. Black dashed lines show chemical shifts of U-HisHCl (cationic), red dashed lines show U-His (zwitterionic), and blue dashed lines show chemical shifts of isotropic His at each respective pH.

In hydrated U-His/FSN-7.6 multiple adsorbed ^{13}C resonances are now visible in ^{13}C CP-MAS spectrum (**Figure 2.5, black**), indicating that adsorbed and excess states are quite different. The CP-MAS peaks of excess His are in agreement with zwitterionic U-His (red lines) and are slightly broadened compared to excess His of U-His/FSN-4 suggesting that the excess does not pack uniformly when deprotonated. $\text{N}_{\delta 1, \text{exc}}$ is not visible at this low loading level (since $\text{N}_{\delta 1}$ at pH 7.6 is deprotonated and does not have a close proton spin bath) but a peak at 249.6 ppm is observed at higher His concentrations (0.10M and 0.15M) and agrees with literature values for $\text{N}_{\delta 1}$ in U-His.⁵⁹ The adsorbed state (**Figure 2.5, red**) also experiences line broadening from a distribution of chemical environments (chemical shift heterogeneity). Similar to U-His/FSN-4, the resonances of the adsorbed layer resemble that of the isotropic state. It is important to note that the chemical

shifts of isotropic His were collected in a hydrogen bonding environment and it is probable that both the isotropic and adsorbed states are involved in hydrogen bonding with water. The $N_{\epsilon 2,ads}$ peak from DP-MAS has the same chemical shift as isotropic $N_{\epsilon 2}$ and displays large degrees of heterogenous line broadening. Many correlations with water (~ 4.7 ppm) are observed in $^1H - ^{13}C$ and $^1H - ^{15}N$ HETCOR experiments (**Figure 2.S5**), supporting TGA data that a water layer exists at the silica interface even following His adsorption. Additionally, Guo et al showed that alanine adsorbed on FSN exchanges with water in a hydrated environment thus, direct water-amino acid interactions appear to be present for different amino acids and are not unique to the observations for His.⁵⁰ It is also worth noting that a small broadening upfield of the $N_{\epsilon 2,exc}$ peak is observed in the CP-MAS spectrum and is more apparent in 2D $^1H - ^{15}N$ HETCOR, but is not observed in DP-MAS. This is likely due to $N_{\epsilon 2,ads}$ shifted from interaction with silanols and is discussed in the later section.

NMR Characterization of His Structure and Dynamics on FSN in the Dried State

U-His/FSN-4 and U-His/FSN-7.6 were analyzed in a dried state to observe direct interactions with the silica surface by removing the interfacial water layer. Full $^1H - ^{13}C$ and $^1H - ^{15}N$ HETCOR spectra of dried U-His/FSN-7.6 can be found in **Figure 2.S6**. T_1 relaxation of the adsorbed layers of both samples increase beyond the point of observation in the fast repetition DP-MAS experiments but, were too broad to measure T_1 in a reasonable timeframe. Instead, the chemical shifts of the adsorbed layer were extracted from ^{13}C and ^{15}N CP-MAS spectra where each peak area was fit to 2 components in MestreNova (**Figure 2.6, 2.7**). The sharp components correspond to excess His which show no change from the hydrated state, and broad components represent the adsorbed His. With water removed, the previously dynamic adsorbed layer of U-

His/FSN-4 is now restricted and interaction with the FSN surface is observed. Adsorbed peaks broaden significantly due to a distribution of chemical environments from tighter binding and reflect a degree of disorder in the binding modes. In the adsorbed layer, C' , $C_{\epsilon 1}$, C_{α} , and N_{α} have negligible changes in chemical shift upon drying (<1ppm) and C_{γ} , $C_{\delta 2}$, C_{β} , $N_{\delta 1}$, $N_{\epsilon 2}$ shift slightly (1-2 ppm). All chemical shifts for dried samples are listed in **Table 2.3** and the deconvoluted CP-MAS spectra are shown in **Figure 2.6**. Protonation state stays the same and negligible changes in chemical shifts suggest that drying locks in a similar environment however, because of slower dynamics there is likely a larger distribution of hydrogen bond lengths and strengths that is reflected by the line broadening.

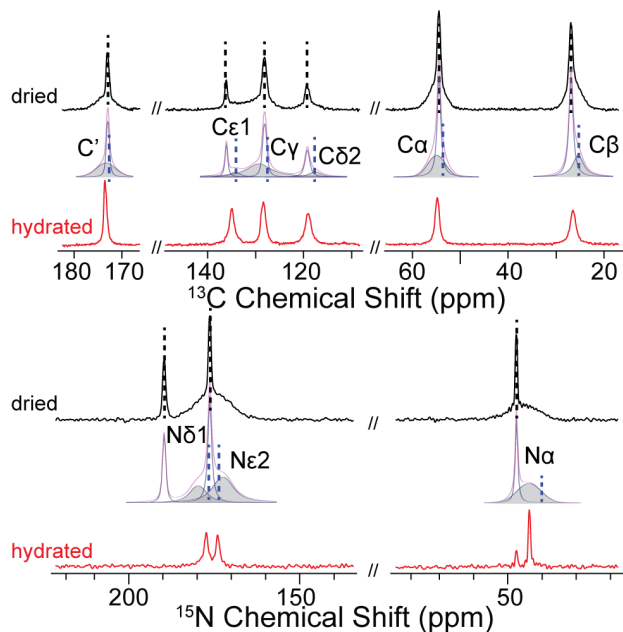


Figure 2.6. ^{13}C and ^{15}N spectra of 0.05M U-His/FSN-4 in a hydrated (red) and dried (black) state. ^{13}C and ^{15}N DP-MAS (red) with fast recycle delay show only the adsorbed layer in the hydrated state. ^{13}C and ^{15}N CP-MAS (black) of the dried state are presented along with the deconvolution from MestreNova to highlight the adsorbed layer. U-HisHCl resonances (black) and isotropic His at pH 4 (blue) resonances are indicated by the dashed lines.

Broadening is also observed in the adsorbed layer of U-His/FSN-7.6 with removal of water. Each peak area was fit to 2 components with the exception of C', N_α, and N_{ε2}/N_{δ1} which required 3 peaks for a proper fit. Excess His is unchanged upon drying. **Figure 2.7** compares the adsorbed layer at pH 7.6 in hydrated, dried, and amorphous states (His encapsulated in sucrose). The chemical shifts, line widths, and peak shapes of the dried adsorbed layer are well represented by amorphous His, which was synthesized to examine if packing arrangement had any effect on chemical shift. At pH 7.6 His is in the zwitterionic form (N_{δ1} deprotonated) and is likely interacting with neighboring sucrose molecules as a hydrogen bond acceptor. Hydrogen bond strength has a strong effect on chemical shift and distribution of hydrogen bond interactions is likely contributing to the observed line broadening. Amorphous C_{ε1} exhibits a broad asymmetric peak that can be deconvoluted into multiple sites resulting from overlap of C_{ε1} and C_γ resonances of cationic and zwitterionic forms. C_γ shifts downfield 10 ppm when N_{δ1} gets deprotonated and this region contains the most overlap (refer to **Figure 2.1 U-HisHCl and U-His**). Unique to the dried U-His/FSN-7.6 sample is an additional adsorbed resonance for C', N_α, and N_{δ1}/N_{ε2} (175.2 ppm). The ¹⁵N peak at 164.6 ppm is assigned to N_{ε2} shifted upfield due to interaction with the FSN surface. This peak is detailed as a 2D HETCOR correlation (**Figure 2.8**) and is observed in both hydrated and dried environments. The ¹⁵N resonance at 175.2 ppm, however, is ambiguous and two possibilities are presented.

Option (1): The ¹⁵N resonance at 175.2 ppm is assigned to protonated N_{δ1,ads}. Drying locks in 2 forms and N_{δ1} becomes either fully deprotonated or fully protonated but both forms are present. N_{δ1} is split into 2 peaks (shifted by ~ 50 ppm) and each N_{δ1} peak has a small area because it is split into 2 forms. The difference in N_{ε2} chemical shift between U-HisHCl and U-His is only a few ppm

so a single peak is observed with a large area and linewidth that encompasses $N_{\epsilon 2}$ in both protonation states. $N_{\epsilon 2}$ is shifted upfield due to strong hydrogen bonding with the FSN surface. This is believed to be more likely because both forms are present in the hydrated state measured by the large exchange rate of $N_{\delta 1}$. The relative peak areas are also consistent with this idea. C' and N_{α} exhibit an additional resonance because they are also interacting with the silica surface, which has been confirmed by ^1H slices from HECTOR experiments (**Figure 2.8**). Mudunkotuwa et al proposed a model of His adsorbed on TiO_2 nanoparticles based on infrared (IR) spectroscopic analysis, where surface interactions occur through $N_{\epsilon 2}$ and N_{α} .⁶³ Thus, it appears that both protonated and deprotonated His are present in the dried adsorbed layer so 2 resonances are observed for $N_{\delta 1}$, N_{α} , and C' . The peak at 175.2 ppm is $N_{\delta 1, \text{ads}}$ and is the protonated form and His binds to the FSN surface through hydrogen bonding with $N_{\epsilon 2}$, and N_{α} or C' .

Option (2): 175.2 ppm is assigned to $N_{\epsilon 2}$ not interacting with silica. Drying removes $H_{\delta 1}$ and locks in the neutral form. $N_{\epsilon 2}$ is split into 2 resonances: $N_{\epsilon 2}$ at 175.2 ppm is closer to hydrated $N_{\epsilon 2}$ (178.1 ppm) and U-His $N_{\epsilon 2}$ (171.1 ppm) where the ring is deprotonated and His is not interacting with the silica surface. $N_{\epsilon 2}$ at 164.6 ppm is shifted upfield from interacting with silanols. N_{α} and C' also show 2 resonances for the adsorbed layer, which could support that there is a population of molecules interacting with the silica surface and a population that is not interacting with the silica surface. This is believed to be less likely because U-His/FSN-7.6 has a stronger interaction with the surface in the hydrated state so removal of the water layer should cause all His molecules to interact with silica. In this situation, drying removes $H_{\delta 1}$ and only neutral His is present but 2 populations exist: one binding to FSN through $N_{\epsilon 2}$, and N_{α} or C' . The other population does not interact with FSN.

Table 2.3. ^{13}C and ^{15}N NMR chemical shifts of U-His/FSN complexes at pH 4 and 7.6 in dried and hydrated states. The chemical shifts of dry samples were determined by deconvolution in MestreNova. In cases where the adsorbed component could not be fit to a single peak, bold chemical shifts represent environments that interact with the FSN surface.

	Site	U-His/FSN-4 dry		U-His/FSN-4 hydrated		U-His/FSN-7.6 dry		U-His/FSN-7.6 hydrated	
		His _{ads}	His _{exc}	His _{ads}	His _{exc}	His _{ads}	His _{exc}	His _{ads}	His _{exc}
^{13}C	C'	173.2	172.8	173.4	173.0	173.6 , 179.5	175.5	174.8	175.4
	C ϵ 1	134.3	136.0	134.9	136.3	134.2	135.6	136.1	135.5
	C γ	131.3	128.1	128.4	128.2	127.5	137.5	131.5	137.4
	C δ 2	117.4	119.2	119.0	119.1	116.4	113.9	118.0	113.8
	C α	55.1	54.4	54.7	54.5	55.1	57.4	55.6	57.3
	C β	25.2	26.8	26.4	26.7	28.0	27.5	28.4	27.4
^{15}N	N δ 1	179.7	189.6	177.3	189.5	243.0, 175.2	249.0	216.6	249.6
	N ϵ 2	172.4	176.3	174.0	176.2	175.2, 164.6	170.8	178.1, 164.6	171.1
	N α	43.8	47.4	43.6	47.4	44.0 , 38.4	41.4	41.7	41.8

Proposed Atomic Binding Model for His/FSN Adsorption Complexes

In the hydrated state, the adsorption site for U-His/FSN-7.6 exhibits chemical shifts that are close to His in an isotropic solution at near neutral pH while, the excess layer agrees with U-His in the solid state (**Table 2.1**). Interactions with water molecules at the silica surface for the adsorption site in the hydrated state are confirmed with $^1\text{H} - ^{13}\text{C}$ and $^1\text{H} - ^{15}\text{N}$ HETCOR spectra (**Figure 2.8**). These water interactions are for the most part absent in the dry form. This type of hydrogen bonding arrangement is in agreement with that proposed by Mudunkotuwa et al for His adsorbed on TiO_2 nanoparticles where $\text{N}_{\delta 1}$ orients away from the silica surface allowing for strong interactions with water.⁶³ This is clearly observed in the hydrated state by $^1\text{H} - ^{15}\text{N}$ HETCOR where a strong correlation with water is observed in the ^1H dimension at 5.3 ppm (**Figure 2.8Dd**). C' also interacts with water in the hydrated state where the $\text{H}_2\text{O} - \text{C}'$ correlation is readily observed at 5.0 ppm (**Figure 2.8Fe**) although it appears weaker compared to that observed for $\text{N}_{\delta 1, \text{ads}}$. At pH

7.6 in the dried state, strong hydrogen-bonding to the silica surface is supported for some sites where the $N_{\epsilon 2}$ shifts upfield to 164.6 ppm with considerable line broadening observed in 1D ^{15}N CP-MAS (**Figure 2.7**) and 2D HETCOR (**Figure 2.8D**). $H_{\epsilon 2}$ shifts upfield from 13.6 to 10.9 ppm (**Figure 2.8De and Df**) and H_3-N_{α} correlation shifts upfield from 8.7 to 8.0 ppm (**Figure 2.8Ee and Ed**), leaving $N_{\delta 1}$ and C' to interact with water with clear correlations at 5.3 ppm (**Figure 2.8Dd**) and 5.0 ppm (**Figure 2.8Fe**). Correlations to water at 4.7 ppm are also observed for N_{α} (**Figure 2.8Ed**) and at 5.3 ppm for $N_{\epsilon 2}$ (**Figure 2.8Df**) suggesting they are exchanging with water in addition to interacting with silica. Intermolecular interactions are observed between C' and a neighboring $H_{\epsilon 2}$ (**Figure 2.S7**) when the CP contact pulse is increased to 2 ms, suggesting horizontal alignment of His molecules along the surface providing intermolecular connectivity. This type of spatial arrangement would allow for pi-pi interactions between neighboring imidazoles along the surface which preferentially form in water due to higher stability.⁶⁴ The later will need to be confirmed by future studies but, is an interesting hypothesis.

The adsorbed layer of dried U-His/FSN-7.6 broadens considerably due to chemical shift heterogeneity and restricted motion from removal of water. The HETCOR correlations to water at 5.3 ($N_{\delta 1}$), 5.0 (C'), and 4.7 ppm (N_{α}) vanish. The proton chemical shifts of $H_{\epsilon 2}$ and H_3-N_{α} shift upfield from 13.6 ppm to 11.1 ppm (**Figure 2.8Ab and Ac**) and from 8.8 ppm to 8.2 ppm (**Figure 2.8Bb and Ba**), respectively, due to interactions with FSN. Additional resonances in the adsorbed layer are observed in dried ^{13}C and ^{15}N CP-MAS NMR spectra. However, no correlation to ^1H was observed in the F_1 dimension of C' at 179.5 ppm (**Figure 2.8Ca**) suggesting that the C' in this environment is isolated from any proton spin bath. The C' resonance at 173.6 ppm has a broad ^1H correlation roughly centered ~ 7 ppm (**Figure 2.8Cc**) that is assigned to silanol interactions. Both $N_{\alpha,\text{ads}}$ peaks at 44.0 ppm and 38.4 ppm (**Figure 2.8Ba and Bc**) exhibit broadening in 2D HECTOR

and both ^1H slices shift upfield and could be interacting with silica. The N_α resonances of protonated and deprotonated His are 47.2 and 41.5 ppm, which agree with our proposal for the ^{15}N peak at 175.2 ppm where both protonation states are present and the resonances are shifted by SiO^- interactions. **Figure 2.9** summarizes the proposed model for His interacting with the FSN surface in hydrated and dried environments at pH 4 and 7.6.

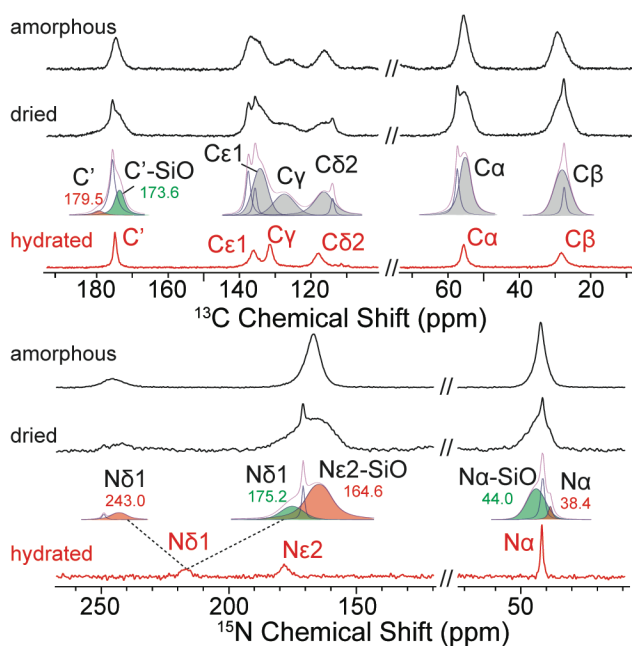


Figure 2.7. ^{13}C and ^{15}N CP-MAS NMR spectra of hydrated and dried 0.05M U-His/FSN-7.6 and amorphous His adjusted to pH 7.6. Red spectra are DP-MAS of the hydrated form with fast (1s for ^{13}C , 2s for ^{15}N) recycle delays. Black spectra are CP-MAS.

Comparison of His adsorption environment on silica to other amino acids

When zwitterionic His is adsorbed to FSN (pH 7.6), His anchors the silica surface by hydrogen bonding to silanol groups at two or three contact points: $N_{\epsilon 2}$, $N_{\alpha}H_3^+$, and/or COO^- (**Figure 2.9**). Since the His R-group contains multiple hydrogen bonding sites and His has a planar shape, molecules can arrange horizontally along the surface, which is unique from other more simplistic amino acid such as Gly and Ala. The His binding and dynamics is dependent on hydration level and the pH of the adsorption solution. Near liquid-like dynamics and a nonpreferred binding is observed in acidic conditions regardless of hydration level, while at near neutral pH His has a more preferred binding arrangement for both hydrated and dry samples with the dry sample being more rigid. For Gly and Ala, which are the two simplest amino acids with non-polar side chains, anchoring is observed through the amine group when adsorbed on MSN.⁶⁵ The organization of Gly on FSN was also studied and shown to adsorb in zwitterionic form through hydrogen bonding of NH_3^+ to surface silanols (except below pH 2).⁶⁶ Alanine adsorbed on FSN was found to anchor through the amine moiety in hydrated environments similar to Gly, but both amine and carboxyl groups hydrogen bond the surface when water is removed.⁵⁰ Lysine binds FSN silanols almost exclusively through hydrogen bonding of the side chain amine group and exhibits a well-ordered vertical arrangement with the amino acid backbone terminal.⁴⁹ Overall this series of studies on different amino acids on FSN and other silica substrates illustrate that for small, non-polar amino acids (Gly and Ala) the only possible anchor points are the amine or carboxyl depending on pH and hydration. For larger, polar amino acids such as His multiple points of contacts are present, and the bonding arrangement is more complex with bonding through three contact points as shown in **Figure 2.9**. This illustrates the importance of individual amino acid studies and shows the diversity of binding to silica nanoparticle surfaces particularly when more

complex amino acids like Lys and His are considered. It also highlights the impact of hydration level and adsorption solution pH on the anchoring, organization of amino acids at silica nanoparticle interfaces and that SSNMR is a powerful tool to elucidate their molecular characteristics at an atomic level.

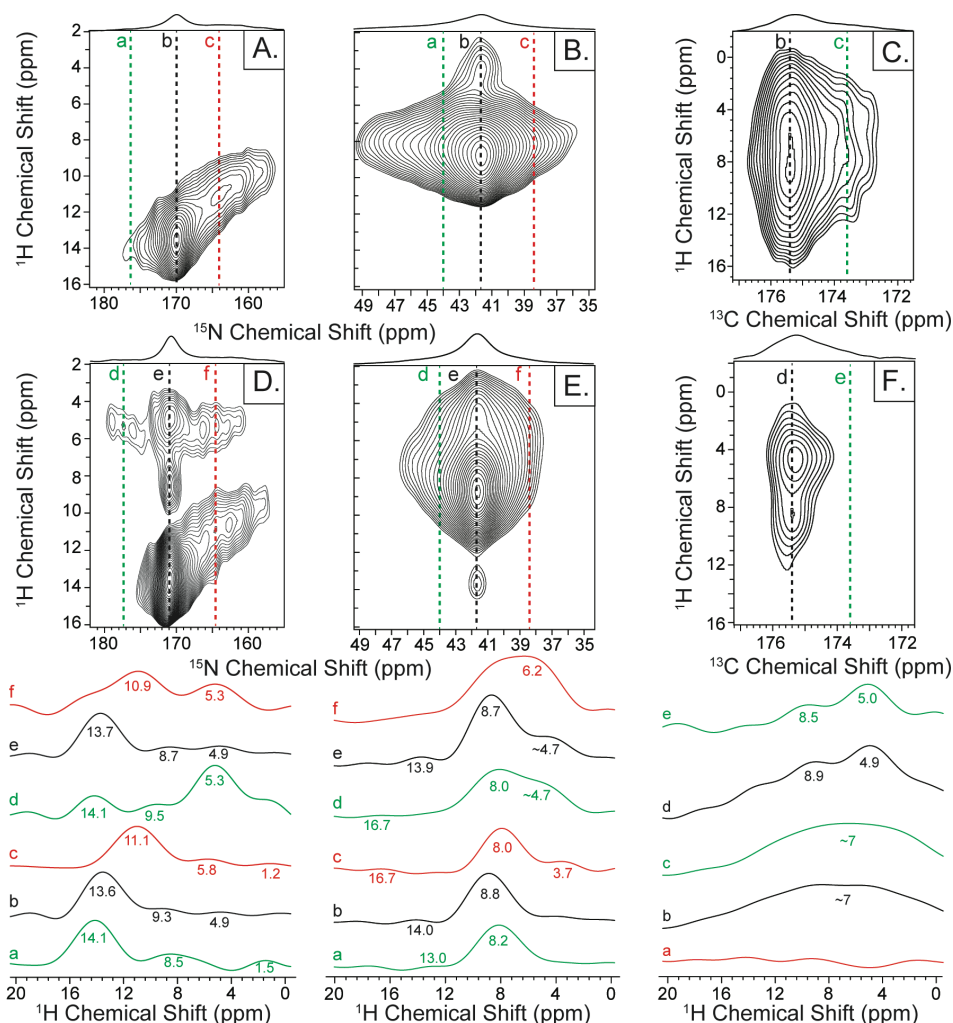


Figure 2.8. ^1H – ^{15}N and ^1H – ^{13}C HETCOR experiments of U-His/FSN-7.6 in (A-C) dried and (D-F) hydrated environments. Corresponding ^1H slices extracted from the ^{15}N or ^{13}C dimensions are shown at the bottom. Experiments were collected at 400 MHz with a 1.0 ms contact time, with 35 kHz MAS. Black lines represent excess His correlations, green and red represent adsorbed layer correlations that trend toward cationic or zwitterionic forms of His, respectively.

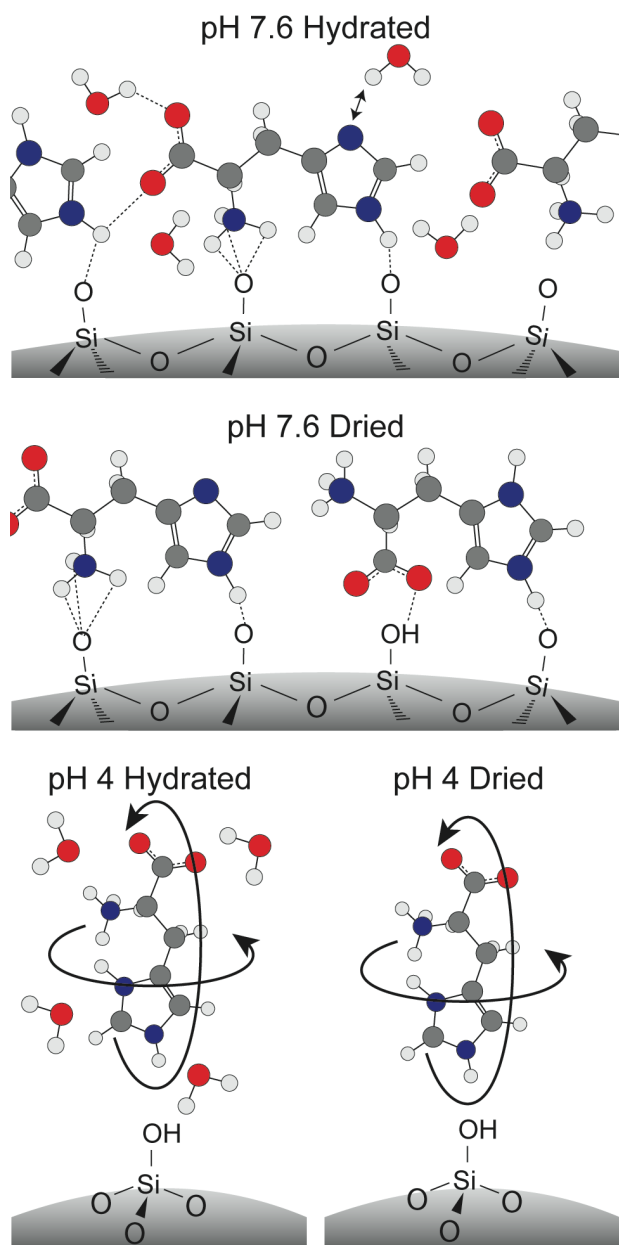


Figure 2.9. Proposed model of His – FSN interactions in hydrated and dried environments for pH 4 and 7.6 adsorptions on FSN surfaces. His has a rotational correlation time of ~ 5 ns in the hydrated state based on T₁.

Conclusions

The protonation state of His was determined for bulk U-HisHCl (protonated) and U-His (zwitterionic) by ^{13}C and ^{15}N CP-MAS SSNMR. A water layer exists at the interface of His/FSN adsorptions in a hydrated state, evidenced by TGA and SSNMR, that impacts His binding and dynamics. The U-His/FSN-4 hydrated adsorption layer exhibits isotropic behavior that was illustrated by fast ^{13}C T_1 relaxation (~ 0.5 s), $^1\text{J}_{\text{CH}}$ coupling resolution when decoupling is turned off, and strong ^{13}C DP signal under static conditions. In both hydrated and dried states of U-His/FSN-4, adsorbed resonances are close to the isotropic peaks of His at pH 4, suggesting all orientations are equally sampled at the interface with no binding preference and near liquid-like dynamics. In U-His/FSN-7.6 samples, electrostatic repulsion decreases and His interacts more strongly with the FSN surface. $\text{N}_{\epsilon 2}$, N_{α} , and C' adsorbed resonances are shifted from U-His due to interactions with FSN silanols. In the hydrated state of U-His/FSN-7.6, CP signal is stronger, line broadening occurs from chemical shift heterogeneity likely due to a distribution in hydrogen bond strengths, and T_1 values increase by 150% (~ 1.5 s). C' , N_{α} , $\text{N}_{\epsilon 2}$, and $\text{N}_{\delta 1}$ interact with water as shown by ^1H - ^{13}C and ^1H - ^{15}N HETCOR experiments. His molecules are arranged horizontally along the surface with $\text{N}_{\epsilon 2}$ and $\text{N}_{\alpha}/\text{C}'$ anchor points to the FSN surface at near neutral pH. Long range correlations between C' and neighboring $\text{H}_{\epsilon 2}$ are observed that orient $\text{N}_{\delta 1}$ away from the surface with strong water contacts observed for this site. In the dried state of U-His/FSN-7.6, the chemical shifts and line shapes of the adsorbed layer resemble amorphous His and $\text{N}_{\epsilon 2}$ experiences a large chemical shift upfield due to strong hydrogen bonding interactions with FSN. At both pH 4 and pH 7.6, the water layer influences dynamics but has little effect on binding geometry/molecular orientation for the near neutral sample while at pH 4 rapid dynamics are observed for both cases with no evidence of preferential binding. This work demonstrates the

power of advanced MAS SSNMR techniques for elucidating amino acid binding on surfaces at an atomic level allowing for molecular models to be proposed as illustrated here. It also highlights the importance of hydration state and adsorption solution pH when conducting such investigations and shows the diversity in amino acid binding arrangements possible on silica surfaces when this work is compared to other amino acids on FSN investigated with similar SSNMR techniques. This sets the stage for future multinuclear, multidimensional SSNMR studies of His-containing peptides on silica and other nanoparticle surfaces.

Acknowledgments

Haley L. Swanson would like to acknowledge support from NASA Fellowship 80NSSC19K0064. NMR instrumentation support from the College of Sciences at SDSU is greatly acknowledged.

Chapter 2, in full, is a reprint of the material as it appears published by Royal Society of Chemistry in the journal of Physical Chemistry Chemical Physics 2020. The dissertation author Haley L. Swanson was the primary investigator and author of this paper. Supporting authors include Chengchen Guo, Michael Cao, J. Bennett Addison, and Gregory P. Holland.

Supplemental Information

Table 2.S1. Sample abbreviations and preparation methods.

Abbreviation	State	Sample	Preparation
FSN	Solid	Fumed silica nanoparticles (7 nm)	When used in adsorptions, heated to 500 °C overnight prior to use
U-HisHCl	Solid, crystalline	Histidine, fully labeled, fully protonated	Isotopically labeled U-[¹⁵ N, ¹³ C]-L-histidine monohydrochloride monohydrate (98%). No preparation, used as received
U-His	Solid, powder	Histidine, fully labeled, zwitterionic	U-HisHCl adjusted to pH 7.6 ± 0.2 using 1M NaOH
Amorphous His	Solid, amorphous	Histidine, fully labeled, zwitterionic	The amorphous state was achieved by entrapping U-HisHCl in a sucrose solution (33% w/w) followed by flash freezing in liquid nitrogen and lyophilization
Isotropic His	Liquid	Histidine, fully labeled in an aqueous state	U-HisHCl dissolved in a 90:10 mixture of H ₂ O:D ₂ O and adjusted to pH 4 or pH 7.6 ± 0.2 using 1M NaOH
L-histidine·HCl·H ₂ O	Solid, crystalline	Histidine, natural abundance, fully protonated	No preparation, used as received
pure L-histidine	Solid, powder	Histidine, natural abundance, zwitterionic	No preparation, used as received
U-His/FSN- <i>x</i>	Solid, adsorbed	Histidine, fully labeled, adsorbed on FSN, <i>x</i> represents pH of the adsorption solution	U-HisHCl dissolved in water at 0.05M and adjusted to pH <i>x</i> . FSN was added and the solution was stirred for 3 h, centrifuged, and dried under vacuum
HisHCl/FSN- <i>x</i> M	Solid, adsorbed	Histidine, natural abundance, adsorbed on FSN, <i>x</i> represents concentration of the adsorption solution	L-histidine·HCl·H ₂ O dissolved in water at a concentration of <i>x</i> M and adjusted to pH 7.6 ± 0.2 using 1M NaOH. FSN was added and the solution was stirred for 3 h, centrifuged, and dried under vacuum
His/FSN- <i>x</i> M	Solid, adsorbed	Histidine, natural abundance, adsorbed on FSN, <i>x</i> represents concentration of the adsorption solution	Pure L-histidine dissolved in water at a concentration of <i>x</i> M and adjusted to pH 7.6 ± 0.2 using 1M NaOH. FSN was added and the solution was stirred for 3 h, centrifuged, and dried under vacuum
	“Adsorbed” or “ads”		The adsorbed layer of histidine that is in contact with FSN surface
	“Excess” or “exc”		Excess deposits of bulk histidine that build in around the adsorbed layer once the surface is saturated
	“Hydrated”		Any adsorptions that were analyzed directly following preparation and contain water at the surface
	“Dry”		Any adsorptions with the water layer removed by drying in rotor under high vacuum for 4 weeks at room temperature

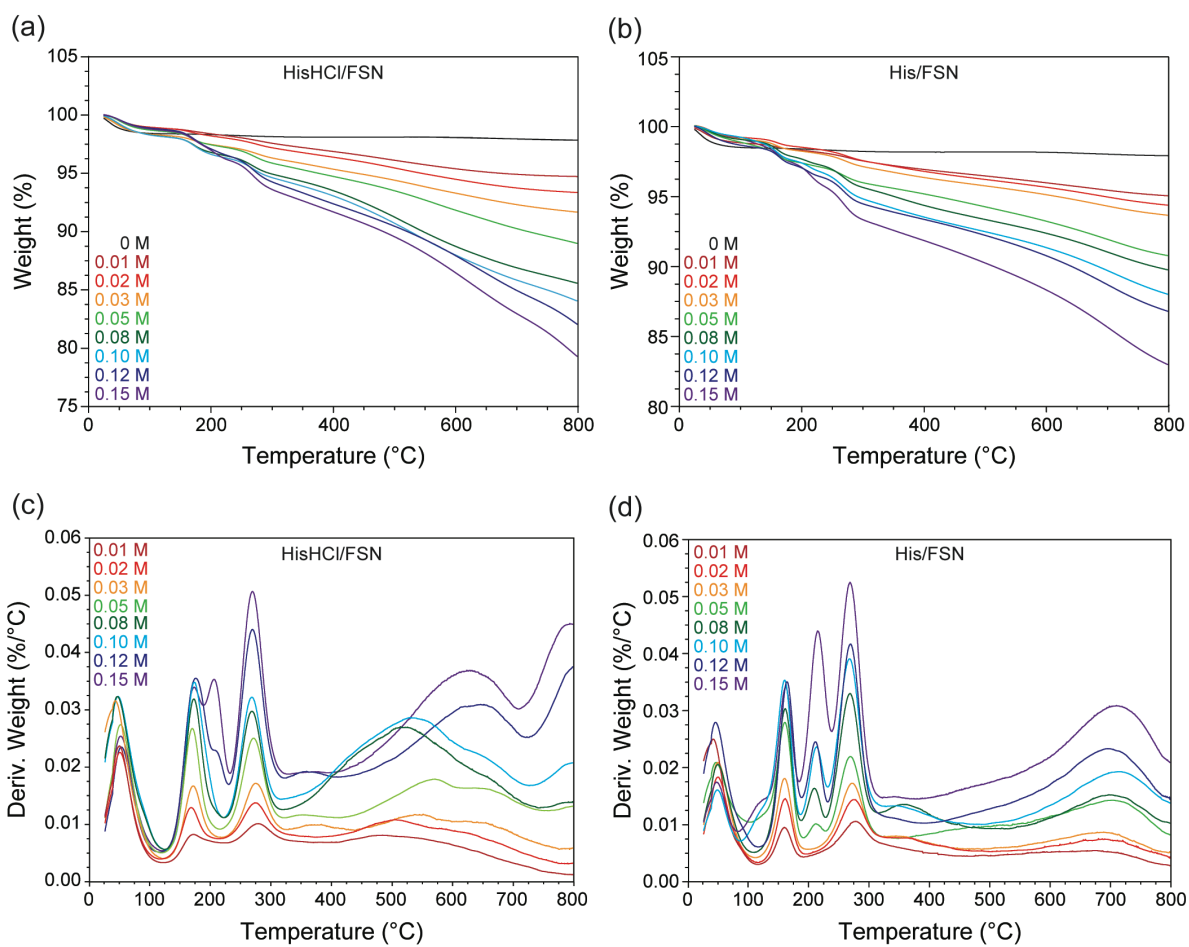


Figure 2.S1. (a, b) TGA curves and (c, d) DTG curves of His/FNS adsorptions using natural abundance L-histidine·HCl·H₂O (fully protonated crystal) or L-histidine (neutral powder). All adsorptions were adjusted to pH 7.6 ± 0.2.

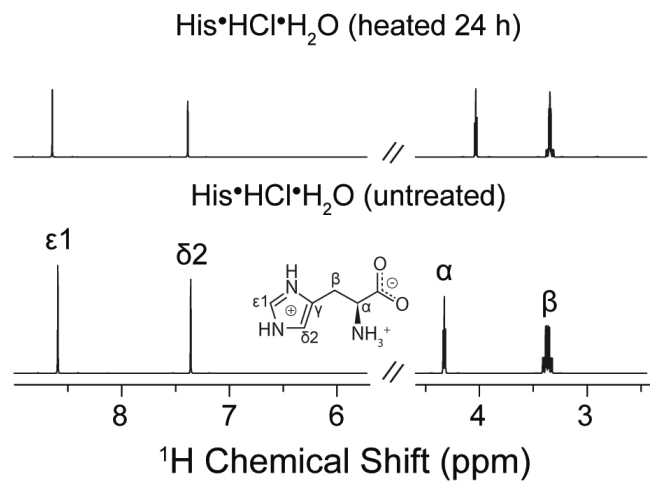


Figure 2.S2. ^1H Solution NMR of free HisHCl untreated (pH 1) and free HisHCl after thermal treatment of 24 h at 165 °C (pH 4). Both samples were dissolved in 90:10 H₂O:D₂O and referenced to DSS (0 ppm) as an internal standard. The small variation in chemical shifts between the two samples is only due to pH differences between samples and not indicative of a thermal condensation product.

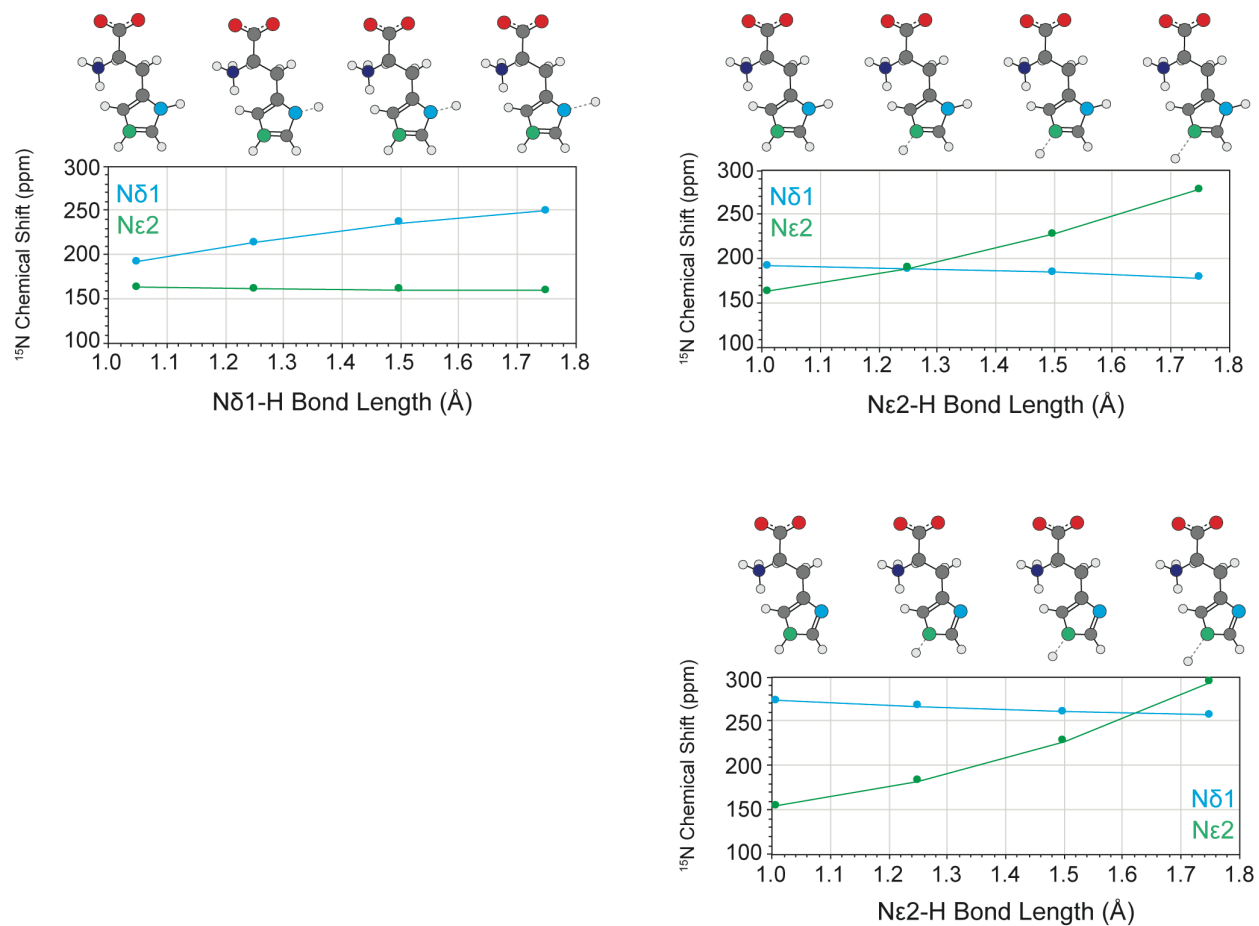


Figure 2.S3. DFT His models with N-H perturbations and resulting NMR chemical shift calculations. The calculated ^{15}N chemical shift (ppm) is plotted as a function of N-H bond length.

Table 2.S2. Computational results from DFT calculations of His models with N-H perturbations. A plus sign (+) represents protonated histidine with positively charged imidazole ring, and a zero (0) represents the neutral histidine molecule where N_{δ1} has been deprotonated.

		$\delta_{\text{calc}} \text{N}\delta 1$ (ppm)	$\delta_{\text{calc}} \text{N}\epsilon 2$ (ppm)	$\delta_{\text{calc}} \text{N}\alpha$ (ppm)
(+) N δ 1-H	1.05	191.8	163.2	39.1
	1.25	213.6	161.7	38.9
	1.50	235.9	160.4	38.5
	1.75	249.9	159.7	38.2
Avg Std Dev		223 \pm 26	161 \pm 2	39 \pm 0
(+) N ϵ 2-H	1.01	191.8	163.2	39.1
	1.25	188.7	189.7	39.3
	1.50	184.7	228.1	39.9
	1.75	179.2	278.4	41.9
Avg Std Dev		186 \pm 5	215 \pm 50	40 \pm 1
(0) N ϵ 2-H	1.01	272.6	154.8	44.1
	1.25	266.6	182.7	44.1
	1.50	260.2	227.2	44.1
	1.75	257.2	293.1	44.1
Avg Std Dev		264 \pm 7	214 \pm 60	44 \pm 0

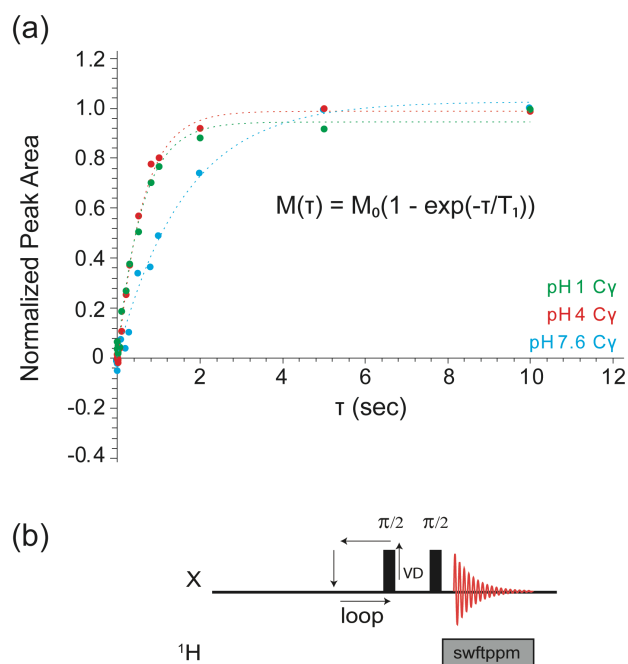


Figure 2.S4. ^{13}C Saturation recovery experiments used to selectively measure T_1 of the adsorbed layer by using a short recycle delay. (a) Data processing displayed for C_γ sites where integrated areas are plotted and fit to a single-component equation to determine T_1 . (b) The direct polarization pulse sequence of the saturation recovery experiment.

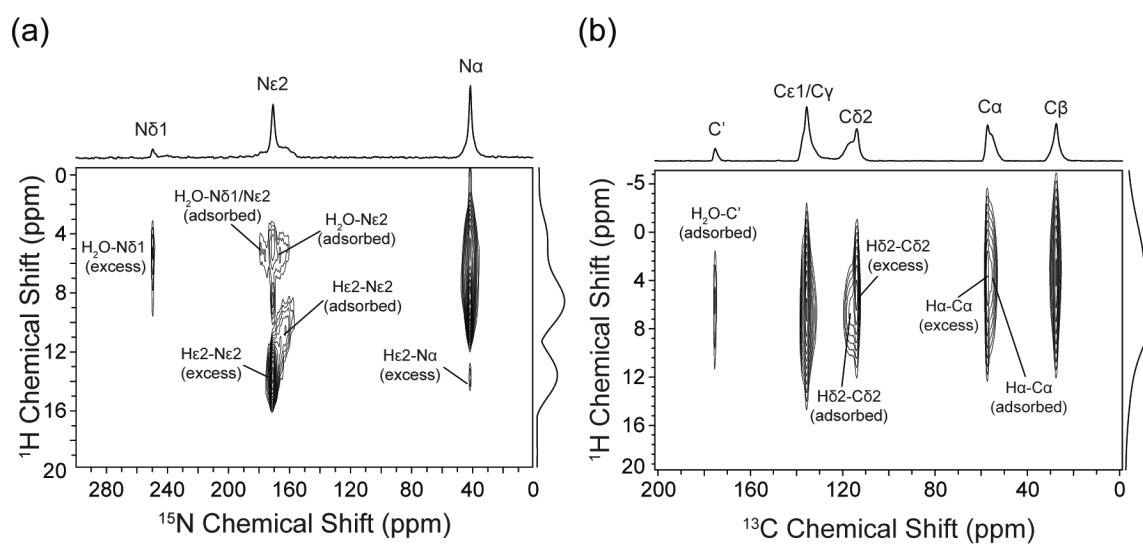


Figure 2.S5. Full spectrum (a) $^1\text{H} - ^{15}\text{N}$ and (b) $^1\text{H} - ^{13}\text{C}$ HETCOR of U-His/FSN-7.6 in the hydrated state. Experiments were collected at 400 MHz with 35 kHz MAS. Heteronuclear correlation is observed through polarization transfer with a 1 ms contact pulse.

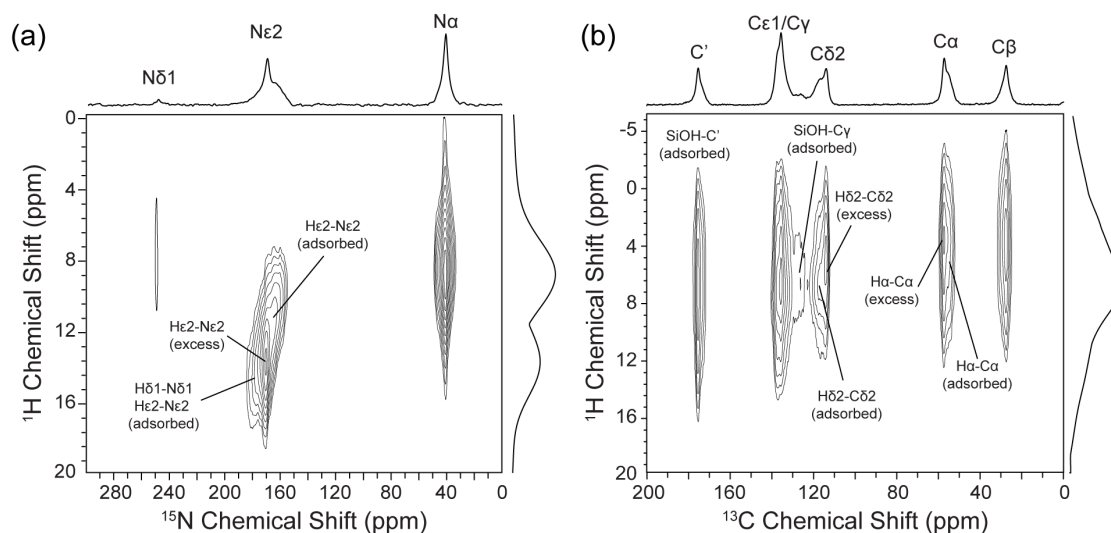


Figure 2.S6. Full spectrum (a) $^1\text{H} - ^{15}\text{N}$ and (b) $^1\text{H} - ^{13}\text{C}$ HETCOR of U-His/FSN-7.6 in the dried state. Samples were packed in rotor and dried under high vacuum for 3 weeks. ^1H 1D spectra were collected before and after analysis to make sure samples did not rehydrate during experimentation. Experiments were collected at 400 MHz with 35 kHz MAS. Heteronuclear correlation is observed through polarization transfer during a 1 ms contact pulse.

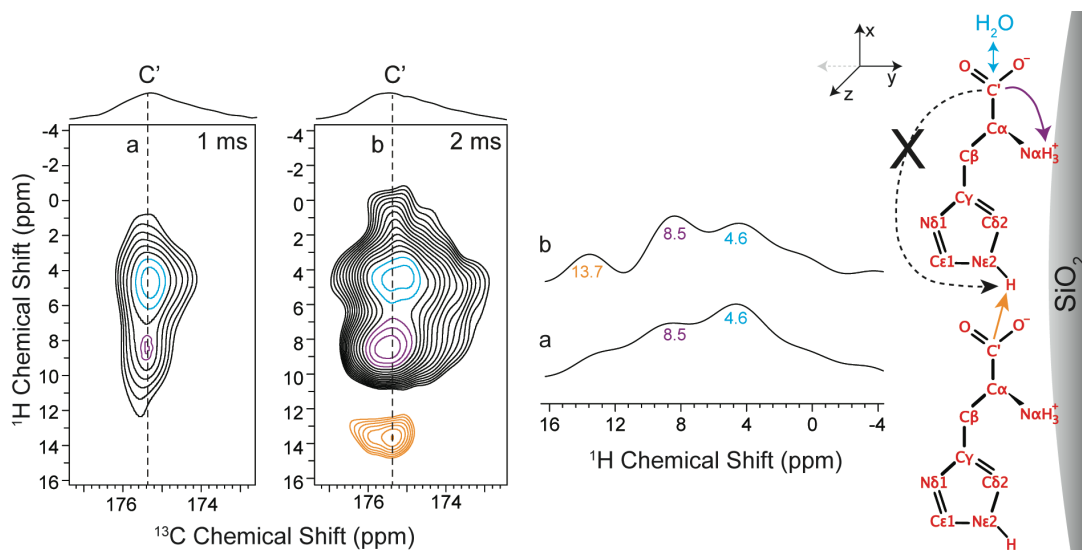


Figure 2.S7. $^1\text{H} - ^{13}\text{C}$ HETCOR of U-His/FSN-7.6 in the hydrated state with variable CP contact time to view long range couplings. Experiments were collected at 400 MHz with 35 kHz MAS. Heteronuclear correlation is observed through polarization transfer during a (a) 1 ms or (b) 2 ms contact pulse. Corresponding ^1H slices and intermolecular interactions are illustrated on the right. This result highlights intermolecular contact between C' and $\text{N}_{\epsilon 2}$ and provides strong evidence for the horizontal arrangement of His on the FSN surface.

References

1. Cox, A.; Andreozzi, P.; Dal Magro, R.; Fiordaliso, F.; Corbelli, A.; Talamini, L.; Chinello, C.; Raimondo, F.; Magni, F.; Tringali, M.; Krol, S.; Jacob Silva, P.; Stellacci, F.; Masserini, M.; Re, F., Evolution of Nanoparticle Protein Corona across the Blood-Brain Barrier. *ACS Nano* **2018**, *12* (7), 7292-7300.
2. Tchoryk, A.; Taresco, V.; Argent, R. H.; Ashford, M.; Gellert, P. R.; Stolnik, S.; Grabowska, A.; Garnett, M. C., Penetration and Uptake of Nanoparticles in 3D Tumor Spheroids. *Bioconjug Chem* **2019**
3. Tang, F.; Li, L.; Chen, D., Mesoporous silica nanoparticles: synthesis, biocompatibility and drug delivery. *Adv Mater* **2012**, *24* (12), 1504-34.
4. Slowing, I. I.; Vivero-Escoto, J. L.; Wu, C.-W.; Lin, V. S. Y., Mesoporous silica nanoparticles as controlled release drug delivery and gene transfection carriers. *Adv Drug Deliv Rev* **2008**, *60* (11), 1278-1288.
5. Weiss, A. C. G.; Kruger, K.; Besford, Q. A.; Schlenk, M.; Kempe, K.; Forster, S.; Caruso, F., In Situ Characterization of Protein Corona Formation on Silica Microparticles Using Confocal Laser Scanning Microscopy Combined with Microfluidics. *ACS Appl Mater Interfaces* **2019**, *11* (2), 2459-2469.
6. Sun, T.; Zhang, Y. S.; Pang, B.; Hyun, D. C.; Yang, M.; Xia, Y., Engineered Nanoparticles for Drug Delivery in Cancer Therapy. *Angew Chem Int Ed* **2014**, *53* (46), 12320-64.
7. Jain, A.; Singh, S. K.; Arya, S. K.; Kundu, S. C.; Kapoor, S., Protein Nanoparticles: Promising Platforms for Drug Delivery Applications. *ACS Biomater Sci Eng* **2018**, *4* (12), 3939-3961.
8. Tarn, D.; Ashley, C. E.; Xue, M.; Carnes, E. C.; Zink, J. I.; Brinker, C. J., Mesoporous silica nanoparticle nanocarriers: biofunctionality and biocompatibility. *Acc Chem Res* **2013**, *46* (3), 792-801.
9. Bilalis, P.; Tziveleka, L. A.; Varlas, S.; Iatrou, H., pH-Sensitive nanogates based on poly(L-histidine) for controlled drug release from mesoporous silica nanoparticles. *Polymer Chemistry* **2016**, *7* (7), 1475-1485.
10. Brigger, I.; Dubernet, C.; Couvreur, P., Nanoparticles in cancer therapy and diagnosis. *Adv Drug Deliv Rev* **2012**, *64*, 24-36.
11. Sztandera, K.; Gorzkiewicz, M.; Klajnert-Maculewicz, B., Gold Nanoparticles in Cancer Treatment. *Mol Pharmaceut* **2019**, *16* (1), 1-23.

12. Qian, R. C.; Lv, J.; Long, Y. T., Controllable Aggregation-Induced Exocytosis Inhibition (CAIEI) of Plasmonic Nanoparticles in Cancer Cells Regulated by MicroRNA. *Mol Pharmaceut* **2018**, *15* (9), 4031-4037.
13. Hu, C. M.; Aryal, S.; Zhang, L., Nanoparticle-assisted combination therapies for effective cancer treatment. *Ther Deliv* **2010**, *1* (2), 323-34.
14. Chen, W.; Glackin, C. A.; Horwitz, M. A.; Zink, J. I., Nanomachines and Other Caps on Mesoporous Silica Nanoparticles for Drug Delivery. *Acc Chem Res* **2019**, *52* (6), 1531-1542.
15. Guntner, A. T.; Sievi, N. A.; Theodore, S. J.; Gulich, T.; Kohler, M.; Pratsinis, S. E., Noninvasive Body Fat Burn Monitoring from Exhaled Acetone with Si-doped WO₃-sensing Nanoparticles. *Anal Chem* **2017**, *89* (19), 10578-10584.
16. Drobny, G. P.; Long, J. R.; Karlsson, T.; Shaw, W.; Popham, J.; Oyler, N.; Bower, P.; Stringer, J.; Gregory, D.; Mehta, M.; Stayton, P. S., Structural Studies of Biomaterials Using Double-Quantum Solid-State NMR Spectroscopy. *Annu Rev Phys Chem* **2003**, *54* (1), 531-571.
17. Baio, J. E.; Zane, A.; Jaeger, V.; Roehrich, A. M.; Lutz, H.; Pfaendtner, J.; Drobny, G. P.; Weidner, T., Diatom mimics: directing the formation of biosilica nanoparticles by controlled folding of lysine-leucine peptides. *J Am Chem Soc* **2014**, *136* (43), 15134-7.
18. Bertani, P.; Raya, J.; Bechinger, B., ¹⁵N chemical shift referencing in solid state NMR. *Solid State Nucl Mag* **2014**, 61-62, 15-8.
19. Buckle, E. L.; Prakash, A.; Bonomi, M.; Sampath, J.; Pfaendtner, J.; Drobny, G. P., Solid-State NMR and MD Study of the Structure of the Statherin Mutant SNa15 on Mineral Surfaces. *J Am Chem Soc* **2019**, *141* (5), 1998-2011.
20. Buckle, E. L.; Roehrich, A.; Vandermoon, B.; Drobny, G. P., Comparative Study of Secondary Structure and Interactions of the R5 Peptide in Silicon Oxide and Titanium Oxide Coprecipitates Using Solid-State NMR Spectroscopy. *Langmuir* **2017**, *33* (40), 10517-10524.
21. Ndao, M.; Goobes, G.; Emani, P. S.; Drobny, G. P., A REDOR ssNMR Investigation of the Role of an N-Terminus Lysine in R5 Silica Recognition. *Langmuir* **2018**, *34* (29), 8678-8684.
22. Lundqvist, M.; Sethson, I.; Jonsson, B.-H., Protein Adsorption onto Silica Nanoparticles: Conformational Changes Depend on the Particles' Curvature and the Protein Stability. *Langmuir* **2004**, *20* (24), 10639-10647.
23. Shaw, C. P.; Middleton, D. A.; Volk, M.; Lévy, R., Amyloid-Derived Peptide Forms Self-Assembled Monolayers on Gold Nanoparticle with a Curvature-Dependent β -Sheet Structure. *ACS Nano* **2012**, *6* (2), 1416-1426.

24. Stöber, W.; Fink, A.; Bohn, E., Controlled growth of monodisperse silica spheres in the micron size range. *J Colloid Interface Sci* **1968**, *26*, 62-69.
25. Bogush, G. H.; Tracy, M. A.; Zukoski IV, C. F., Preparation of Monodisperse Silica Particles: Control of Size and Mass Fraction. *J Non Cryst Solids* **1988**, *104*, 95-106.
26. Sato-Berrú, R.; Saniger, J. M.; Flores-Flores, J.; Sanchez-Espíndola, M., Simple Method for the Controlled Growth of SiO₂ Spheres. *Mater Sci Eng A* **2013**, *3* (4), 237-242.
27. Zhang, H.; Dunphy, D. R.; Jiang, X.; Meng, H.; Sun, B.; Tarn, D.; Xue, M.; Wang, X.; Lin, S.; Ji, Z.; Li, R.; Garcia, F. L.; Yang, J.; Kirk, M. L.; Xia, T.; Zink, J. I.; Nel, A.; Brinker, C. J., Processing pathway dependence of amorphous silica nanoparticle toxicity: colloidal vs pyrolytic. *J Am Chem Soc* **2012**, *134* (38), 15790-804.
28. Nandiyanto, A. B. D.; Kim, S. G.; Iskandar, F.; Okuyama, K., Synthesis of spherical mesoporous silica nanoparticles with nanometer-size controllable pores and outer diameters. *Micropor Mesopor Mat* **2009**, *120* (3), 447-453.
29. Kresge, C. T.; Leonowicz, M. E.; Roth, W. J.; Vartuli, J. C.; Beck, J. S., Ordered mesoporous molecular sieves synthesized by a liquid-crystal template mechanism. *Nature* **1992**, *359* (6397), 710-712.
30. Vartuli, J. C.; Schmitt, K. D.; Kresge, C. T.; Roth, W. J.; Leonowicz, M. E.; McCullen, S. B.; Hellring, S. D.; Beck, J. S.; Schlenker, J. L., Effect of Surfactant/Silica Molar Ratios on the Formation of Mesoporous Molecular Sieves: Inorganic Mimicry of Surfactant Liquid-Crystal Phases and Mechanistic Implications. *Chem Mater* **1994**, *6* (12), 2317-2326.
31. Aw, M. S.; Simovic, S.; Addai-Mensah, J.; Losic, D., Silica microcapsules from diatoms as new carrier for delivery of therapeutics. *Nanomedicine* **2011**, *6* (7), 1159-73.
32. Argyo, C.; Weiss, V.; Bräuchle, C.; Bein, T., Multifunctional Mesoporous Silica Nanoparticles as a Universal Platform for Drug Delivery. *Chem Mater* **2014**, *26* (1), 435-451.
33. Urata, C.; Aoyama, Y.; Tonegawa, A.; Yamauchi, Y.; Kuroda, K., Dialysis process for the removal of surfactants to form colloidal mesoporous silica nanoparticles. *Chem Commun* **2009**, (34), 5094-6.
34. Paris, J. L.; Vallet-Regi, M., Mesoporous Silica Nanoparticles for Co-Delivery of Drugs and Nucleic Acids in Oncology: A Review. *Pharmaceutics* **2020**, *12* (6).
35. Thomas, C. R.; Ferris, D. P.; Lee, J.-H.; Choi, E.; Cho, M. H.; Kim, E. S.; Stoddart, J. F.; Shin, J.-S.; Cheon, J.; Zink, J. I., Noninvasive Remote-Controlled Release of Drug Molecules in Vitro Using Magnetic Actuation of Mechanized Nanoparticles. *J Am Chem Soc* **2010**, *132* (31), 10623-10625.

36. Barnes, M. R.; Gray, I. C., *Bioinformatics for geneticists*. Wiley,; Chichester, England ; Hoboken, NJ, 2003; pp. xiv, 408 pages, 8 pages of plates. Table of contents <http://catdir.loc.gov/catdir/toc/wiley032/2003535288.html>
Contributor biographical information
<http://catdir.loc.gov/catdir/enhancements/fy0708/2003535288-b.html>
Publisher description <http://catdir.loc.gov/catdir/description/wiley036/2003535288.html>
http://nrs.harvard.edu/urn-3:hul.ebook:MBC_0470843934.
37. Sun, B.; Pokhrel, S.; Dunphy, D. R.; Zhang, H.; Ji, Z.; Wang, X.; Wang, M.; Liao, Y. P.; Chang, C. H.; Dong, J.; Li, R.; Madler, L.; Brinker, C. J.; Nel, A. E.; Xia, T., Reduction of Acute Inflammatory Effects of Fumed Silica Nanoparticles in the Lung by Adjusting Silanol Display through Calcination and Metal Doping. *ACS Nano* **2015**, *9* (9), 9357-72.
38. Guo, C.; Jordan, J. S.; Yarger, J. L.; Holland, G. P., Highly Efficient Fumed Silica Nanoparticles for Peptide Bond Formation: Converting Alanine to Alanine Anhydride. *ACS Appl Mater Interfaces* **2017**, *9* (20), 17653-17661.
39. Osterberg, T.; Wadsten, T., Physical state of L-histidine after freeze-drying and long-term storage. *Eur J Pharm Sci* **1999**, *8* (4), 301-8.
40. Stephens, P. J.; Devlin, F. J.; Chabalowski, C. F.; Frisch, M. J., Ab Initio Calculation of Vibrational Absorption and Circular Dichroism Spectra Using Density Functional Force Fields. *J Phys Chem* **1994**, *98* (45), 11623-11627.
41. Wolinski, K.; Hinton, J. F.; Pulay, P., Efficient implementation of the gauge-independent atomic orbital method for NMR chemical shift calculations. *J Am Chem Soc* **1990**, *112* (23), 8251-8260.
42. Gervais, C.; Dupree, R.; Pike, K. J.; Bonhomme, C.; Profeta, M.; Pickard, C. J.; Mauri, F., Combined first-principles computational and experimental multinuclear solid-state NMR investigation of amino acids. *J Phys Chem A* **2005**, *109* (31), 6960-9.
43. Gervais, C.; Profeta, M.; Lafond, V.; Bonhomme, C.; Azais, T.; Mutin, H.; Pickard, C. J.; Mauri, F.; Babonneau, F., Combined ab initio computational and experimental multinuclear solid-state magnetic resonance study of phenylphosphonic acid. *Magn Reson Chem* **2004**, *42* (5), 445-52.
44. Sceats, E. L.; Figueroa, J. S.; Cummins, C. C.; Loening, N. M.; Van der Wel, P.; Griffin, R. G., Complexes obtained by electrophilic attack on a dinitrogen-derived terminal molybdenum nitride: electronic structure analysis by solid state CP/MAS ¹⁵N NMR in combination with DFT calculations. *Polyhedron* **2004**, *23* (17), 2751-2768.
45. Thakur, R. S.; Kurur, N. D.; Madhu, P. K., An analysis of phase-modulated heteronuclear dipolar decoupling sequences in solid-state nuclear magnetic resonance. *J Magn Reson* **2008**, *193* (1), 77-88.

46. Torchia, D. A., The measurement of proton-enhanced carbon-13 T1 values by a method which suppresses artifacts. *J Magn Reson* **1978**, *30* (3), 613-616.
47. Hayashi, S.; Hayamizu, K., Chemical Shift Standards in High-Resolution Solid-State NMR (2) ¹⁵N Nuclei. *Bull Chem Soc Jpn* **1991**, *64* (2), 688-690.
48. Morcombe, C. R.; Zilm, K. W., Chemical shift referencing in MAS solid state NMR. *J Magn Reson* **2003**, *162* (2), 479-86.
49. Guo, C.; Holland, G. P., Investigating Lysine Adsorption on Fumed Silica Nanoparticles. *J Phys Chem C* **2014**, *118* (44), 25792-25801.
50. Guo, C.; Holland, G. P., Alanine Adsorption and Thermal Condensation at the Interface of Fumed Silica Nanoparticles: A Solid-State NMR Investigation. *J Phys Chem C* **2015**, *119* (45), 25663-25672.
51. Lambert, J. F.; Jaber, M.; Georgelin, T.; Stievano, L., A comparative study of the catalysis of peptide bond formation by oxide surfaces. *Phys Chem Chem Phys* **2013**, *15* (32), 13371-80.
52. Stievano, L.; Piao, L. Y.; Lopes, I.; Meng, M.; Costa, D.; Lambert, J. F., Glycine and lysine adsorption and reactivity on the surface of amorphous silica. *Eur J Mineralogy* **2007**, *19* (3), 321-331.
53. Bouchoucha, M.; Jaber, M.; Onfroy, T.; Lambert, J.-F.; Xue, B., Glutamic Acid Adsorption and Transformations on Silica. *J Phys Chem C* **2011**, *115* (44), 21813-21825.
54. Lambert, J.-F.; Stievano, L.; Lopes, I.; Gharsallah, M.; Piao, L., The fate of amino acids adsorbed on mineral matter. *Planet Space Sci* **2009**, *57* (4), 460-467.
55. Anandan, P.; Jayavel, R., Crystal growth and characterization of semiorganic single crystals of l-histidine family for NLO applications. *J Cryst Growth* **2011**, *322* (1), 69-73.
56. Bujdak, J.; Eder, A.; Yongyai, Y.; Faybikova, K.; Rode, B. M., Investigation on the mechanism of peptide chain prolongation on montmorillonite. *J Inorg Biochem* **1996**, *61* (1), 69-78.
57. Fuchida, S.; Masuda, H.; Shinoda, K., Peptide formation mechanism on montmorillonite under thermal conditions. *Orig Life Evol Biosph* **2014**, *44* (1), 13-28.
58. Bujdak, J.; Rode, B. M., The Effect of Smectite Composition on the Catalysis of Peptide Bond Formation. *J Mol Evol* **1996**, *43* (4), 326-33.
59. Li, S.; Hong, M., Protonation, Tautomerization, and Rotameric Structure of Histidine: A Comprehensive Study by Magic-Angle-Spinning Solid-State NMR. *J Am Chem Soc* **2011**, *133* (5), 1534-44.

60. Mathe, C.; Devineau, S.; Aude, J. C.; Lagniel, G.; Chedin, S.; Legros, V.; Mathon, M. H.; Renault, J. P.; Pin, S.; Boulard, Y.; Labarre, J., Structural determinants for protein adsorption/non-adsorption to silica surface. *PLoS One* **2013**, *8* (11), e81346.
61. Bloembergen, N.; Purcell, E. M.; Pound, R. V., Relaxation Effects in Nuclear Magnetic Resonance Absorption. *Phys Rev* **1948**, *73* (7), 679-712.
62. Iwahara, J.; Jung, Y. S.; Clore, G. M., Heteronuclear NMR spectroscopy for lysine NH3 groups in proteins: unique effect of water exchange on (15)N transverse relaxation. *J Am Chem Soc* **2007**, *129* (10), 2971-80.
63. Mudunkotuwa, I. A.; Grassian, V. H., Histidine adsorption on TiO₂ nanoparticles: an integrated spectroscopic, thermodynamic, and molecular-based approach toward understanding nano-bio interactions. *Langmuir* **2014**, *30* (29), 8751-60.
64. Heyda, J.; Mason, P. E.; Jungwirth, P., Attractive Interactions between Side Chains of Histidine-Histidine and Histidine-Arginine-Based Cationic Dipeptides in Water. *J Phys Chem B* **2010**, *114*, 8744-8749.
65. Ben Shir, I.; Kababya, S.; Schmidt, A., Molecular Details of Amorphous Silica Surfaces Determine Binding Specificity to Small Amino Acids. *J Phys Chem C* **2014**, *118* (15), 7901-7909.
66. Meng, M.; Stievano, L.; Lambert, J. F., Adsorption and Thermal Condensation Mechanisms of Amino Acids on Oxide Supports. 1. Glycine on Silica. *Langmuir* **2004**, *20*, 914-923.

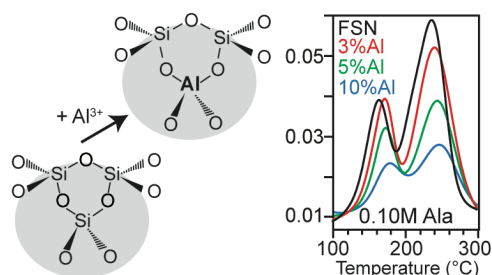
Chapter 3

The impact of metal doping on fumed silica structure and amino acid thermal condensation catalytic properties

Abstract

Fumed silica nanoparticles (FSN) are one of the most commonly synthesized forms of silica but prolonged exposure leads to cell toxicity and apoptosis due to reactive oxygen species (ROS) generation and cell membrane perturbation resulting from hydrogen-bonding and electrostatic interactions. Increasing attention is being put on synthesizing FSN material that is safer both for workers involved in large-scale industrial production, and consumers coming into contact with FSN additives. In the present work, we explore the structural differences and efficacy of Al- and Ti-metal doped FSN which has previously been shown to reduce toxicity effects of FSN. We use a combination of ^{29}Si and ^{27}Al solid-state magic angle spinning (MAS) NMR, Raman spectroscopy, and thermogravimetric analysis (TGA) to probe the surface and bulk structure and quantify the adsorption capacity and reactivity of the metal-doped FSN with respect to amino acid thermal condensation. Alanine was selected as the amino acid of choice for its simplicity and ubiquity in biochemical reactions. The results indicate that metal doping has a modest impact on the fumed silica molecular structure with a small decrease in amino acid adsorption capacity and thermal condensation reactivity as a function of increased metal doping.

Graphical Abstract



Introduction

Fumed silica nanoparticles (FSN) are generally recognized as safe (GRAS) by the Food and Drug Administration (FDA) and have been a commonly used additive in foods, beverages, and cosmetics for decades.¹ While oral consumption of FSN is GRAS, repeated exposure leads to accumulation in cells, causing inflammation, apoptosis, and cytotoxicity.²⁻⁴ Recent studies show that inhalation causes immediate acute inflammatory responses in the pulmonary system.⁴ Prolonged exposure induces chronic lung toxicity and its effects on other organs have yet to be studied.⁴ This brings the GRAS classification into question. FSN is one of the most highly produced synthetic forms of silica due to its stability and widespread applicability;⁵ thus, efforts to make the material safer are of significant public interest. Brinker et al have begun investigating metal doping of FSN as a novel alternative that shows promising results in the context of reducing cellular toxicity. Aluminum and titanium are introduced during the pyrolytic synthesis and the resulting metal-doped FSN exhibits reduced reactive oxygen species (ROS) generation and inflammatory responses in the lung compared to undoped FSN.^{3, 4} Here, we present the first investigation into the molecular structural changes due to metal doping and the impact of metal doping on FSN amino acid thermal condensation catalytic activity.

One of the reasons why FSN is such an efficient thickening agent is because of its extremely high surface area with primary particle sizes in the range of 7 – 14 nm. Due to the nature of FSN formation, these types of particles contain an increased population of strained 3-membered rings (3MR) that have been shown to cleave after thermal treatment and rehydration to form surface radical species.^{2, 3} It has been hypothesized that these inherent strained ring defects and surface radicals are what makes FSN highly reactive and toxic to cells.^{2, 6} The high surface area combined with ROS generation also makes FSN a very effective catalyst in the promotion of

thermal condensation reactions which have significant implications in origin of life research.⁷⁻¹³ Much of the Earth's crust is composed of silicates, silica-containing clays, and silica substrates have been shown to sequester and stabilize amino acids in dilute solutions and promote oligomerization.^{9, 14-16} Clays and other silica-based minerals often exist in combination with other elements, so understanding how metals such as Al and Ti effect both binding and oligomerization is also of interest in origin of life research. Oligomerization proceeds through condensation of neighboring amino acids and is readily monitored by first derivative thermogravimetric analysis (DTG).^{14, 17-20} This presents a simple and effective method to monitor changes in surface reactivity as a function of amino acid loading capacity. Here, solid-state nuclear magnetic resonance (SSNMR) and Raman spectroscopy are used to characterize the molecular structure of metal-doped FSN, and thermogravimetric analysis (TGA) is used to determine the influence of metal doping on FSN amino acid adsorption capacity and thermal condensation reactivity. The results of these experiments illustrate that metal doping influences the FSN molecular structure and decreases the amino acid adsorption capacity and thermal condensation reactivity as the metal content is increased at low levels.

Experimental

Materials

Natural abundance L-alanine was purchased from Sigma-Aldrich and used as received.

Preparation of Metal-Doped FSN

Flame spray pyrolysis was used to synthesize metal-doped silica nanoparticles. Details of the procedure are described elsewhere.^{21, 22} In brief, the undoped, Ti- and Al-doped SiO₂ were

obtained using a flame aerosol technique. The Ti-doped SiO₂ library was synthesized via combustion of titanium isopropoxide (Ti-precursor, Sigma Adrich) mixed with tetraethylorthosilicate (TEOS, Si-precursor, Sigma Adrich). Al-doped SiO₂ was obtained by combustion of the mixture of aluminum secondary butoxide (Al-precursor, Sigma Adrich) and tetraethylorthosilicate. For both the cases, the resulting solutions were diluted with xylene. To prepare 10% Ti or Al doped SiO₂ particles (as an example), 15.2 mL of 0.1 M titanium isopropoxide or 27.4 mL of 0.1 M aluminum secondary butoxide were mixed together with 50 mL of 0.5 M TEOS and flame sprayed. During combustion (1) liquid spray was ignited by premixed gases such as CH₄ and O₂ flowing at the rate of 1.5 and 3.2 L/min, respectively, forming a spray flame (2) the precursor feed was maintained at 5 mL/min throughout the experiment (3) the precursor droplets were atomized using 5 L/min O₂ at a constant pressure drop of 1.5 bar at the nozzle. The ultrafine particles produced were collected from a 257 mm glass filter placed in the flame reactor at the distance of 60 cm from the flame nozzle.

Adsorption of Alanine on FSN

FSN was heated at 500 °C in an oven overnight to remove adsorbed water and impurities from the surface and activate the FSN. Aqueous solutions of alanine were produced [0.10 M] using deionized water and separated into 5.00 mL aliquots. 75 mg of FSN was added and each solution was stirred overnight at ambient conditions followed by centrifugation at 6000 rpm for 1 h to pellet the adsorption complex. Samples were dried under vacuum overnight at room temperature and analyzed as described below.

Solid-state Nuclear Magnetic Resonance Spectroscopy

NMR experiments were conducted with a 600 MHz Bruker Avance IIIHD spectrometer equipped with a 4 mm double resonance ($^1\text{H}/\text{X}$) MAS probe. ^{27}Al direct polarization (DP)-MAS experiments were collected with 15 kHz MAS using a $0.66\ \mu\text{s}$ ($\pi/12$) excitation pulse, 1600 ppm spectral width (sw), 4k points, 0.25 sec recycle delay (d1), and 16k – 256k scans, with no decoupling. ^{27}Al CP-MAS experiments were set up using an aluminum oxide standard (γ -alumina) at 15 kHz MAS. Experiments were collected with an 800 ppm sw, 512 points, 1 sec d1, 16k scans, and no decoupling. An initial ^1H $\pi/2$ pulse of $4.5\ \mu\text{s}$ was applied, followed by a $500\ \mu\text{s}$ contact pulse (30% ramp) matched to the -1 Hartman Hahn spinning side band condition for ^{27}Al at 35 kHz B_1 field strength (RF). ^{27}Al spectra were processed with 2k points, 100 Hz line broadening and externally referenced to a 1 M solution of $\text{Al}(\text{NO}_3)_3$ (0 ppm).

^{29}Si DP-MAS experiments were collected at 5 kHz MAS using a $4\ \mu\text{s}$ ($\pi/2$) excitation pulse, 382 ppm sweep width (sw), 512 points, 300 sec recycle delay (d1), and 280 scans. High-powered spinal-64 ^1H decoupling was applied at 44 – 46 kHz RF during acquisition, and spectra were processed with 4k points and 50 Hz line broadening. $^1\text{H} \rightarrow ^{29}\text{Si}$ cross-polarization (CP) experiments included an initial ^1H $\pi/2$ pulse of 2.7-2.75 μs followed by a ramped (50%) 5 ms contact pulse matched to the -1 Hartman Hahn spinning sideband condition for ^{29}Si at 55 kHz RF. High-powered spinal-64 ^1H decoupling at 44 – 46 kHz RF was applied during acquisition. ^{29}Si CP-MAS experiments were collected with a 382 ppm sw, 512 points, 5 s d1, and 8k scans. 20 Hz line broadening and zero-filling to 2k points were used in processing. All ^{29}Si NMR spectra were externally referenced to TTSS (-9.7 ppm).

BET and OH-concentration Determination

The Brunauer-Emmett-Teller (BET) measurements were performed using a Quantachrome NOVA gas adsorption system at liquid N₂ temperature to determine the specific surface areas of the samples. The powders (~ 60-100 mg) placed in a test cell were allowed to degas at 200 °C for 2 hours. Data were acquired by exposing or removing a known quantity of gas in or out of the cell containing the solid adsorbent maintained at 77 K. Total OH-concentrations were obtained via integration of near and mid IR bands centered at 4500 and 3750 cm⁻¹, followed by applying Beers law with molar absorptivity coefficients of 0.16 and 4 μM/cm⁻¹, respectively.^{2, 23}

Raman Spectroscopy

The Raman spectroscopic data was collected using a custom-built Raman spectrometer configured in 180° geometry. The sample was excited using a 150 mW Coherent Sapphire SF laser with a 532 nm laser wavelength. The laser power was controlled using a neutral density filter wheel and an initial laser power of 28 mW. The laser was focused onto the sample using a 50X super long working distance plan APO Mitutoyo objective with a numerical aperture of 0.42. The signal was discriminated from the laser excitation using an Ondax® SureBlock™ ultranarrow-band notch filter combined with two Optigrate notch filters. The data were collected using an Acton 300i spectrograph and a back thinned Princeton Instruments liquid nitrogen cooled CCD detector.

Thermogravimetric Analysis

A TA2910 (TA Instruments Inc.) TGA was used to quantify adsorption and assess surface reactivity of the metal doped FSN. A sample mass of 12 – 15 mg was used in each experiment and the sample was equilibrated under N₂ flow for a minimum of 30 min prior to analysis or until a

stable baseline was reached. The instrument flow rate was maintained at 60 mL/min and 40 mL/min for furnace and balance, respectively. The TGA method included temperature equilibration at 25 °C followed by a 5 °C/min heating rate applied from 25 – 600 °C.

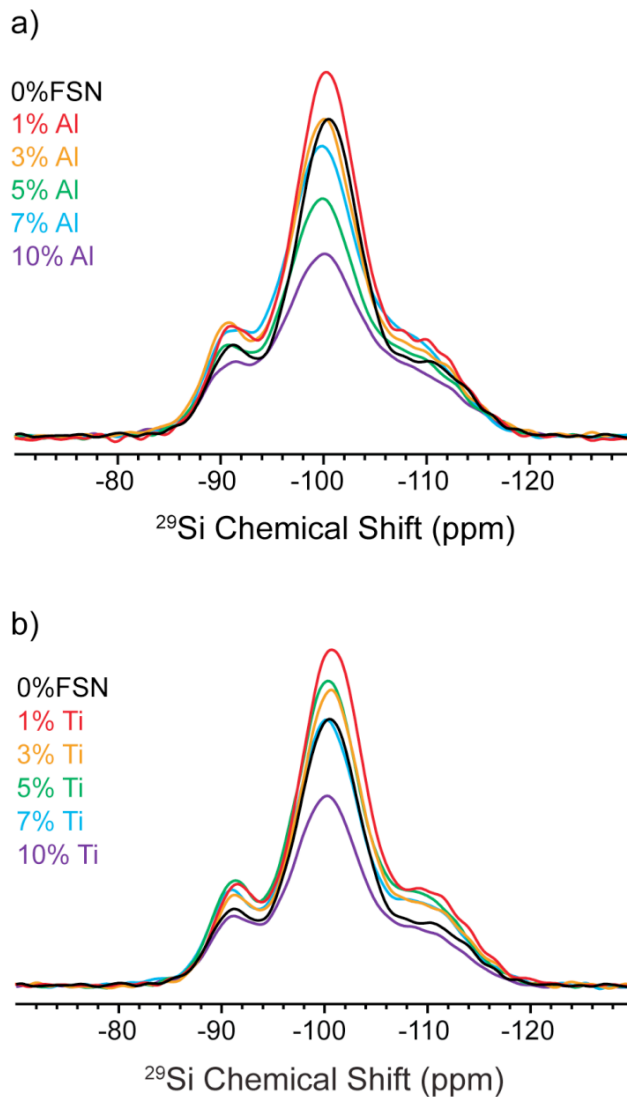


Figure 3.1. ^{29}Si CP-MAS NMR of a) Al- and b) Ti-doped samples with 0%FSN. Spectra are scaled proportionally to sample mass.

Results

^{29}Si CP-MAS

$^1\text{H} \rightarrow ^{29}\text{Si}$ CP-MAS experiments were used to selectively characterize the surface of FSN since the bulk material is composed of siloxane bonds (excluding minor defects and trapped interparticle water) and the only proton spin bath comes from surface silanols making the method surface specific.²⁴ In a typical ^{29}Si CP-MAS spectrum, three peaks are present centered at -90 ppm (Q_2), -100 ppm (Q_3), and -110 ppm (Q_4) where the number represents the number of bridging siloxane bonds surrounding the central tetrahedrally coordinated silicon atom. In zeolites and other silicates, T coordinated sites are expected at -50 ppm (T_1), -60 ppm (T_2), and -70 ppm (T_3).^{25, 26} T_n sites represent direct Si-R coordination. No T_n sites were observed in any of the doped spectra, indicating that the metal atoms are incorporated into the siloxane network replacing tetrahedrally coordinated silicon and attaching bridging oxygens. ^{29}Si CP-MAS spectra (**Figure 3.1, Table 3.1**) were fit with the software package MestreNova. No major differences in peak shapes were observed for differing levels of Al or Ti-doping. The full width at half maximum (FWHM) increased with increased doping level for all Q_n sites in Al containing samples, with 10% doping exhibiting the largest FWHM. Compared to 0%FSN, the FWHM increased by ~ 65 Hz (Q_2), ~ 105 Hz (Q_3), ~ 260 Hz (Q_4). All sites are broadened indicating that Al is incorporated near the surface including Q_4 sites. A smaller overall change in FWHM is observed across Ti-dopants and 10%Ti only increases by ~ 7 Hz (Q_2), ~ 12 Hz (Q_3), and ~ 145 Hz (Q_4) compared to 0%FSN. The FWHM actually decreased in Q_2 by ~ 10 Hz from 1 to 7%Ti, in Q_3 by ~ 10 Hz from 1 to 3%Ti, and in Q_4 by ~ 15 Hz from 5 to 7%Ti, but this minor change is within the fitting error. The FWHM was slightly higher in Al dopings vs Ti dopings presumably due to the nominal charge difference where Al is +3 and Ti +4. Overall, the increase in linewidth with metal doping content indicates an

increased silica heterogeneity/disorder with Al-containing samples exhibiting the broadest resonances.

The relative abundances of Q_n sites were also analyzed and only minimal differences in Q_n ratios were observed. For Al-dopants, Q_2 populations remain the same across samples and Q_3 is converted to Q_4 as doping level increases assuming similar CP efficiency across samples. This is another indication that some of the aluminum sites may be congregating near the surface. In Ti-dopants, Q_3 gets converted to Q_2 and Q_4 but the changes are still minimal in comparison to Al. Lastly, chemical shift was analyzed, and changes are small (~ 0.5 to 1 ppm) but trend downfield with increasing dopant indicating a small decrease in T-O-T bond angle.^{27, 28}

Overall, the absence of any T_n sites among dopants confirms that the metal is incorporated into the framework through bridging oxygens. The FWHM all Q_n sites increases at the 10% level which suggest that at least some of the dopants are near the surface. Al dopants create a larger change in CP-MAS spectra than Ti dopants suggesting that Al makes the framework more disordered.

Table 3.1. ^{29}Si CP-MAS SSNMR data for doped samples.

	Q₂			Q₃			Q₄		
	Populati on	FWHM (Hz)	δ (ppm)	Populati on	FHWM (Hz)	δ (ppm)	Populati on	FWHM (Hz)	δ (ppm)
0% FSN	0.14	645	-91.0	0.69	881	-100.4	0.17	985	-110.4
1% Al	0.14	656	-91.0	0.66	882	-100.2	0.20	1050	-109.8
3% Al	0.15	656	-90.7	0.63	890	-99.8	0.21	1115	-109.3
5% Al	0.15	661	-90.6	0.60	939	-99.5	0.24	1164	-108.9
7% Al	0.15	675	-90.8	0.62	944	-99.6	0.23	1089	-108.8
10% Al	0.15	711	-90.7	0.59	986	-99.7	0.26	1246	-109.1
1% Ti	0.13	620	-91.5	0.66	875	-100.8	0.21	1014	-110.5
3% Ti	0.13	614	-91.5	0.64	865	-100.7	0.23	1108	-110.2
5% Ti	0.14	613	-91.0	0.62	874	-100.2	0.24	1112	-109.7
7% Ti	0.14	609	-90.7	0.62	886	-99.9	0.24	1096	-109.5
10% Ti	0.15	652	-91.0	0.62	893	-100.2	0.23	1129	-109.9

^{29}Si DP-MAS

^{29}Si DP-MAS NMR (**Figure 3.2**) was utilized to examine bulk structural changes for FSN samples as a function of metal doping. Due to the low signal intensity of protonated Q₂ and Q₃ sites in ^{29}Si DP-MAS experiments, the discussion will focus on Q₄ resonances that dominate the spectra and represent the bulk siloxane bonds. A long recycle delay (300 s) was used and spectra were scaled by mass for quantitative analysis. All samples had a broad Q₄ resonance due to the intrinsic amorphous nature of FSN. Since DP-MAS is a direct polarization technique and proton decoupling was applied during acquisition, broadening can be attributed to the degree of disorder within the bulk framework similar to the above discussions for CP-MAS results, specifically a larger distribution of Si-O-T (T = Al, Si, or Ti) bond angles and Si-O bond strengths, as well as Al and Ti disorder from the presence of multiple coordination sites (see ^{27}Al discussion below). While

Al and Ti are the next nearest neighbors (NNN) (i.e. not directly bound to silicon), they do have a deshielding effect on the observed ^{29}Si NMR isotropic chemical shift.^{27, 29-31}

In Al-doped samples, Q₄ intensity decreases as doping level increases from 1% to 5% indicating homogenous incorporation in the framework with increasing formation of Si-O-Al bonds. While Al is commonly found in multiple coordination environments, titanium is typically octahedrally coordinated as the rutile polymorph.³² However, previous studies have shown that at low metal doping levels in titanium-containing silicate glasses ($0.05 < \text{TiO}_2 < 9 \%$ (w/w)) the titanium cations are primarily tetrahedral with increasing levels of octahedral coordination as doping level increases.³³⁻³⁵ ^{29}Si Q₄ intensities of Ti-doped samples are scattered and no trends can be established (**Figure 3.2**). It is interesting to note that the 5% doping in both materials are outliers. 5%Ti has the largest Q₄ population after 0%FSN, followed by 1%Ti, then 3%/7%/10%Ti with the lowest. The absence of any trend or large change in Q₄ peak area and chemical shift suggests that Ti- is either phase separated from the Si-O-T network or that Ti is not incorporated in the framework at all. This will be discussed further in the Raman section.

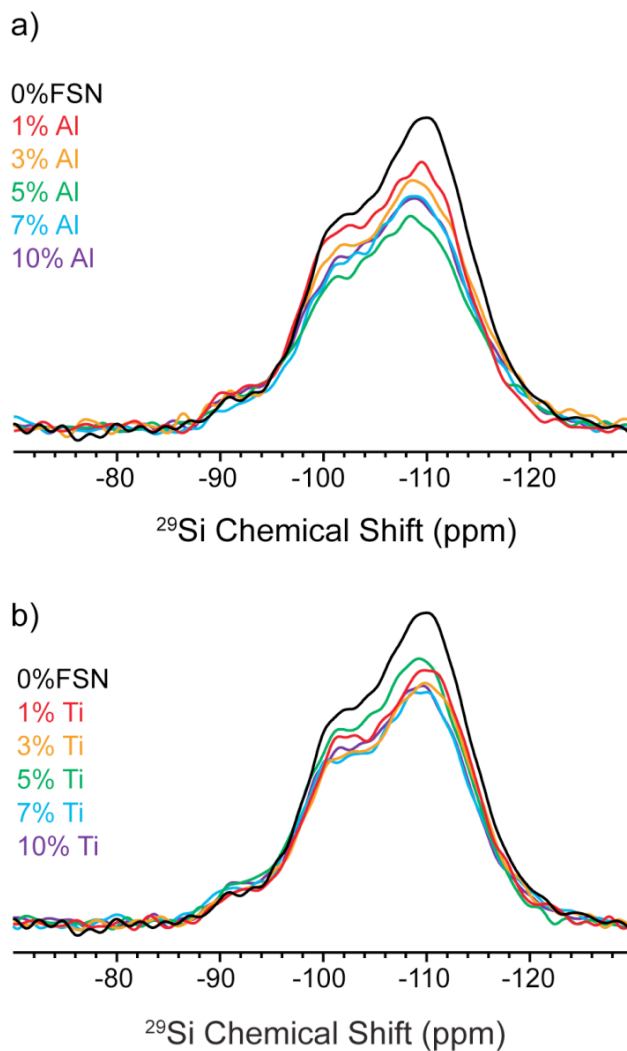


Figure 3.2. ^{29}Si DP-MAS NMR of Al- and Ti-doped samples with 0%FSN.

In addition to changes in Q_4 intensity, Q_4 resonances shift downfield as doping level increases. Many studies have been done that relate ^{29}Si DP-MAS NMR isotropic chemical shifts to Si-O-Si bond angle.^{27, 28, 30, 36-38} In this work, we used the equation published by Smith and Blackwell³⁸ derived from silica polymorphs and later applied to amorphous FSN by Legrand et al²⁸ to estimate the average Si-O-T bond angle of each dopant that is listed in **Table 3.2** for the

samples studied here. As the siloxane bond angles decrease, silicon atoms become deshielded and Q₄ shifts downfield. However, it is important to note that Al and Ti also have next-nearest-neighbor (NNN) deshielding effects leading to the Q₄ shift downfield.^{29, 31} Therefore, the chemical shift cannot be attributed to differences in bond angle alone. The total downfield shift from 0%FSN to 10%Al or 10%Ti is small (~ 1 ppm) although the trend would likely continue if doping levels were increased further. This is consistent with the results published by Ramdas et al, where ~ 5 ppm shift is observed in 25% Al content of zeolites and with Balmer et al, where a 5 – 10 ppm shift is observed at 25% Ti doped silica glass.^{29, 31}

Table 3.2. ²⁹Si Q₄ isotropic chemical shift from DP-MAS and predicted Si-O-T bond angle calculated from the equation derived by Smith & Blackwell.³⁸

	Al-doped (δ ppm)	α (°)	Ti-doped (δ ppm)	α (°)
0%FSN	-110.0	146.9	-110.0	146.9
1%	-109.6	146.4	-109.9	146.7
3%	-108.5	145.0	-109.7	146.5
5%	-108.3	144.8	-108.9	145.5
7%	-108.7	145.2	-109.4	146.1
10%	-108.8	145.4	-109.1	145.7

²⁷Al DP-MAS NMR

²⁷Al MAS NMR is a useful technique for determining Al coordination in inorganic materials. Due to limited sample quantity, only 1%, 5% and 10% Al were analyzed, as well as 10%Al following thermal treatment (overnight at 500 °C), rehydration, and adsorption of Ala (**Figure 3.3**). In all samples, at least three Al resonances are observed ~ 52, 12 and 0 ppm indicating presence of tetrahedral (52 ppm) and a minimum of two octahedral coordination sites (12, 0 ppm).

A large broad resonance is observed in all samples ~ 33 ppm. It is unclear whether this is due to the presence of a penta-coordinated species or additional strained tetrahedral sites that exhibit larger second-order quadrupole broadening compared to the traditional tetrahedral environment observed ~ 52 ppm.³⁹⁻⁴¹ The center of this resonance does not shift with doping level and remains considerably broad across 10%Al perturbations. Thermal treatment causes the signal ~ 33 ppm to increase and rehydration causes the tetrahedral peak ~ 52 ppm to increase and ~ 33 ppm signal to decrease. This is consistent with the work by Peeters et al where thermal treatment and ^{27}Al multiple quantum (MQ)-MAS was used to confirm that the ambiguous resonance ~ 33 ppm is actually due to a distorted tetrahedral environment experiencing a large quadrupole interaction, and not a penta-coordinated species as one would expect.⁴² Our samples exhibit similar behavior, and therefore we hypothesize that this resonance is likely due to a more strained tetrahedral coordination. Additionally, penta-coordinated sites are less common and are often unobservable due to the asymmetric nature of the site.⁴³⁻⁴⁵ In the literature $\text{Al}[\text{O}_5]$ sites were only observed in very high aluminum percentages (30% and 70%Al) as was shown previously for Al-doped FSN⁴⁴ and in zeolites (ZSM-5 and HZSM-5) following thermal treatment over 900 °C and rehydration.^{43,45}

^{27}Al is a $I=5/2$ quadrupolar nucleus, meaning local symmetry has a large effect on signal intensity and powder pattern lineshapes, so peak area is not indicative of relative populations.^{39, 40,}
⁴⁶ Typically, octahedrally coordinated sites have high symmetry and exhibit only first order quadrupolar contributions to the resonances with little to no second order contribution and is expected to have a stronger signal intensity.^{39, 40, 46} However, the metal doping levels analyzed here are all dominated by tetrahedrally coordinated $\text{Al}[\text{O}_4]$ (~ 52 ppm) environments. This is expected since aluminum atoms are replacing tetrahedrally coordinated silicon. 1%Al and 5%Al appear

mostly tetrahedral, and 10%Al has strong contributions from both tetrahedral and octahedral regions.

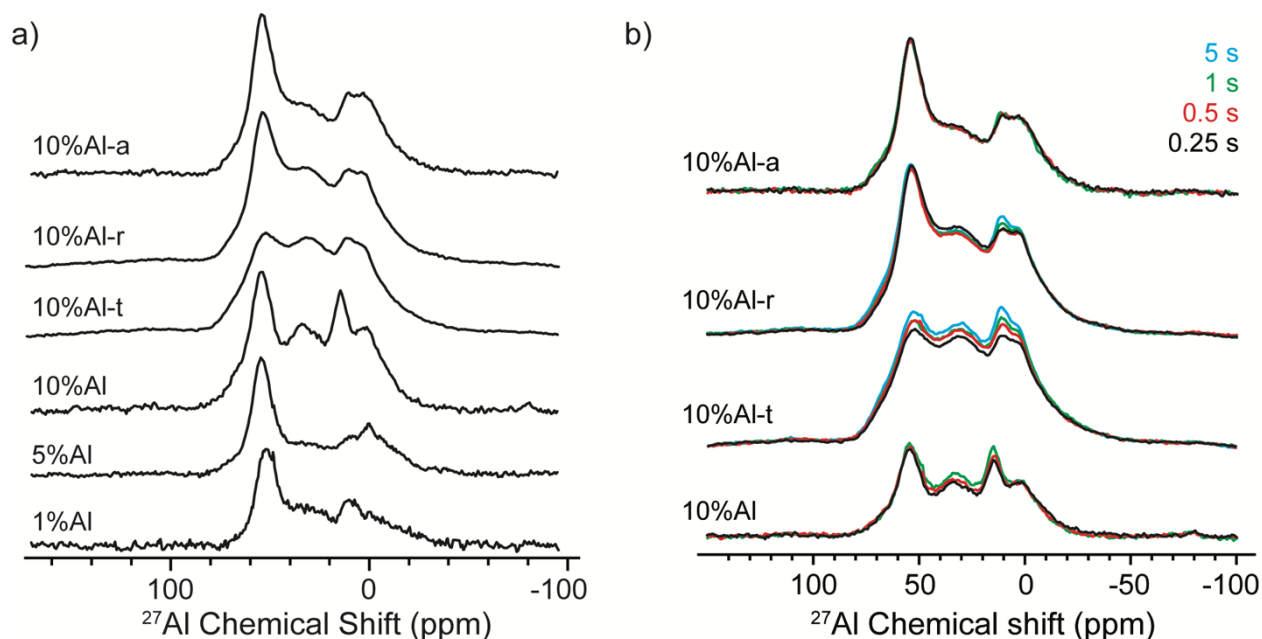


Figure 3.3. ^{27}Al DP-MAS NMR of Al-doped samples. Spectra were collected at 15 kHz MAS. A recycle delay of a) 0.25 sec and b) variable delay between 0.25 and 5 s were used. The following notation is used to indicate treatments applied to 10%Al FSN: 10%Al-t (thermal treated), 10%Al-r (rehydrated), and 10%Al-a (alanine adsorbed).

In the 10%Al-SiO₂ sample, there is not much change after heating. The tetrahedral and octahedral resonances broaden due to disorder and restricted dynamics. Heating impacts T_1 relaxation of all sites which we observe by the peak intensities increasing with increasing recycle delay (**Figure 3.3**). After rehydration, only the downfield octahedral resonance exhibits changes with increasing recycle delay. This suggests that this site is either in the framework and unaffected by local dynamics or rearrangement at the surface after rehydration, or that this is a separate

population of small alumina particles that have increased T_1 due to a difference in dynamics. This will be discussed further in the next section where ^{27}Al CP-MAS was collected on 10% heated and rehydrated, and the upfield octahedral site has the largest CP signal, suggesting this site is close to or at the highly protonated surface.

In addition to ^{29}Si , ^{27}Al resonances are also deshielded with increasing %Al. While we cannot accurately report chemical shifts from a basic Lorentzian Gaussian line fit, it is obvious that the $\text{Al}[\text{O}_4]$ and $\text{Al}[\text{O}_6]$ regions shift downfield as doping level increases. $\text{Al}[\text{O}_4]$ shifts <1 ppm from 5% to 10% and <1 ppm after calcination and rehydration supporting that aluminum was homogeneously incorporated in the framework. The $\text{Al}[\text{O}_6]$ site, however, shifts 5 ppm downfield from 1% to 10% which could mean that the octahedral sites are potentially the result of phase-separation. If ^{27}Al nuclei are deshielded with increasing aluminum content, this means either an increase in ^{27}Al NNN (more Al-O-Al bonds) or Al nuclei are sensitive to the long-range electron withdrawing effects (less likely). The idea of phase-separation for the highest doping level is in agreement with ^{29}Si DP-MAS which shows a slight increase in ^{29}Si Q₄ content at 10%Al.

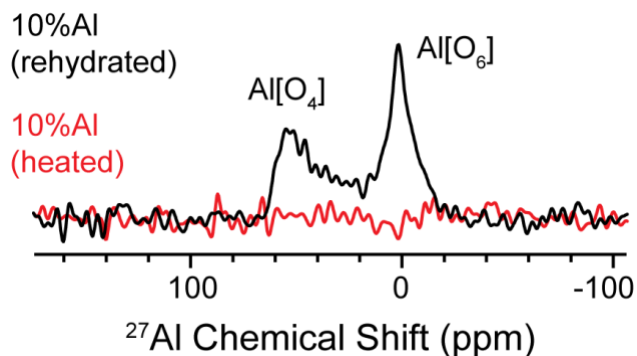


Figure 3.4. ^{27}Al CP-MAS NMR of 10%Al- doped samples after heating and rehydration.

²⁷Al CP-MAS

²⁷Al CP-MAS was collected on 10%Al-SiO₂ following heating and rehydration (**Figure 3.4**). No signal was observed in the heated sample when a short contact pulse was used (500 μs). Following rehydration, some Al[O₄] and Al[O₆] sites were observed. This indicates that a portion of the Al[O₄] and Al[O₆] environments are located near surface hydroxyls or water but may not be directly bound. Aluminum hydroxides are present in penta and octahedrally coordinated materials;^{44, 47, 48} thus, we cannot rule out the possibility that a small population of hydroxylated alumina particles are present in the system, causing the Al[O₆] resonance ~ 12 ppm. This would explain the increased signal intensity and sharp linewidth upon rehydration. It also agrees with ²⁹Si DP-MAS data where an increase in Q₄ population occurs at 7% and 10%Al which likely indicates formation of more undoped FSN. The presence of small alumina particles was seen in a previous study of Al-containing silica sol-gel derived materials where MQMAS was used to measure quadrupole parameters that were similar to that of alumina⁴² and could be a possibility here. It is also interesting to note that the broad ²⁷Al resonance ~ 33 ppm is for the most part absent compared to the ²⁷Al DP-MAS NMR spectrum (**Figure 3.3**) indicating that this environment is associated with the bulk Al-doped FSN and not spatially close to surface protons.

Raman Spectroscopy

The Raman spectra of 0%FSN display characteristic silica stretching modes (oxygen bending motion in the random network denoted as “R” ~ 440 cm⁻¹, stretching vibrations of Si-O-Si ~ 800 cm⁻¹, and Si-(OH) stretching ~ 950 cm⁻¹) and strained defects (oxygen breathing vibrations of strained 4- and 3- membered rings denoted as “D1” ~ 495 cm⁻¹ and “D2” ~ 605 cm⁻¹, respectively).^{49, 50} Al-doped samples produced too much fluorescence for analysis (**Figure 3.S1**)

so only Ti-doped samples will be discussed here. Five of the 6 Raman active anatase stretching modes were observed in all Ti-doped samples with no evidence of rutile coordination (**Figure 3.5**). Previous studies on Ti-doped FSN found that octahedral coordination is preferred in Ti >9%, and that either rutile or anatase coordination is possible and is determined by the mode of glass preparation.^{33, 34} Silicon is a known inhibitor of rutile transformation so it is not surprising that anatase is observed even though rutile is the thermodynamically and kinetically stable polymorph.³² The anatase stretching modes dominate all Ti-dopants and convolute the silica strain ring defects making them unobservable. This is unfortunate as the presence of strained ring defects appears to correlate with the amino acid thermal condensation reactivity of FSN¹⁷ (discussed below).

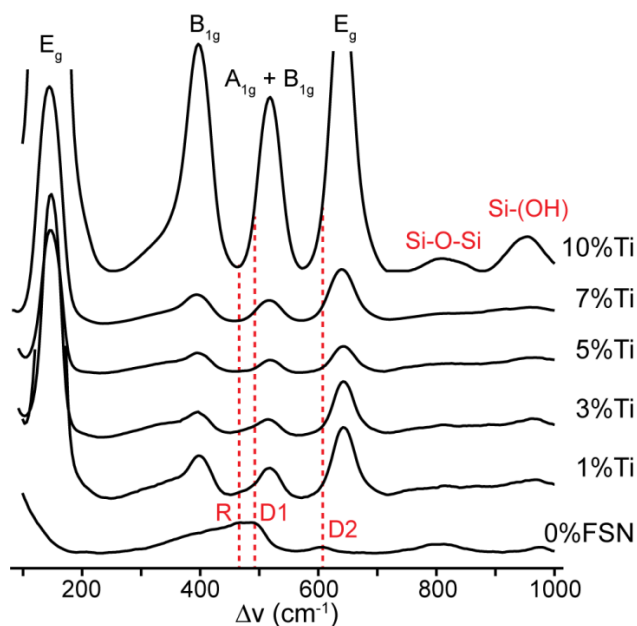


Figure 3.5. Raman spectra of 0%FSN and Ti-doped FSN.

5%Ti has the weakest anatase peaks which is in agreement with ^{29}Si DP-MAS that show 5% has the largest ^{29}Si Q₄ intensity. Surprisingly, the silica stretching modes are most pronounced in 10%Ti-SiO₂ where anatase peaks are also the strongest. This supports that phase separation is a strong possibility for the Ti-doped samples and is also consistent with ^{29}Si MAS NMR results discussed above. Anatase is crystalline and the peaks in 10%Ti are significantly more intense than any of the other dopings.³² This would also explain the increase in silica stretching modes as well for this sample.

In Balmer et al's analysis of the titanosilicate pollucite (CsTiSi₂O_{6.5}) Ti- and Si- stretching and bending modes were significantly broadened and convoluted.³¹ Huang et al analyzed amorphous TiO₂ xerogel as well as crystalline anatase and rutile polymorphs.⁵¹ In the amorphous form, the peaks are so broad they are unresolvable. The anatase peaks in our doped samples look like that of pure crystalline anatase leading to the conclusion that anatase is the primary containing component of the sample and incorporation into the FSN framework through Si-O-T bonding is low.

TGA Thermal Analysis

TGA monitors sample weight loss as a function of temperature and can be used to determine the amount of adsorbed water and organic species. TGA can also be used to observe thermal condensation reactions for adsorbed amino acids by detecting the water loss during the formation of peptide bonds.^{14, 15, 52-54} Because of the limited amount of material only two TGA runs could be conducted per metal doped FSN sample. Some variation exists within each sample depending on environmental humidity, starting temperature of furnace, and N₂ tank pressure; thus, the average of both runs is reported.

The hydroxyl content (OH/nm²), primary particle size (nm), and surface area (m²/g) were quantified by BET and are reported in **Table 3.3**. Together, these values determine the number of available ligand binding sites which is one of the primary traits that determine the amount of Ala that will bind. The weight loss reported in **Table 3.3** is the loss of Ala, measured from 100 to 600 °C. All doped NPs were within ± 1% of 0%FSN indicating that doping level has little effect on the amount of adsorbed alanine. The average weight loss quantified by TGA (**Figure 3.S2**) was 6.25% for 0%FSN, 7.06 ± 0.39% (Al-doped NPs), and 6.83 ± 0.53% (Ti-doped NPs). The average of both Al- and Ti- dopants was higher than 0%FSN with small standard deviations. When the surface area is accounted for determining the number of Ala molecules/nm², it becomes evident that the adsorption capacity roughly decreases with increasing metal doping content and decreasing OH/nm² (**Table 3.3**).

Table 3.3. BET analysis and TGA calculations.

Doping Level	SSA (m ² /g)	Diameter (nm)	OH/nm ²	0.10M L-Ala			
				Wt Loss (%)	Molecules Ala (/nm ²)	Molecules H ₂ O _(TC) (/nm ²)	
0%FSN	269	8.4	6.0	6.25	1.69	2.72	
1%Al	334	6.7	2.8	7.37	1.62	2.33	
3%Al	363	6.2	1.2	7.30	1.48	2.16	
5%Al	363	6.0	1.0	6.81	1.38	1.96	
7%Al	357	6.1	0.7	7.35	1.52	2.23	
10%Al	357	6.0	1.8	6.50	1.33	1.72	
1%Ti	339	6.6	4.5	6.70	1.44	2.00	
3%Ti	346	6.4	5.0	6.74	1.42	1.98	
5%Ti	338	6.5	2.6	7.58	1.66	2.08	
7%Ti	348	6.3	1.7	7.02	1.49	2.12	
10%Ti	361	5.9	1.0	6.12	1.24	1.65	

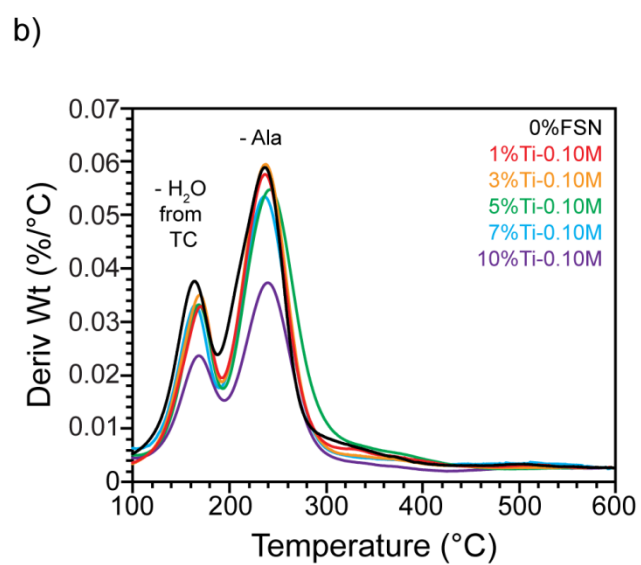
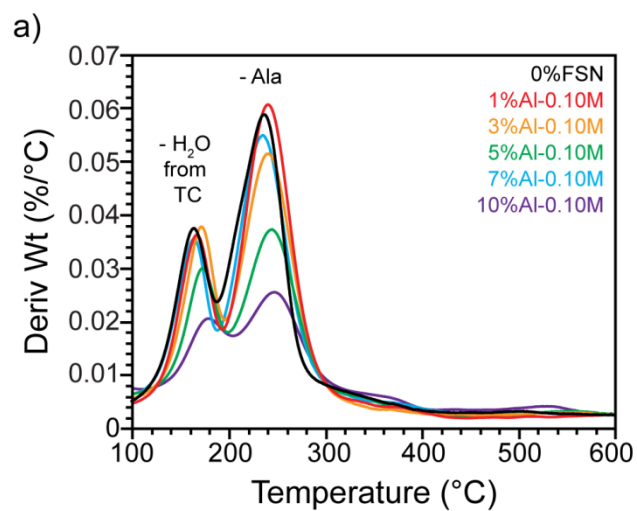


Figure 3.6. DTG curves of 0%FSN and a) Al- and b) Ti-doped FSN with 0.10M Ala adsorbed.

One of the properties that make FSN unique is its efficacy in catalyzing the thermal condensation and oligomerization of adsorbed amino acids.^{18-20, 54-56} The first derivative thermogram (DTG) was analyzed where peptide bond formation is easily visualized by a peak ~ 165 °C caused by water loss from the thermal condensation (TC) of neighboring adsorbed amino acid molecules.^{14, 15, 17, 19, 20, 54, 57, 58} Guo et al found that FSN converts alanine into the dipeptide alanine anhydride with nearly 100% efficiency after just 3 hours of thermal treatment at 170 °C compared to colloidal forms that only converted 50%.¹⁷ We verified that the structure of our thermal condensation product is also alanine anhydride, which makes the DTG peak ~ 165 °C a good indicator of the catalytic activity of each metal doped FSN sample. DTG curves are shown in **Figure 3.6**.

3% Al- and Ti-NPs had the largest TC peaks after 0%FSN. 10% dopants exhibited the greatest reduction in TC with amino acid degradation peaks accompanied by peak broadening which points to disorder at the surface causing thermal events to occur over a broader range of temperatures. 10%Al performed the worst among the Al dopants in the context of both amino acid loading capacity and thermal condensation. It had the lowest number of Ala molecules adsorbed and the broadest DTG peaks. DTG peaks for Ti dopants showed less variation, and the thermal events were well defined and narrow, with 1% and 3%Ti performing comparably to 0%FSN. 10%Ti performed the worst among Ti dopants with the lowest amount of adsorbed Ala molecules.

The number of molecules of water lost in the TC region (100 – 200 °C) was also calculated and is shown in **Table 3.3**. The number of water molecules lost in the TC region is higher than the number of adsorbed Ala molecules, which suggests there is more than 1 water loss per Ala molecule. This could be due to an interfacial water layer at the FSN interface that is trapped between the FSN and the adsorbed Ala amino acid. This has been observed previously with some

amino acids and lipids adsorbed on silica nanoparticles.^{18, 54, 59} Since these water molecules are interacting more closely with silanols and alanine molecules at the surface, it presumably come off at a temperature above 100 °C. There is approximately one additional water molecule per Ala which is consistent with a single water monolayer. Therefore, the number of molecules of water lost in the TC region is likely a reflection of both the efficiency of the surface catalyzing these TC reactions plus an additional water molecule per Ala that is due to the surface bound water monolayer. Overall, these changes are minor and indicate that the thermal condensation reactivity is not all that different, but does roughly trend lower with increasing metal doping.

Conclusion

The work presented here is part of a larger investigation toward safer alternatives for FSN production. Previous studies show that metal doping improves the inflammatory and cytotoxicity effects of FSN exposure in cells. The focus of this study was to determine if metal doping FSN impacted the bulk molecular structure and surface chemistry with respect to amino acid adsorption and thermal condensation compared to commercial grade FSN. TGA was used to analyze the adsorption capacity of each dopant and assess the reactivity by measuring the thermal condensation efficiency. All metal doped FSN samples had a molecular adsorption (molecules/nm²) capacity that roughly decreased with increasing metal doping that is likely due to decreasing OH⁻ population with metal dopant. Only minor differences were observed in thermal condensation peak temperature and reactivity, relative CP populations, and ²⁹Si Q₂ FWHM. ²⁹Si Q₃ and Q₄ FWHM, measured by CP-MAS (surface selective) increased with doping level (300 – 400 Hz broader than FSN) indicating more disorder near the surface (i.e., a distribution in Si-O bond lengths and bond angles). The ²⁹Si DP-MAS chemical shift of Q₄ increased with doping level, which could be due

to either larger Si-O-T bond angles, deshielding effects from Al/Ti, or both. Our data suggests that Al was incorporated into the framework in 1% and 3%Al-FSN and may congregate near the surface or as separate alumina particles in 7% and 10%Al. Phase separation is likely for Ti dopings as ^{29}Si DP-MAS Q_4 intensities were all similar and clear anatase stretching modes were observed in Raman, indicating the presence of anatase crystals. It is interesting that in both ^{29}Si MAS NMR, Raman, and TGA the same dopant is the outlier (7%Al and 5%Ti). Paired with previous work, 1% and 3% Al- and Ti-doped FSN seem to offer a less toxic alternative to FSN and interestingly, the decreased toxicity correlates with a decrease in amino acid adsorption capacity and thermal condensation reactivity.

Acknowledgements

We acknowledge the use of facilities within the Eyring Materials Center at Arizona State University supported in part by NNCI-ECCS-1542160. The authors would also like to thank funding from the NASA Fellowship 80NSSC19K0064.

Chapter 3, in full, is a reprint of the material as it appears published by Springer in the Journal of Materials Science 2021. The dissertation author Haley L. Swanson was the primary investigator and author of this paper. Supporting authors include Suman Pokhrel, Stephen K. Davidowski, Lutz Mädler, C. Jeffrey Brinker, and Gregory P. Holland.

Supplemental Information

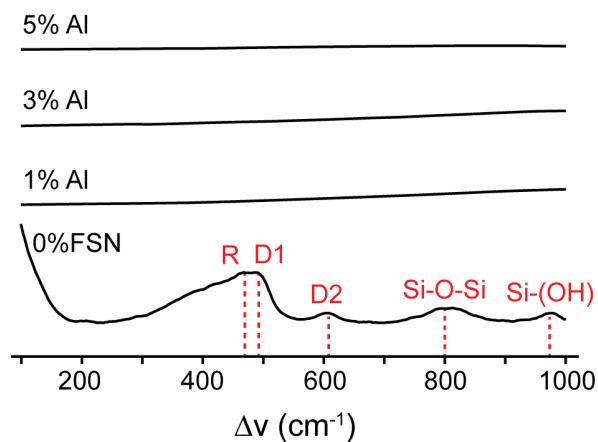


Figure 3.S1. Raman spectra of 0%FSN and Al-doped FSN.

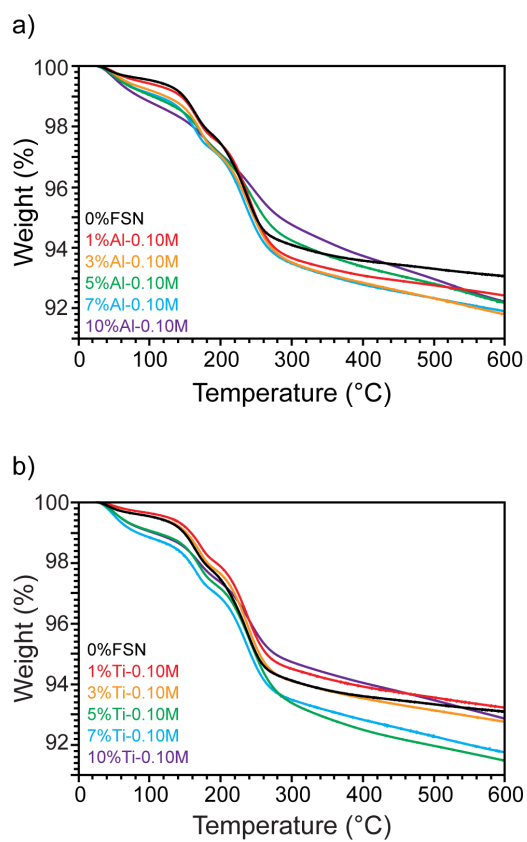


Figure 3.S2. Thermograms of 0.10M alanine adsorbed on 0%FSN, a) Al-doped FSN, and b) Ti-doped FSN.

References

1. Regulations, C. o. F., 21. In 1, Administration, U. S. F. a. D., Ed. Department of Health and Human Services: *Code of Federal Regulations*, **2020**; Vol. B.
2. Zhang, H.; Dunphy, D. R.; Jiang, X.; Meng, H.; Sun, B.; Tarn, D.; Xue, M.; Wang, X.; Lin, S.; Ji, Z.; Li, R.; Garcia, F. L.; Yang, J.; Kirk, M. L.; Xia, T.; Zink, J. I.; Nel, A.; Brinker, C. J., Processing pathway dependence of amorphous silica nanoparticle toxicity: colloidal vs pyrolytic. *J Am Chem Soc* **2012**, *134* (38), 15790-804.
3. Sun, B.; Pokhrel, S.; Dunphy, D. R.; Zhang, H.; Ji, Z.; Wang, X.; Wang, M.; Liao, Y. P.; Chang, C. H.; Dong, J.; Li, R.; Madler, L.; Brinker, C. J.; Nel, A. E.; Xia, T., Reduction of Acute Inflammatory Effects of Fumed Silica Nanoparticles in the Lung by Adjusting Silanol Display through Calcination and Metal Doping. *ACS Nano* **2015**, *9* (9), 9357-72.
4. Sun, B.; Wang, X.; Liao, Y. P.; Ji, Z.; Chang, C. H.; Pokhrel, S.; Ku, J.; Liu, X.; Wang, M.; Dunphy, D. R.; Li, R.; Meng, H.; Madler, L.; Brinker, C. J.; Nel, A. E.; Xia, T., Repetitive Dosing of Fumed Silica Leads to Profibrogenic Effects through Unique Structure-Activity Relationships and Biopersistence in the Lung. *ACS Nano* **2016**, *10* (8), 8054-66.
5. Croissant, J. G.; Butler, K. S.; Zink, J. I.; Brinker, C. J., Synthetic amorphous silica nanoparticles: toxicity, biomedical and environmental implications. *Nat Rev Mater* **2020**, *5* (12), 886-909.
6. Tallant, D. R.; Bunker, B. C.; Brinker, C. J.; Balfe, C. A., Raman Spectra of Rings in Silicate Materials. *MRS Proceedings* **1986**, *73*, 261.
7. McKee, A. D.; Solano, M.; Saydjari, A.; Bennett, C. J.; Hud, N. V.; Orlando, T. M., A Possible Path to Prebiotic Peptides Involving Silica and Hydroxy Acid-Mediated Amide Bond Formation. *ChemBiochem* **2018**, *19* (18), 1913-1917.
8. Brack, A., From interstellar amino acids to prebiotic catalytic peptides: a review. *Chem Biodivers* **2007**, *4* (4), 665-79.
9. Rode, B. M., Peptides and the origin of life. *Peptides* **1999**, *20* (6), 773-86.
10. Bujdak, J.; Eder, A.; Yongyai, Y.; Faybikova, K.; Rode, B. M., Investigation on the mechanism of peptide chain prolongation on montmorillonite. *J Inorg Biochem* **1996**, *61* (1), 69-78.
11. Erastova, V.; Degiacomi, M. T.; D, G. F.; Greenwell, H. C., Mineral surface chemistry control for origin of prebiotic peptides. *Nat Commun* **2017**, *8* (1), 2033.
12. Lambert, J. F., Adsorption and polymerization of amino acids on mineral surfaces: a review. *Orig Life Evol Biosph* **2008**, *38* (3), 211-42.

13. Rimola, A.; Costa, D.; Sodupe, M.; Lambert, J. F.; Ugliengo, P., Silica surface features and their role in the adsorption of biomolecules: computational modeling and experiments. *Chem Rev* **2013**, *113* (6), 4216-313.
14. Meng, M.; Stievano, L.; Lambert, J.-F., Adsorption and Thermal Condensation Mechanisms of Amino Acids on Oxide Supports. 1. Glycine on Silica. *Langmuir* **2004**, *20* (22), 914-923.
15. Lahav, N.; White, D.; Chang, S., Peptide formation in the prebiotic era: thermal condensation of glycine in fluctuating clay environments. *Science* **1978**, *201* (4350), 67-9.
16. Liebau, F., Structural chemistry of silicates: structure, bonding, and classification. Springer Science & Business Media: **2012**.
17. Guo, C.; Jordan, J. S.; Yarger, J. L.; Holland, G. P., Highly Efficient Fumed Silica Nanoparticles for Peptide Bond Formation: Converting Alanine to Alanine Anhydride. *ACS Appl Mater Interfaces* **2017**, *9* (20), 17653-17661.
18. Swanson, H. L.; Guo, C.; Cao, M.; Addison, J. B.; Holland, G. P., Probing the binding modes and dynamics of histidine on fumed silica surfaces by solid-state NMR. *Phys Chem Chem Phys* **2020**, *22* (36), 20349-20361.
19. Bouchoucha, M.; Jaber, M.; Onfroy, T.; Lambert, J.-F.; Xue, B., Glutamic Acid Adsorption and Transformations on Silica. *J Phys Chem C* **2011**, *115* (44), 21813-21825.
20. Lambert, J. F.; Jaber, M.; Georgelin, T.; Stievano, L., A comparative study of the catalysis of peptide bond formation by oxide surfaces. *Phys Chem Chem Phys* **2013**, *15* (32), 13371-80.
21. Wang, Z.; Pokhrel, S.; Chen, M.; Hunger, M.; Mädler, L.; Huang, J., Palladium-doped silica–alumina catalysts obtained from double-flame FSP for chemoselective hydrogenation of the model aromatic ketone acetophenone. *J Catal* **2013**, *302*, 10-19.
22. Kim, K. D.; Pokhrel, S.; Wang, Z.; Ling, H.; Zhou, C.; Liu, Z.; Hunger, M.; Mädler, L.; Huang, J., Tailoring High-Performance Pd Catalysts for Chemoselective Hydrogenation Reactions via Optimizing the Parameters of the Double-Flame Spray Pyrolysis. *ACS Catalysis* **2016**, *6* (4), 2372-2381.
23. Pokhrel, S.; Birkenstock, J.; Schowalter, M.; Rosenauer, A.; Mädler, L., Growth of Ultrafine Single Crystalline WO₃ Nanoparticles Using Flame Spray Pyrolysis. *Cryst Growth Des* **2010**, *10* (2), 632-639.
24. Liu, C. H. C.; Maciel, G. E., The fumed silica surface: A study by NMR. *J Am Chem Soc* **1996**, *118* (21), 5103-5119.

25. Burkett, S. L.; Sims, S. D.; Mann, S., Synthesis of hybrid inorganic-organic mesoporous silica by co-condensation of siloxane and organosiloxane precursors. *ChemComm* **1996**, (11), 1367-1368.
26. van der Graaff, W. N. P.; Olvera, K. G.; Pidko, E. A.; Hensen, E. J. M., Stability and catalytic properties of porous acidic (organo)silica materials for conversion of carbohydrates. *J Mol Catal A* **2014**, 388-389, 81-89.
27. Merzbacher, C. I.; Sherriff, B. L.; Hartman, J. S.; White, W. B., A high-resolution ^{29}Si and ^{27}Al NMR study of alkaline earth aluminosilicate glasses. *J Non Cryst Solids* **1990**, *124*, 194-206.
28. Legrand, A. P.; Taibi, H.; Hommel, H.; Tougne, P.; Leonardelli, S., Silicon functionality distribution on the surface of amorphous silicas by ^{29}Si solid state NMR. *J Non Cryst Solids* **1993**, *155*, 122-130.
29. Ramdas, S.; Klinowski, J., A simple correlation between isotropic ^{29}Si -NMR chemical shifts and T-O-T angles in zeolite frameworks. *Nature* **1984**, *308*, 521-523.
30. Oestrike, R.; Yang, W.; Kirkpatrick, R. J.; Hervig, R. L.; Navrotsky, A.; Montez, B., High-resolution ^{23}Na , ^{27}Al , ^{29}Si NMR spectroscopy of framework aluminosilicate glasses. *Geochim Cosmochim Acta* **1987**, *51*, 2199-2209.
31. Balmer, M. L.; Bunker, B. C.; Wang, L. Q.; Peden, C. H. F.; Su, Y., Solid-State ^{29}Si MAS NMR Study of Titanosilicates. *J Phys Chem B* **1997**, *101*, 9170-9179.
32. Hanaor, D. A. H.; Sorrell, C. C., Review of the anatase to rutile phase transformation. *J Mater Sci* **2010**, *46* (4), 855-874.
33. Sandstrom, D. R.; Lytle, F. W.; Wei, P. S. P.; Greeger, R. B.; Wong, J.; Schultz, P., Coordination of Ti in TiO_2 - SiO_2 Glass by X-Ray Absorption Spectroscopy. *J Non Cryst Solids* **1980**, *41*, 201-207.
34. Greeger, R. B.; Lytle, F. W.; Sandstrom, D. R.; Wong, J.; Schultz, P., Investigation of TiO_2 - SiO_2 Glasses by X-Ray Absorption Spectroscopy. *J Non Cryst Solids* **1983**, *55*, 27-43.
35. Schneider, E.; Wong, J.; Thomas, J. M., Multinuclear solid state NMR investigation of titanium-containing silicate glasses. *J Non Cryst Solids* **1991**, *136*, 1-13.
36. Dupree, R.; Pettifer, R. F., Determination of the Si-O-Si Bond Angle Distribution in Vitreous Silica by Magic Angle Spinning Nmr. *Nature* **1984**, *308* (5959), 523-525.
37. Brinker, C. J.; Kirkpatrick, R. J.; Tallant, D. R.; Bunker, B. C.; Montez, B., NMR Confirmation of Strained "Defects" in Amorphous Silica. *J Non Cryst Solids* **1988**, *99*, 418-428.

38. Smith, J. V.; Blackwell, C. S., Nuclear Magnetic-Resonance of Silica Polymorphs. *Nature* **1983**, *303* (5914), 223-225.
39. Autschbach, J.; Zheng, S.; Schurko, R. W., Analysis of electric field gradient tensors at quadrupolar nuclei in common structural motifs. *Concepts Magn Reson A* **2010**, *36A* (2), 84-126.
40. Ashbrook, S. E.; Duer, M. J., Structural information from quadrupolar nuclei in solid state NMR. *Concepts Magn Reson A* **2006**, *28A* (3), 183-248.
41. Ray, G. J.; Samoson, A., Double rotation and variable field ^{27}Al NMR study of dealuminated Y zeolites. *Zeolites* **1993**, *13*, 410-413.
42. Peeters, M. P. J.; Kentgens, A. P., M., A ^{27}Al MAS MQMAS and off resonance nutation NMR study of aluminum containing silica-based sol-gel materials. *Solid State Nucl Mag* **1997**, *9*, 203-217.
43. Deng, F.; Du, Y.; Ye, C.; Wang, J.; Ding, T.; Li, H., Acid Sites and Hydration Behavior of Dealuminated Zeolite HZSM-5: A High-Resolution Solid State NMR Study. *J Phys Chem* **1995**, *99*, 15208-15214.
44. Huang, J.; van Vegten, N.; Jiang, Y.; Hunger, M.; Baiker, A., Increasing the Bronsted acidity of flame-derived silica/alumina up to zeolitic strength. *Angew Chem Int Ed* **2010**, *49* (42), 7776-81.
45. Kanellopoulos, J.; Unger, A.; Schwieger, W.; Freude, D., Catalytic and multinuclear MAS NMR studies of a thermally treated zeolite ZSM-5. *J Catal* **2006**, *237* (2), 416-425.
46. Massiot, D.; Bessada, C.; Coutures, J. P.; Taulelle, F., Quantitative study of ^{27}Al MAS NMR in crystalline YAG. *J Magn Reson* **1990**, *90*, 231-242.
47. Lookman, R.; Grobet, P.; Merckx, R.; Van Riemsdijk, W. H., Application of ^{31}P and ^{27}Al MAS NMR for phosphate speciation studies on soil and aluminum hydroxides: promises and constraints. *Geoderma* **1997**, *80*, 369-388.
48. Singh, P. S.; Bastow, T.; Trigg, M., Structural studies of geopolymers by ^{29}Si and ^{27}Al MAS-NMR. *J Mater Sci* **2005**, *40*, 3951-3961.
49. Geissberger, A. E.; Galeener, F. L., Raman studies of vitreous SiO_2 versus fictive temperature. *Phys Rev B* **1983**, *28* (6), 3266-3271.
50. Vaccaro, G.; Angnello, S.; Buscarino, G.; Gelardi, F. M., Thermally Induced Structural Modifications of Silica Nanoparticles Investigated by Raman and Infrared Absorption Spectroscopies. *J Phys Chem C* **2010**, *114*, 13991-13997.

51. Huang, P. J.; Chang, H.; Yeh, C. T.; Tsai, C. W., Phase transformation of TiO₂ monitored by Thermo-Raman spectroscopy with TGA/DTA. *Thermochim Acta* **1997**, *297*, 85-92.
52. Bujdak, J., The effect of reaction conditions on montmorillonite-catalysed peptide formation. *Catal Letters* **1996**, *37*, 267-272.
53. Fuchida, S.; Masuda, H.; Shinoda, K., Peptide formation mechanism on montmorillonite under thermal conditions. *Orig Life Evol Biosph* **2014**, *44* (1), 13-28.
54. Guo, C.; Holland, G. P., Alanine Adsorption and Thermal Condensation at the Interface of Fumed Silica Nanoparticles: A Solid-State NMR Investigation. *J Phys Chem C* **2015**, *119* (45), 25663-25672.
55. Lambert, J.-F.; Stievano, L.; Lopes, I.; Gharsallah, M.; Piao, L., The fate of amino acids adsorbed on mineral matter. *Planet Space Sci* **2009**, *57* (4), 460-467.
56. Stievano, L.; Piao, L. Y.; Lopes, I.; Meng, M.; Costa, D.; Lambert, J. F., Glycine and lysine adsorption and reactivity on the surface of amorphous silica. *Eur J Mineral* **2007**, *19* (3), 321-331.
57. Guo, C.; Holland, G. P., Investigating Lysine Adsorption on Fumed Silica Nanoparticles. *J Phys Chem C* **2014**, *118* (44), 25792-25801.
58. Rimola, A.; Tosoni, S.; Sodupe, M.; Ugliengo, P., Does silica surface catalyse peptide bond formation? New insights from first-principles calculations. *Chemphyschem* **2006**, *7* (1), 157-63.
59. Bayerl, T. M.; Bloom, M., Physical properties of single phospholipid bilayers absorbed to micro glass beads. *Biophys J* **1990**, *58*, 357-362.

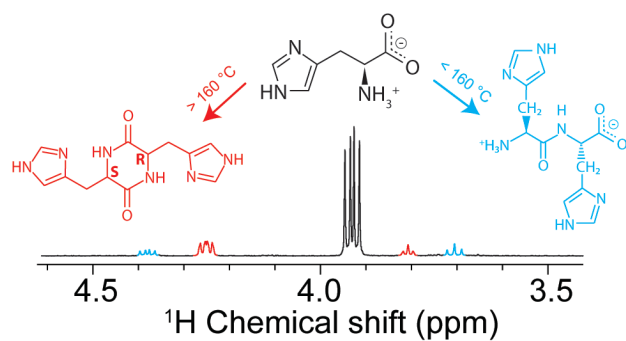
Chapter 4

Assembly and thermal-induced polymerization of histidine on fumed silica surfaces

Abstract

A thorough investigation into the thermal condensation reaction of histidine (His) on fumed silica nanoparticles (FSN) was performed. Thermogravimetric analysis (TGA) was used to track thermal events and characterize the optimal temperature for thermal condensation reactions for His adsorbed to FSN. Lower temperature thermal cycling was used to investigate the possibility of linear polymerization. The products were characterized using one- (1D) and two-dimensional (2D) solution and solid-state nuclear magnetic resonance (NMR) spectroscopy and mass spectrometry (MS). The formation of His diketopiperazine (DKP) was the major product and is produced at two distinct thermal condensation temperatures. Under low temperature thermal condensation conditions, a linear His-His dipeptide is also formed which is relevant to origin of life research and points to some potential conditions for promoting His linearization. Possible explanations for two discrete thermal events for His/FSN complexes are presented that indicate variable His binding modes influence His polymerization and that molecular re-orientation may be required for complete conversion to DKP. DTG of other amino acids on FSN are included for context and illustrate that two thermal events are characteristic of amino acids with a functional basic sidechain.

Graphical Abstract



Introduction

Silica surfaces are of interest to origin of life scientists because of their catalytic effect on the polymerization of prebiotic molecules.^{1,2} Silicon and oxygen are the most abundant elements on Earth so it is no surprise that silica (SiO₂) composes over 60% of the Earth's crust.³ Decades of research support the presence of amino acids on prebiotic Earth and in meteorites,⁴⁻⁷ but the pathway to increasing biological complexity is not well understood. Lambert et al has assessed the catalytic potential of various silica and other mineral oxide surfaces for the polymerization of glycine (Gly) and found that fumed silica nanoparticles (FSN) and mesoporous silica nanoparticles (MSN) showed the greatest catalytic activity while, surprisingly, clays were much less efficient.⁸ Thermal condensation reactions involving Gly have been well studied because it is the simplest amino acid and also considered one of the most common prebiotic amino acids as it was produced in the Miller-Urey experiments and was present in meteorites.^{7,9,10} Forsythe et al discovered that linear chain polymerization is much more favorable in the presence of L-lactic acid through ester-bond mediation.¹¹ Further investigations of alanine adsorption on FSN determined that alanine can be converted to alanine anhydride with nearly 100% yield when exposed to heat for just 3 hours compared to colloidal silica nanoparticles that only exhibited ~50% yield.¹² Other studies found that FSN significantly lowers the activation energy for the self-cyclization of glutamic acid,¹³ and that polypeptides can form from one step heating procedures of binary amino acid systems adsorbed on FSN.¹⁴

While histidine (His) is not generally considered a prebiotic amino acid,¹⁰ it may have played an important role in prebiotic chemical evolution due to its potential to function as a novel enzyme. The protonation of the His side chain occurs at near neutral pH, allowing it to complex with metals, form catalytic triads, and participate in hydrogen bonding. In the simplest form, the

addition of His alone has been shown to increase oligomerization of alanine and lysine.¹⁵ His-containing dipeptides also exhibit catalytic properties by promoting the polymerization of amino acids and nucleic acids.^{16, 17} Histidyl-histidine can be synthesized under prebiotic conditions,¹⁸ and could have helped create an early self-reproducing chemical system.¹⁹ In this work, we present an equally plausible route of prebiotic His-dipeptide synthesis and explore polymerization mechanisms of short His-containing peptides.

Thermogravimetric analysis (TGA) is a great tool to quantify surface coverage and gain insight into thermal transitions of organic ligands bound to thermally stable metal oxide substrates. SiO₂ is stable at temperatures below 1600 °C so any weight loss can be attributed to surface bound water, thermal condensation events and ligand decomposition. Many amino acids adsorptions have been analyzed this way, and typically one peak is observed in the thermal condensation region (150 to 200 °C) if neighboring amino acids condense.^{13, 20-22} The thermodynamically and kinetically stable product is typically the cyclic dipeptide, diketopiperazine (DKP) form, and has been observed across many studies of amino acids on silica supports.^{2, 12, 21, 23} Both temperature and length of time play a role in directing polymerization, and longer oligomerization is observed after low temperature (~ 80-100 °C) repetitive thermal cycling.^{1, 24} Fuchida et al found that heating time as well as hydration level control the ratio of Gly dimer/cyclic dimer formation, and that the DKP product is preferred at longer heating times under anhydrous conditions.²⁵

In our previous work, first derivative thermograms (DTG) showed two peaks in the thermal condensation region, ~160 °C and ~200 °C of His adsorbed on FSN surfaces.²⁶ The second peak was present in His loading levels >0.05M and His·HCl loading levels >0.12M suggesting that the presence of salt deters the higher temperature reaction. The aim of the current work is to understand the progression of thermal activity and identify the peptide products formed after each step. If the

cyclization of His occurs through a two-step process, forming a linear dipeptide before DKP, this would be unique among other amino acids on silica surfaces and maybe explored further for oligomerization in origin of life research. We use a combination of TGA, high-performance liquid chromatography (HPLC), mass spectrometry (MS), solution nuclear magnetic resonance (NMR) spectroscopy, solid-state NMR (SSNMR), and density function theory (DFT) computation to elucidate the two discreet thermal events for His adsorbed on FSN and characterize the products produced.

Experimental

Materials

FSN (~ 7nm) with Brunauer, Emmett, and Teller (BET) surface area of 395 ± 25 m²/g, natural abundance L-histidine monohydrochloride monohydrate ($\geq 99.5\%$), and L-histidine ($\geq 99.5\%$) were purchased from Sigma-Aldrich. L-arginine ($\geq 98\%$), L-phenylalanine ($\geq 98.5\%$), L-lysine monohydrochloride ($\geq 99\%$), and L-glutamine (99%) were purchased from Fischer Scientific. All materials were used as received.

Sample preparation

His – FSN adsorption complexes were prepared as follows. FSN were heated at 500 °C for 15 hours to activate the silica and remove adsorbates from the surface. Aqueous solutions of His were created in 10.00 mL aliquots and adjusted to pH 4, 7.6, or 10 ± 0.2 using either 1M HCl or 1M NaOH as needed. 150 mg of FSN was added and the pH was retested and adjusted as needed. The solutions were mixed at room temperature for 3 hours. His – FSN adsorptions were separated by centrifugation and dried under vacuum at room temperature for 48 hours. All experiments were

carried out in millipore deionized (DI) water. The notation His/FSN- x M will be used, where x refers to the initial His concentration (in moles per liter) in the adsorption solution. The same adsorption procedure was used for Arg – FSN, Phe – FSN, Lys – FSN, and Gln – FSN and the pH was adjusted to the isoelectric point of each amino acid.

Thermal condensation

Thermal condensation of histidine was promoted by exposing His/FSN-0.03M samples to prolonged heating at various intervals (3, 6, 8, and 24-hr) at 160 °C. The resulting thermal condensation product was removed from the FSN surface by washing with DI water, sonicating, and centrifuging at 10,000 rpm for 1 hr. The supernatant was collected and dried under vacuum. The dried product was then prepared for solution NMR, HPLC, and MS. Two thermal condensation events in the range of 150 – 250 °C were present in higher concentrations of His/FSN adsorptions.²⁶ The products following each transition were isolated by an isothermal treatment at the peak temperature for 3 hr. The products were then removed from FSN by washing and dried under vacuum for subsequent analysis by NMR, HPLC, and MS. The same thermal treatment applied by TGA was also tested (ramped at 5 °C/min under N₂ (g) until the peak maximum temperature) and showed only subtle differences compared to isothermal treatment indicating the isothermal treatment is a good representation. Thermal cycling on His/FSN-0.03M was performed using a Bio Rad T100™ Thermal Cycler where one cycle consisted of 12-hr at 100 °C followed by 12-hr at 25 °C. Samples were washed, dried, and analyzed with solution NMR. Thermal cycling was performed under ambient conditions with humidity levels fluctuating between 40 – 60%.

Thermal gravimetric analysis

TGA of His/FSN-*x*M samples was performed with a TA Instruments Q50 under a steady nitrogen flow (60 mL/min for furnace and 40 mL/min for balance). Prior to analysis, the sample was kept under N₂ flow for 30 minutes to remove weakly-bound physisorbed water and obtain a stable baseline. A sample mass of 12 – 15 mg was used in each experiment and a heating rate of 5 °C/min was applied from 25 – 800 °C. DTG was applied to record peak temperatures of each thermal transition using TA Universal Analysis software.

High-performance liquid chromatography

Separation was performed using reverse-phase (RP) HPLC with a C₁₈ column (C₁₈ Restek 150 x 4.6 mm) on an Agilent 1100 binary pumping system with a UV variable wavelength detector set to 214 nm. The mobile phase consisted of water (%A) and acetonitrile (%B) with 0.1% trifluoroacetic acid. A simple isocratic method was used where 100% A was applied at a flow rate of 1 mL/min for 10 minutes. Each peak was collected over 10 fractions and used in MS analysis described below.

Mass spectrometry

The analyte solutions collected from HPLC were directly infused into an Agilent 6530 mass spectrometer with dual Agilent Jet Stream (AJS) electrospray ionization (ESI) operating in positive ion mode. The drying gas was maintained at 250 °C with a flow rate of 8 L/min and the sheath gas was maintained at 250 °C and 11 L/min. The ESI ion source was used with the following conditions: nebulizer at 35 psi, fragmentor at 175 V, and skimmer at 65 V. MS data were recorded

in full scan mode (m/z 100 to 3000) with internal standards from the Agilent G1969-85001 reference mass solution kit (m/z 121.1 and 922.0). Free His was run as calibration standard.

Solution NMR spectroscopy

Solution NMR experiments were performed with a 600 MHz Advance IIIHD Bruker spectrometer equipped with a 5 mm TXI probe operating in triple resonance ($^1\text{H}/^{13}\text{C}/^{15}\text{N}$) mode. All samples were dissolved in 90:10 $\text{H}_2\text{O}:\text{D}_2\text{O}$. ^1H and ^{13}C spectra were referenced to a 10% DSS internal standard (0 ppm) and ^{15}N spectra were externally referenced to nitromethane (380.6 ppm) in deuterated chloroform.²⁷ ^1H 1D spectra were collected using nuclear Overhauser effect (NOE) transfer with pre-saturation during the recycle delay and mixing time to suppress water signals (Bruker, noesypr1d or noesygppr1d), 8 – 64 scans, 2 – 5 sec d1, 65536 points, and 16 – 20 ppm spectral width. ^{15}N 1D spectra were extracted from the F_1 dimension of $^1\text{H} - ^{15}\text{N}$ heteronuclear multiple bond correlation (HMBC) experiments (Bruker, hmbcgpndqf) collected with 128 scans, 1.5 sec d1, 4096 points, 256 complex points, and 11 ppm / 300 ppm spectral width. ^1H total correlation spectroscopy (TOCSY) (Bruker, mlevphpr.2) was collected with 80 ms mixing time, 32 scans, 2 sec d1, 2048 points, 256 complex points, and 10 ppm spectral width in both dimensions.

Diffusion coefficients were calculated using the Stejskal – Tanner equation²⁸ for concentrations ranging from saturated stock solution diluted to 0.05 wt%. All samples were diluted in D_2O and equilibrated for a minimum of 15 minutes at 25 °C prior to data collection. Diffusion experiments were collected using a 15 ppm spectral width, 32 scans, and 5 sec d1 in a 2D stimulated echo experiment with bipolar gradients and WATERGATE suppression (Bruker, stebpgp1s19). Variable gradient strength was applied using 2 or 2.2 ms gradient pulse (δ), 180 ms

diffusion delay (Δ) and 32 points for each diffusion decay curve. Gradient strength was calibrated from the known self-diffusion coefficient of water at 25 °C ($2.29 \times 10^{-9} \text{ m}^2/\text{s}$).²⁹

Solid-state NMR spectroscopy

SSNMR experiments were performed with a 1.9 mm triple resonance ($^1\text{H}/^{13}\text{C}/^{15}\text{N}$) probe and Bruker Avance IIIHD 600 MHz spectrometer. 30 kHz magic angle spinning (MAS) was used. ^{13}C Cross polarization experiments (CP-MAS) were collected using a 2.45 μs hard pulse on ^1H , followed by a 2 ms ramped (30%) contact pulse on ^1H with a radio frequency (rf) field strength of 118 kHz. Polarization transfer to ^{13}C was matched to the -1 Hartman Hann condition and ^1H decoupling at 115 kHz rf was applied during acquisition (Bruker, swftppm_13). A 5 sec recycle delay (d1), 300 ppm sweep width, and 4k scans were used. Spectra were processed with 50 Hz exponential line broadening and indirectly referenced to adamantane (^{13}C , 38.48 ppm).³⁰ ^{15}N CP-MAS experiments were collected at 30 kHz MAS. An initial ^1H $\pi/2$ pulse of 2.4 μs was applied followed by a 1.5 ms ramped pulse (30%) contact pulse on ^1H with a rf field strength of 103 kHz. Polarization transfer to ^{15}N was matched to the -1 Hartman Hann condition and high power ^1H decoupling at 117 kHz rf was applied during acquisition (Bruker, swftppm_13). A 3 sec recycle delay, 400 ppm sweep width, and 4k scans were used. Spectra were processed with 100 Hz exponential line broadening and indirectly referenced to glycine (^{15}N , 31.6 ppm).³¹

Computational DFT chemical shift calculations

Computational analysis was executed with the Gaussian16 software package using density functional level of theory (DFT) with a B3LYP 6-31G+(d,p) basis set.³² Geometry was optimized on various His dipeptides solvated in water without constraints until energy minimization was

achieved. Neutral and protonated states were analyzed for cyclic His DKP and linear dipeptides. Chemical shielding tensors were calculated at the same level of theory using the gauge-including atomic orbital (GIAO) method³³ and converted to chemical shift using a reference molecule (TMS) optimized under the same conditions. The equation used for conversion of chemical shielding to chemical shifts is described previously.^{26, 34, 35}

Results

Confirmation of Histidine DKP

The thermal condensation reaction for His on FSN was investigated by TGA, solution NMR, HPLC and MS. While simple diurnal fluctuations provide enough energy for polymerization and are relevant to origin of life,^{1, 11, 25} the primary aim of this work is to understand the two thermal transitions that occur in the TGA thermal condensation region for His/FSN adsorption complexes and characterize the structure of the products produced. Short, isothermal treatments were applied at distinct thermal condensation peak temperatures to isolate each product. The first thermal condensation peak found by DTG was 163 °C thus, a temperature of 160 °C was used to facilitate thermal condensation and peptide bond formation.²⁶ Thermal condensation was induced for His/FSN adsorptions for various lengths of time (3, 6, 8, and 24 hr) and the resulting ¹H solution NMR spectra of the products are shown in **Figure 4.1**. No amine or amide peaks are observed in any of the spectra due to rapid proton exchange. Percent yield is expressed as total product converted from free His calculated by integration of the H_α peak areas of free His and His thermal condensation products. At short heating times (3 hr) multiple products are present in nearly equimolar ratios and 75% of free His is unreacted. As thermal treatment time increases to 24 hr,

92% of free His is converted into the product indicated by the asterisk (*). The minor peptide product indicated by the dagger (†) is unobservable after heating for 24 hr.

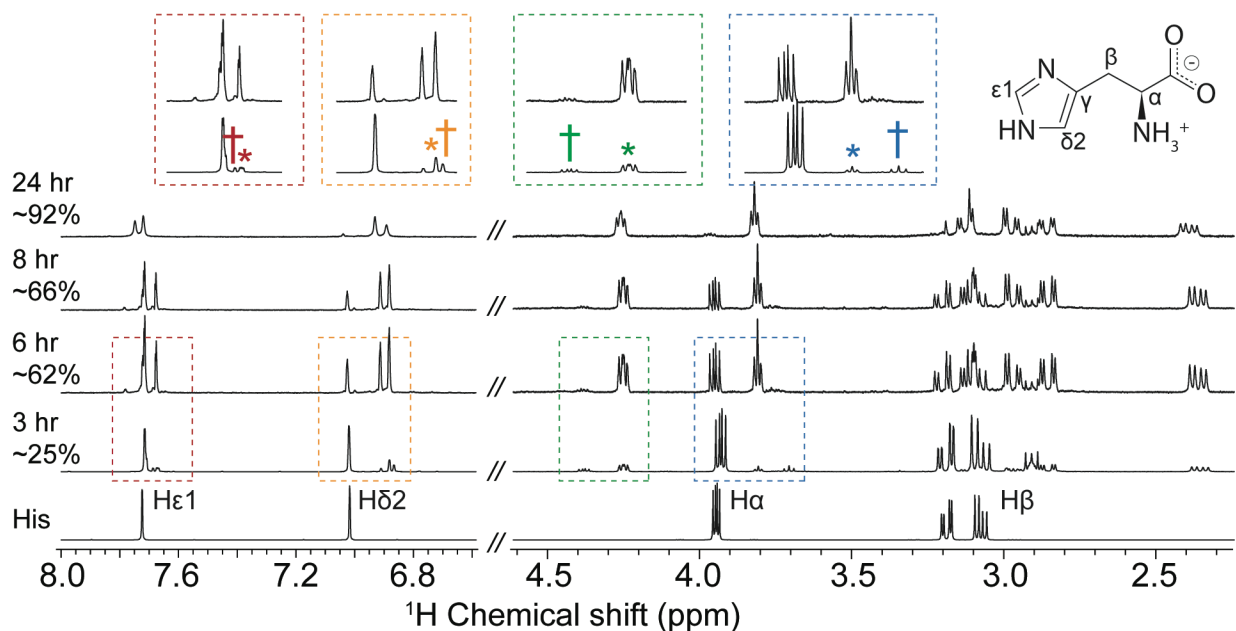


Figure 4.1. ^1H solution NMR of His/FSN thermal condensation products after $160\text{ }^\circ\text{C}$ heating at various times. Percent yield of total product was calculated by integration of H_α peak areas. DKP product is indicated with an asterisk (*) and an additional minor peptide product with a dagger (†).

^1H chemical shifts of the major (*) product in **Figure 4.1** agree with previously reported NMR data of His DKP in D_2O ³⁶ and are reported in **Table 4.1**. However, we observe two unique H_α resonances which integrate in a 1:1 ratio for the major product. Additional multi-dimensional NMR experiments were performed on the major (*) product isolated after $160\text{ }^\circ\text{C}/24\text{ hr}$ heating, including $^1\text{H} - ^{15}\text{N}$ HMBC (**Figure 4.S1**), $^1\text{H} - ^1\text{H}$ TOCSY (**Figure 4.2**), $^1\text{H} - ^{13}\text{C}$ HMBC, $^1\text{H} - ^{13}\text{C}$ HSQC, and $^1\text{H} - ^1\text{H}$ COSY (not reported). No ^{15}N correlations are observed in the amine region

of the $^1\text{H} - ^{15}\text{N}$ HMBC, supporting the proposed DKP structure. This confirms that the major (*) product has no free amine terminus, and thus must be a cyclic peptide.

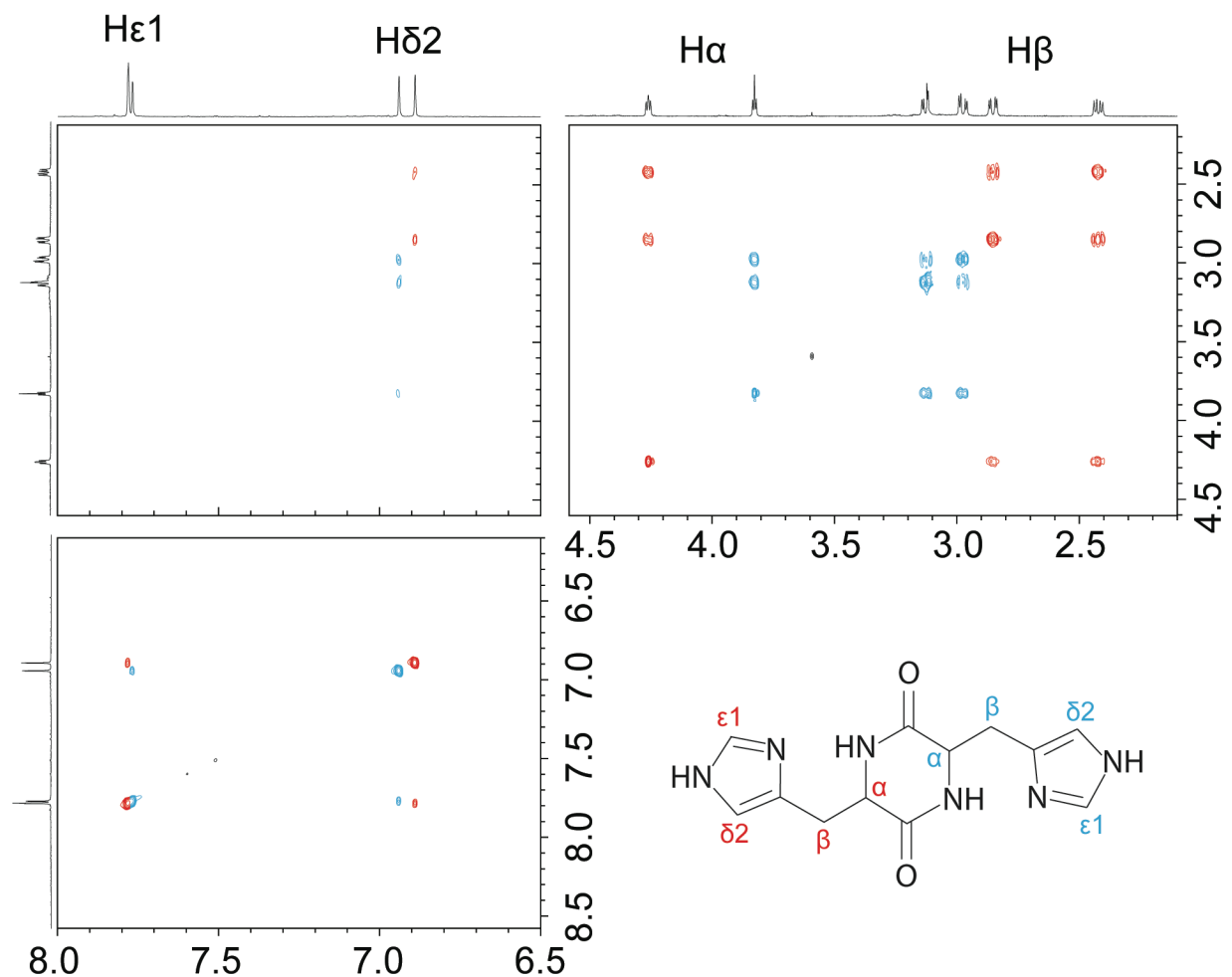


Figure 4.2. $^1\text{H} - ^1\text{H}$ TOCSY of His/FSN thermal condensation product after 24 hr thermal treatment at 160 °C.

$^1\text{H} - ^1\text{H}$ TOCSY reveals through-bond correlations of protons within a given spin system. A mixing time of 80 ms will display proton correlations up to 5-6 bonds apart and cannot cross

quaternary carbon sites. In **Figure 4.2**, two complete His spin systems are identified which indicate two non-equivalent His environments. Cross correlations are not observed between H_α resonances due to the quaternary C' sites in the central ring. It should be noted that H_α sites integrate proportionally, and correlation is observed between the two H_α sites in a through space 2D NOESY experiment with 1 sec mixing time (not reported), which confirms the two His environments are part of the same structure. His DKP model and proton environments are also displayed in **Figure 4.2**. DKP products are thermodynamically and kinetically favored at higher temperatures and have been observed in several studies following thermal condensation on silica surfaces, so it is not surprising that DKP is evidenced as the major (*) product in the first thermal event.^{2, 8, 12, 13, 24, 25, 37, 38} The minor (†) product observed in 160 °C/3 hr and 6 hr samples will be discussed in the sections below.

The product resulting from the second thermal event ~ 210 °C was isolated by heating His/FSN at 200 °C for 3 hr. **Figure 4.3** shows 1H spectra of free His, 160 °C/24 hr and 200 °C/3 hr which, surprisingly, are nearly identical. Both H_α proton environments of the major (*) product are present, integrate 1:1, and all the corresponding protons resonate at identical chemical shifts in both products. The peptide yield is significantly higher in the 200 °C treatment at short heating times with ~ 84% conversion, compared to only ~ 25% after 3 hr at 160 °C. This suggests that both thermal events produce DKP as the major product, however a much longer heating time is required to reach comparable DKP yield for the 160 °C treatment. Possible explanations for two discrete thermal events in the TGA are discussed further in the discussion section.

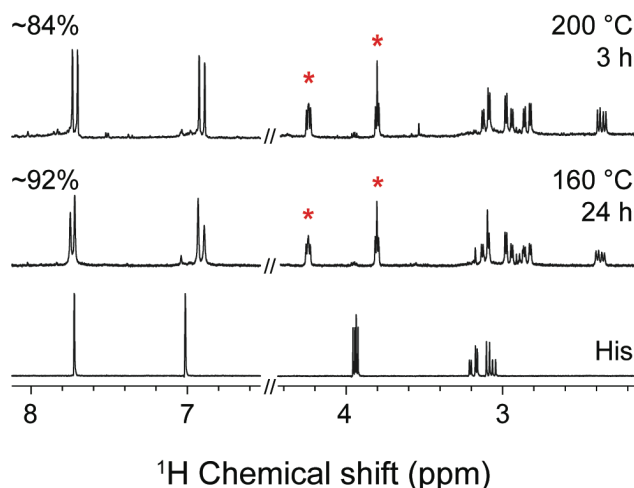


Figure 4.3. ^1H NMR of free His and thermal condensation products after isothermal treatment at 160 °C/24 hr and 200 °C/3 hr. Percent yield is displayed on the left calculated from $\text{H}\alpha$ peak areas. DKP product is indicated with an asterisk (*).

To further confirm His DKP as the major (*) product, HPLC, ^{13}C and ^{15}N CP-MAS SSNMR, MS, diffusion NMR, and DFT modeling were performed and support that DKP is the preferred product at both thermal condensation temperatures. **Figure 4.S2** shows RP-HPLC chromatograms and ^{13}C and ^{15}N CP-MAS which support ^1H solution NMR data and display partial conversion after 160 °C/3 hr, and a near complete conversion to His DKP after 200 °C/3 hr. All ^{13}C and ^{15}N sites in SSNMR spectra are significantly broadened due to the rigid environment that restricts local dynamics in the solid-state sample. It is also important to note that the spectra displayed in **Figure 4.S2 (top)** are all adsorbed on FSN and thus, not influenced by the washing step. C' and N_α sites exhibit the most obvious changes after thermal treatment since these sites participate in the formation of new bonds. ^{13}C and ^{15}N CP-MAS results of 160 °C/3 hr appear as a compilation of the top and bottom spectra, having populations of both unreacted His adsorbed and partial product conversion to DKP. Peptide bond formation is clearly evident by the formation

of the new amide peak in ^{15}N CP-MAS at ~ 120 ppm. After $200\text{ }^\circ\text{C}/3$ hr thermal treatment, C' and C_β sites have clear changes in chemical shifts, and the N_α in the free amine region almost completely disappears due to conversion to the peptide amide structure (~ 120 ppm).

Free His was analyzed with the HPLC method described above and elutes at 2.15 min. In **Figure 4.S2 (bottom)**, HPLC of the $160\text{ }^\circ\text{C}/3$ hr sample shows a large population of unreacted His plus an additional peak (2.45 min) of similar intensity. Two smaller peaks are present (2.28 and 2.65 min) which could indicate short linear peptides, but were not analyzed further because of convolution. Although not reported, the presence of salt seems to impact the abundance of the second peak at 2.28 min, with a higher concentration in the presence of NaCl. After $200\text{ }^\circ\text{C}/3$ hr, free His (2.15 min) is almost entirely depleted and one large peak is observed at the same retention time (2.45 min) as the $160\text{ }^\circ\text{C}/3$ hr sample. Three smaller peaks are observed at longer retention times (3.18, 3.68, and 4.55 min) which could be larger peptides. The supernatant was also analyzed by HPLC to confirm that the washing step does not impact polymerization. Based on the solution NMR results discussed above it is clear that the HPLC peak at retention time 2.45 min is the His DKP peptide.

The main product peak (2.45 min) was collected over 10 fractions and directly injected into MS-ESI (**Figure 4.S3**). The peak at 922 m/z is an internal reference and can be ignored. The base peak at 275.1 m/z can be attributed to either $[\text{DKP}]^+$ or cyclic $[\text{His}_4]^{2+}$. The parent peak at 549.1 m/z is consistent with a cyclic $[\text{His}_4]^+$ molecule and this cannot be ruled out as a possibility, since both compounds would be indistinguishable by NMR. Diffusion NMR experiments were performed to gain insight into the size of the cyclic compound and discount the presence of larger His DKP structures containing more than two His molecules.

Diffusion of free His and DKP (isolated from thermal treatment of 200 °C/3 hr) were measured at 5 different concentrations. We report the average diffusion coefficients calculated for free His and each spin system in His DKP ($\delta_{H\alpha}$ at 3.82 and 4.26 ppm). The average diffusion coefficient calculated for His across all concentrations was 5.9×10^{-10} (m²/s) consistent with the literature value of His measured under similar conditions.³⁹ The average diffusion coefficient calculated for each H _{α} in DKP under the same conditions was 4.8×10^{-10} (m²/s) and 4.7×10^{-10} (m²/s), respectively, which agree with a molecule considerably higher in molecular weight than free His. The difference between each DKP H _{α} site is within the margin of error (± 0.1), but is consistent across all concentrations.

Assuming a spherical molecule, the hydrodynamic radius calculated by the Stokes-Einstein equation using the diffusion coefficients stated above is 4.2 Å for His, and 5.1 Å and 5.2 Å, respectively, for each DKP H _{α} site. If the major product was cyclic [His₄]²⁺ a radius ~ 4x the size of His would be expected and therefore, this product is ruled out based on diffusion NMR. Diffusion NMR is incredibly sensitive and helps narrow down the most likely 3D His DKP conformer predicted from DFT modeling. Where ¹H has small chemical shift perturbations and multiple DFT structures have calculated chemical shifts that overlap, diffusion NMR helps narrow down the most likely 3D conformer for the His DKP product.

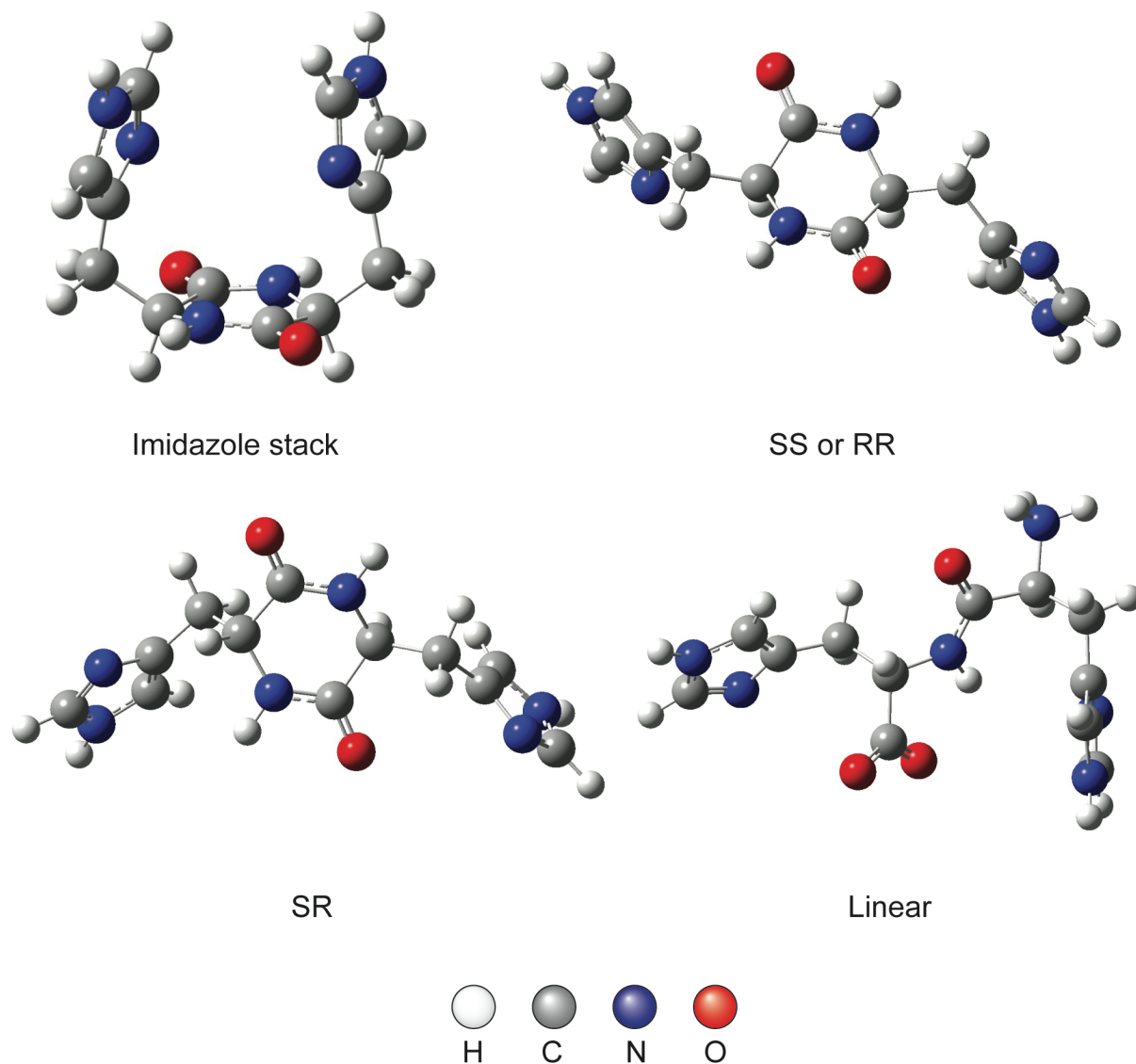


Figure 4.4. His DKP and linear conformations derived from DFT computational modeling.

DFT modeling was performed on various linear and cyclic dipeptide models solvated in water. The chemical shifts were calculated from the predicted shielding values and we report four possible conformations that are in good agreement with experimental data and low in total energy (**Table 4.1, Figure 4.4**). The “imidazole stack” DKP model exhibits pi-pi stacking of the imidazole

rings which is known to have stabilizing effects³⁸ and the predicted ¹H chemical shifts closely match some of our experimental results. However, both His molecules are equivalent in this model and yield identical chemical shifts, in contrast with the inequivalent two unique sets of resonance observed experimentally by solution NMR. The molecular radius of this structure is ~ 2.25 Å which is also inconsistent with the radius calculated from diffusion NMR and for these reasons, we discount this model as being the 3D orientation of the major (*) product. Based on the diffusion NMR hydrodynamic radius and experimental and calculated ¹H chemical shifts (**Table 4.1**) the most likely conformation is the SR conformer (**Figure 4.4**).

Table 4.1. ¹H solution NMR data of His DKP from literature, His DKP experimental after 160 °C/24 hr, and calculated chemical shifts predicted from DFT modeling. Conformers are shown in Fig. 4.4. Chemical shift is expressed in ppm relative to TMS at 0 ppm. Energy (E) after optimization is reported for the calculated compounds, and the hydrodynamic radius (R) of the molecules are shown.

	Site	δ_H (ppm) literature ³⁶	δ_H (ppm) experimental	δ_H (ppm) calculated imidazole stack	δ_H (ppm) calculated SS	δ_H (ppm) calculated SR	δ_{calc} (ppm) calculated linear
¹ H	H ϵ 1	7.70	7.72, 7.75	7.30	7.58, 7.69	7.74, 7.54	7.47, 7.77
	H δ 2	6.90	6.93, 6.89	7.14	7.15, 7.14	7.14, 7.18	7.22, 7.08
	H α	4.25	3.82, 4.26	4.22	4.53, 4.90	4.24, 4.54	3.76, 4.55
	H β	2.85, 2.35	[3.13, 2.98] [2.86, 2.39]	3.49, 2.65	[3.17, 2.79] [3.22, 2.57]	[3.13, 2.81] [3.12, 2.79]	[3.14, 2.37] [3.13, 2.99]
E (kJ/mol)			-2480533	-2480522	-2480532	-2681211	
R (Å)		5.07, 5.18	2.25	5.86	5.15	5.15	

Thermal Condensation at Lower Temperatures

DTG curves show two thermal events occurring ~ 163 °C and 210 °C using a constant ramp of 5 °C/min.²⁶ To make sure the 3 hr isothermal treatments were accurately representing the products produced after each thermal event, we replicated the temperature ramped conditions applied during TGA and analyzed the products with solution NMR. The adsorbed sample was purged under N₂(g) and heated with a controlled ramp of 5 °C/min to 160 °C or 200 °C. Once the desired temperature was reached, the oven was shut off and cooled to room temperature. The product was washed following the same procedure and ¹H solution NMR was collected. The most notable difference that occurs between the ramped and isothermal treatments is the total peptide yield, suggesting that the 3 hr isothermal treatment is satisfactory for final DKP product isolation. DKP (*) yield increases from $\sim 17\%$ in the isothermal treatment to $\sim 46\%$ in the ramped treatment to 160 °C and there is a small population of additional ¹H resonances (†) in the 160 °C/3 hr sample (**Figure 4.1, Figure 4.S5**) that is not present in the ramped treatment. Conversely, DKP yield is higher in the isothermal treatment at 200 °C compared to the ramped treatment, with no additional resonances, supporting that DKP is kinetically favored.

Various other thermal treatments were tested to explore formation of minor products (**Figure 4.5**). Although it appears no reaction took place, many populations are observable when the baseline is blown up significantly (500%). Interestingly, DKP (*) is not present in any of the lower temperature thermal treatments in **Figure 4.5**. Peaks ~ 4.0 and 3.8 ppm are the ¹J_{CH} coupling of free His H_α and should not be confused with DKP. All treatments were isothermal for the length of time indicated, except for 100 °C 2 cycles, where 1 cycle was programmed to heat at 100 °C for 12 hr then 25 °C for 12 hr. The 100 °C and 90 °C treatments have the most diversity among products with multiple resonances present, and the two treatments at 120 °C are nearly identical.

All 4 treatments contain evidence of the minor (\dagger) product that was observed in 160 °C/3 hr and 160 °C/6 hr samples (**Figure 4.1**). This product exists in low (less than 10%) yields in solution with other species and we have not been able to isolate and perform full structural analysis by NMR. However, the experimental H_α chemical shifts of the minor (\dagger) product at 3.75 and 4.39 ppm are in good agreement with the linear His dipeptide conformer predicted by DFT (**Table 4.1**, **Figure 4.3**) and with the predicted 1H solution NMR spectrum of histidylhistidine that shows 2 unique H_α resonances at 4.01 and 4.48 ppm with equivalent shifts for the other resonances.⁴⁰

Evidence of His linear peptides are also present in the MS fragmentation patterns after 160 °C/3 hr heating. $[His_3]^+$ was observed at 430.2, and 10 repeat losses of -135 m/z was observed in one of the minor peaks on HPLC, suggesting we have a longer His peptide species. This could be responsible for the other smaller peaks in the HPLC eluting ~ 3 -5 min (**Figure 4.S2**). This would be extremely interesting in origin of life research because it would overcome the thermodynamically and kinetically preferred DKP formation which is seen in the polymerization of many other amino acids on oxide surfaces and suggest lower temperature treatments as routes to linear polymerization.

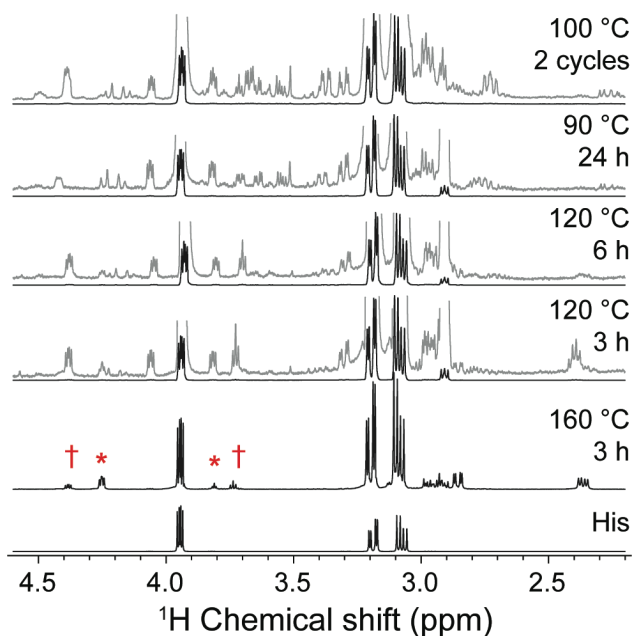


Figure 4.5. ^1H solution NMR of free His and His/FSN products after various thermal treatments. Grey traces are scaled 500% to display weak resonances. DKP peaks are indicated by the asterisk (*) and the minor peptide product peaks are indicated by the dagger (†).

The Effect of Molecular Organization on Thermal Condensation

In previous work, we established that a water layer exists at the interface between FSN and amino acids after adsorption.^{22, 26} While removing water through drying did not affect binding orientation of His molecules around the surface, it did promote tighter binding interactions.²⁶ To determine if the water layer was influencing the thermal condensation reactions, TGA was performed on His/FSN adsorptions in “dry” conditions where the interfacial water layer was removed prior to TGA temperature ramping by pre-heating the sample under $\text{N}_2(\text{g})$ for 5 hr at 100 °C. Two loading levels were analyzed: 0.05M roughly corresponding to a single saturated His surface layer and 0.10M to ensure both thermal events would be clearly observable. The results are shown in **Figure 4.6** and both thermal events in the thermal condensation region are still

present after water is removed. The peak temperatures and peak intensities remain the same upon drying, suggesting that the interfacial water layer has little effect on oligomerization. The formation of an additional peak in the degradation region >300 °C is observed and will not be discussed further.

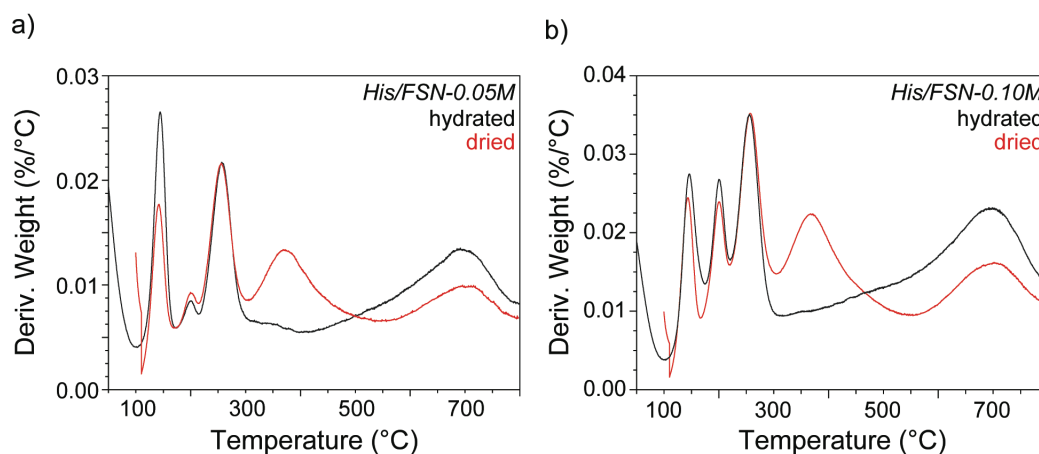


Figure 4.6. DTG of His/FSN at pH 7.6 in hydrated and dried conditions adsorbed at (a) 0.05M and (b) 0.10M His concentrations.

His/FSN adsorptions at pH 4 and pH 10 were analyzed with TGA to investigate the effect of molecular orientation, which is influenced by pH, on oligomerization. In acidic conditions, His molecules experience charge-charge repulsion and are highly dynamic within the water layer at the surface with no preferred binding orientation.²⁶ In contrast, zwitterionic His molecules pack horizontally around the surface with at least two contact points: $N_{\epsilon 2}$ and $N_{\alpha}H_3^+$ or COO^- . If molecular arrangement is the cause of the second thermal event, then only one peak should appear in His/FSN adsorptions at pH 4 where His molecules are randomly arranged. **Figure 4.7** shows

His/FSN adsorptions at pH 4, pH 7.6, and pH 10 at low, mid, and high concentrations. The peaks in pH 4 adsorptions are significantly broadened which is consistent with a distribution of molecular arrangements on the surface causing thermal events to occur over a broad range of temperatures. It is possible that the second thermal event ~ 200 °C is buried under line broadening, but only one major thermal event clearly occurs in the thermal condensation temperature range for pH 4. A small peak ~ 110 °C forms in pH 4 adsorptions and we attribute this to water or salt associated water.

At pH 10, $\text{N}_\alpha\text{H}_3^+$ becomes deprotonated and His molecules have a net negative charge. This protonation state of His largely impacts the binding arrangement, so it is likely that the assembly of His/FSN at pH 10 is different than the other lower pH conditions. The molecular arrangement of His/FSN at pH 10 has not been completely characterized, but ^{13}C and ^{15}N CP-MAS (not shown) display obvious differences in protonation state and assembly compared to pH 4 and pH 7.6. Similarly, the DTG curves look very different from pH 4 and pH 7.6, and only one clear peak is observed in the thermal condensation region for the lower pH. This indicates that pH, which impacts His molecular binding and orientation on the surface could be the cause of the two thermal condensation events.

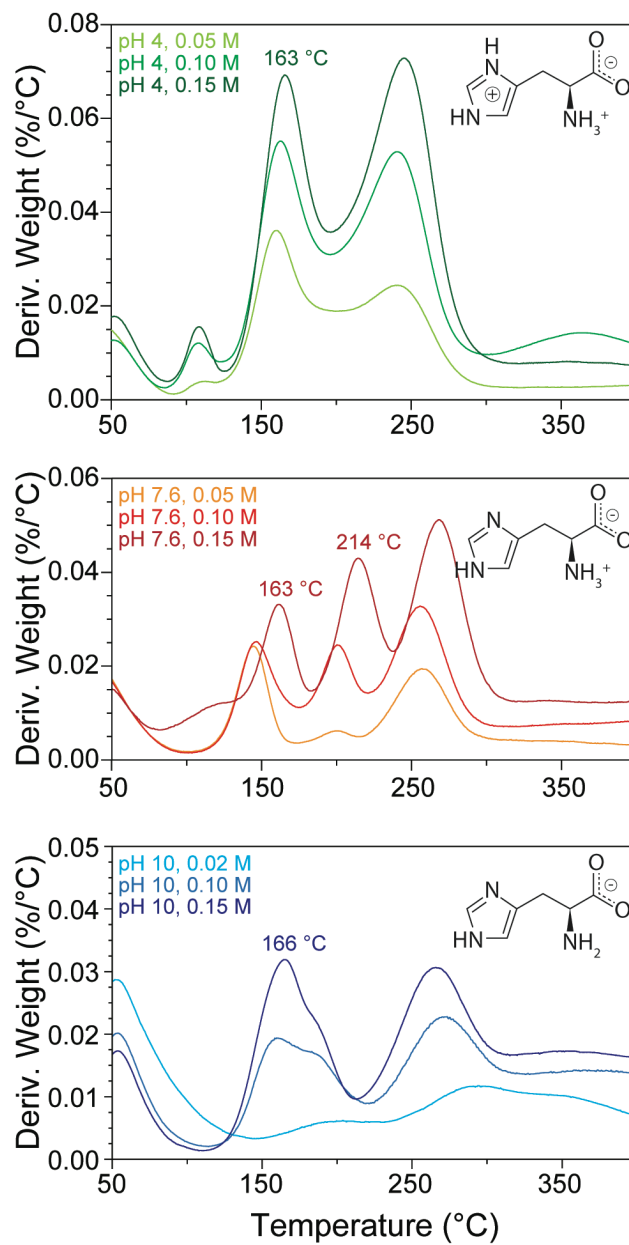


Figure 4.7. DTG of His/FSN adsorptions at pH 4, pH 7.6, and pH 10 as a function of His loading.

Discussion

TGA was performed previously to characterize the transition temperatures of each thermal event.²⁶ Both HisHCl (adjusted to ~ pH 7.6) and His were used as starting materials and adsorbed on FSN in concentrations ranging from 0.01M to 0.15M. The peak temperatures were independent of concentration. Only the first peak ~ 160 °C was shifted by the presence of salt to ~ 170 °C. The second peak ~ 210 °C readily formed in His adsorptions above 0.05M but did not form in HisHCl adsorptions until concentrations above 0.12M, well past surface saturation. This suggests salt plays a role in polymerization, likely by providing charge balance at the termini and/or sidechain^{41, 42} stabilizing His molecules as evidenced by the shift to higher temperature in the first thermal event and absence of the second thermal event at low concentrations. We also analyzed the impact of water at the interface (**Figure 4.6**) and found it to have no effect on oligomerization.

Several different thermal treatments were investigated. HPLC, solution, and SSNMR data all point to one major product (His DKP) that forms at two distinct temperatures. After 160 °C/3 hr we have partial conversion with unreacted His remaining. This is clear in the HPLC chromatograms (His at 2.15 min, product at 2.45 min) and ¹⁵N CP-MAS NMR (His free amine at 45 ppm, product amide at 120 ppm). MS, 2D solution NMR, and diffusion NMR confirm this product is His DKP. In His/FSN-0.03M adsorptions which correspond to roughly a single monolayer, only ~ 25% His reacts after 160 °C/3 hr while, >80% His reacts after 200 °C/3 hr. Interestingly, the ramped treatments have similar DKP peptide yields of ~ 46% (ramped to 160 °C) and 66% (ramped to 200 °C). At a ramp rate of 5 °C/min, the peak temperatures were reached after 27 and 35 min, respectively, supporting that DKP is the kinetically favored product.

The His DKP product here produces two sets of proton resonances for one product, which shows that the two His molecules in DKP are not chemically equivalent. Two spin systems are

identified in $^1\text{H} - ^1\text{H}$ TOCSY which correspond to each His molecule in one DKP molecule. They have slightly different diffusion coefficients that are right on the order of measurement error, which could be due to small differences in local His dynamics (e.g. one ring is more dynamic). The hydrodynamic radius of our DKP product calculated by diffusion NMR is between 5.1 and 5.2 Å. Four possible conformers predicted by DFT modeling were found to be in good agreement with ^1H experimental NMR chemical shift data (**Figure 4.4**). The calculated molecular radius from diffusion NMR allowed us to pinpoint the most likely His DKP conformer and we propose the SR model to be the most likely conformer because the difference in H_α chemical shifts is similar to our experimental H_α resonances, and the molecular radius is measured at 5.15 Å, in line with the calculated experimental diffusion value. This demonstrates the power of diffusion NMR when determining molecular structure.

The 3 hr isothermal treatment at 160 °C contains a minor (\dagger) product in low concentration that is not observed in the ramped thermal treatment. It is possible that there is a different, thermodynamically favored product that forms at lower temperature, longer thermal treatment times. This minor product is observed in all isothermal and thermal cycling treatments below 160 °C (**Figure 4.5**). The highest yield of the minor product of the conditions tested was ~ 10% after 160 °C/3 hr and was too low for full characterization, but H_α chemical shifts are in good agreement with our optimized DFT model for the linear His dipeptide (**Table 4.1, Figure 4.4**). Evidence of longer linear His peptides is found in MS data but were too low in abundance for a full NMR characterization. Nonetheless, it is clear that although DKP is the favored peptide formed, linear peptides are also present at low abundance and the overall abundance could be increased by conducting isothermal or cycled heating experiments at lower temperatures and is the subject of future investigations.

In the context of chemical evolution and the origin of life on Earth, all thermal conditions tested in our lab are considerably fast and short. This study would benefit from longer thermal cycling treatments at low temperatures ranging from a few weeks to a few months. Histidine and His dipeptides are capable of promoting the oligomerization of other amino acids and nucleic acids, and could have played an important role in early self-replicating chemical systems.^{15-17, 19} Here, we have demonstrated a novel route to generate these catalytic molecules which could be considerably important in origin of life research and that they could be present under plausible prebiotic conditions in the presence of a mineral catalyst like silica.

This study and others have shown that ligand assembly and binding on oxide surfaces largely impacts the polymerization process. Ala and Gly have been studied in detail because they are the simplest amino acids and are prebiotically prevalent.^{9, 10} They bind to mineral oxide surfaces through one contact point and quickly cyclize upon thermal treatment.^{8, 11, 12, 25} Lys binds FSN through the side chain amine group, vertically orienting outwards from the surface.⁴³ We investigated the thermal condensation of Lys/FSN and found that neighboring Lys molecules condense through the backbone, which encapsulates FSN and prevents removal by simple washing (data unpublished). We analyzed the decomposition of several other prebiotic amino acids on FSN and observe the following generalities. Amino acids with hydrophobic side chains (Ala, Val, Leu, Phe, Pro, Gly) likely adsorb through hydrogen bonding from N_{α} to SiO^{-} . A single thermal event is observed in the thermal condensation region, almost certainly DKP formation, similar to previous studies. Interactions between the negatively charged SiO^{-} surface and amino acids with negatively charged side chains (Glu, Asp) are likely unfavorable and their DTG thermograms are markedly different (**Figure 4.8**). Further characterization is needed to determine if thermal condensation reactions took place. R-groups containing OH (Ser, Thr) do not undergo thermal condensation

reactions and appear to degrade in a single, low temperature event. R-groups containing basic sidechains (Arg, His, Lys) have convoluted, broad peaks which we propose is due to multiple binding sites that occur at the backbone and sidechain environments that can also be dependent on the pH of the adsorption solution where two distinct thermal condensation events are observed at neutral pH (**Figure 4.7**). This has been demonstrated for His on FSN and TiO₂.^{26, 44} As we saw with His, the protonation state of these amino acids will likely direct binding orientation and ultimately polymerization. An in-depth analysis of amino acid thermal transitions on FSN in additional protonation states is recommended as a follow up investigation.

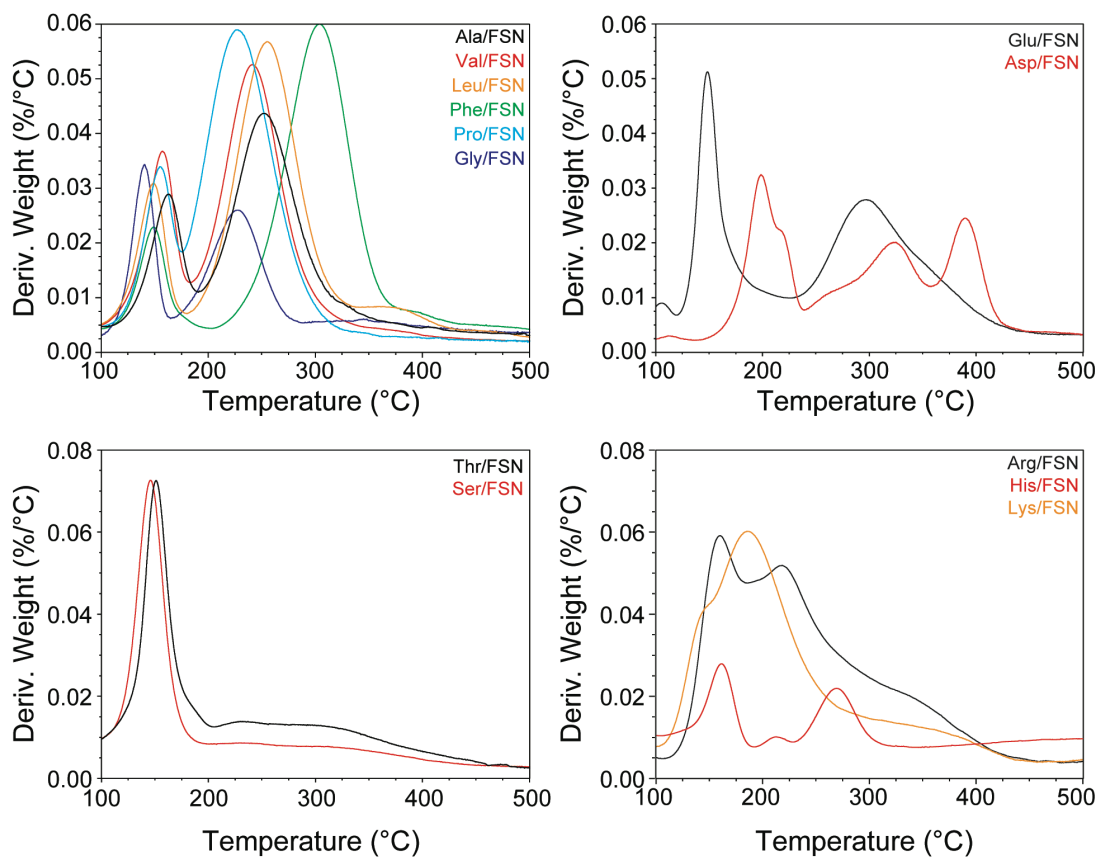


Figure 4.8. DTG curves of various amino acids adsorbed on FSN at 0.05M.

DTG results shown in **Figure 4.8** are consistent with the idea that molecular arrangement plays a large role in directing thermal condensation and polymerization events. In zwitterionic form, His molecules arrange horizontally along the surface and bind through terminal and sidechain contact points ($N_{\epsilon 2}$ and $N_{\alpha}H_3^+$ or COO^-).²⁶ At pH 7.6 where binding occurs through the side chain as well as the termini, two thermal events in the thermal condensation region are observed. In protonated form, His molecules experience charge-charge repulsion and are highly dynamic in the adsorbed layer with no preferred binding orientation. This isotropic distribution leads to broad lines in the DTG curves due to heterogeneity and dynamics at the surface, and only the thermal event at 160 °C is present. His/FSN adsorptions at pH 10 have not been characterized to the full extent as pH 4 and pH 7.6, but new resonances appear in ^{13}C and ^{15}N CP-MAS (not shown) which is attributed to differences in molecular assembly. The amine group is no longer protonated at pH 10 so it is reasonable to assume that altering the protonation state especially at one of the contact points would influence His arrangement at the interface. As a result, the DTG thermograms at pH 10 show similarities to pH 4 adsorptions, with broad, convoluted peaks. One thermal event is clear at ~ 160 °C and a second, higher temperature thermal condensation event is possible but unclear.

Finally, possible explanations are presented for the occurrence of discrete thermal events in His/FSN adsorptions at pH 7.6. After the first round of DKP formation at 160 °C, it is suggested that some sort of molecular rearrangement must occur. As more binding sites become available, nearby His molecules can anchor and react causing the formation of the second DKP peak at 200 °C. This would explain why the secondary peak ~ 200 °C is only observed at higher His concentrations, where His is packed in multiple layers on the surface. Alternatively, the two events could be caused by His anchoring through different contact points. Evidence of His/FSN

interactions are present in both $N_{\alpha}H_3^+$ and COO^- groups, but it is spatially improbable for both to be anchoring in the same molecule. Perhaps the event at 160 °C is due to His/FSN anchoring through the carboxyl terminus, and a higher temperature is required for His/FSN anchoring through $N_{\alpha}H_3^+$ where hydrogen bonding is stronger and the thermal condensation reaction takes place. Another possibility that is consistent with observing only 1 event in HisHCl/FSN adsorptions where salt is available for charge balancing, is that maybe some His molecules bind through only 1 contact point. Salt is available to stabilize the other terminus or side chain. Only molecules bound through the $N_{\alpha}H_3^+$ terminus are primed for DKP formation. If His is bound through the side chain only, rearrangement needs to occur for His to anchor through a terminal group before DKP formation can occur.

DKP formation has been observed in many amino acid/mineral oxide systems after thermal treatment. DKP is thermodynamically and kinetically favored and readily forms after just a few hours in some systems. While it is unsurprising that DKP is the major product in our study, it is unique that DKP forms at two different temperatures indicating the importance of multiple types of binding. This is likely due to the presence of multiple contact points in zwitterionic His molecules, where binding to the FSN surface can exist in multiple arrangements. In our previous study, SSNMR displayed clear evidence of His binding to FSN through $N_{\epsilon 2}$, $N_{\alpha}H_3^+$, and/or COO^- , but it is unclear how many contact points exist within a single His molecule.²⁶ Thermal energy may be required for some molecules to undergo rearrangement before DKP formation can occur. This is consistent with our observation of peptide yields ~ 50% in ramped thermal treatments (**Figure 4.S5**) where exposure to a range of temperatures may facilitate rearrangement during temperature ramping. Peptide yields were considerably different from one another (25% and 80%) in the isothermal treatments at 160 °C and 200 °C, respectively. The duration of thermal treatment

at 160 °C was considerably longer in the isothermal versus ramped treatment, but the peptide yield was lower suggesting that molecular rearrangement is influenced by temperature and that polymerization is highly dependent on molecular assembly.

Evidence of other peptide products, possibly linear derivatives, are observed when lower temperature conditions are applied and should be explored further. Together, the results presented here suggest that the protonation state of His is the main factor in molecular assembly at the surface of FSN, and molecular assembly at the interface largely directs the progression of thermally-activated oligomerization. This is further supported by our study of other amino acid/FSN systems (**Figure 4.8**), where amino acids with similar R-groups display similar thermal behavior. Hydrophobic residues with one possible contact site display one clear event in the thermal condensation region. R-groups containing an amine bind well and possibly have multiple contact points. R-groups containing carboxylic acid or alcohol moieties are unfavorable. We also draw the conclusion that amino acids with a net positive or net negative charge (**Figure 4.7, Figure 4.8**) have broad thermal transitions likely due to the high degree of surface dynamics.

Conclusions

The thermal behavior of His/FSN was investigated by TGA, NMR, HPLC, MS, and DFT computational methods. His has multiple contact points available for hydrogen bonding to the FSN surface at neutral pH and uniquely displays two discrete TGA events in the peptide condensation region when adsorbed in zwitterionic form, centered at 163 and 210 °C. Only one thermal event is observed when His is adsorbed in other protonation states, which display the intrinsic relationship between binding orientation and polymerization mechanism. Interestingly, DKP is produced at both thermal events, likely in an SR conformation, and forms with ~ 44% and 64% yields,

respectively, in conditions set forth by TGA. DKP yield increases to ~ 92% and > 80% after 160 °C/24 hr and 200 °C/3 hr, respectively. We previously proposed that His molecules bind to FSN through a combination of contact points ($N_{\epsilon 2}$, $N_{\alpha}H_3^+$, and/or COO^-) at neutral pH and based on the current results, rearrangement to a preferred anchor point might be necessary for complete DKP formation. This would describe the need for two discrete thermal events producing the same product.

An additional product is observed at 160 °C/3 hr and all low temperature thermal treatments which agrees with the linear His-His dipeptide as judged by 1H solution NMR in combination with DFT chemical shift calculations. This is extremely interesting in origin of life research as His uniquely demonstrates the ability to overcome the kinetically and thermodynamically favored DKP formation which is observed in most amino acid high temperature thermal condensation reactions on metal oxide surfaces. The His dipeptide may have also served as an early catalyst in polymerization of other amino acids in prebiotic conditions, and here we present a plausible route to synthesize His-His linear peptides using only heat. Additional studies are recommended to investigate thermal condensation reactions of His with other amino acids. Combining the catalytic properties of His and FSN with other amino acids may prove highly informative in origin of life research or provide a novel, inexpensive route to synthesis of His polypeptides which have many biological and metabolic functions.¹⁵ This work on His and other amino acids demonstrates that both the R-group and protonation state greatly influence molecular assembly on the surface of FSN, which ultimately influences polymerization. We also demonstrate the power of multi-dimensional solution, diffusion, and solid-state NMR techniques in combination with DFT chemical shift calculations to investigate the oligomerization of amino

acids at the interface of oxide surfaces and provide atomic level detail of their 3D structural conformers.

Acknowledgments

The authors would like to thank Dr. J. Bennett Addison and Dr. David Onofrei for help with NMR instrumentation, student training, and scientific discussion, and Dr. Greg Elliot for help with MS instrumentation. Haley L. Swanson would like to acknowledge support from NASA Fellowship 80NSSC19K0064.

Chapter 4, in full, has been submitted for publication of the material as it may appear in ACS Earth and Space Chemistry 2022. The dissertation author Haley L. Swanson was the primary investigator and author of this material. Supporting authors include Elizabeth A. Couri, Christian James P. Sabando, and Gregory P. Holland.

Supplemental Information

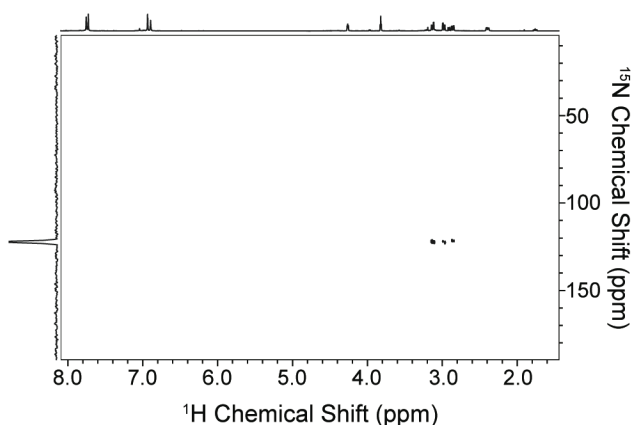


Figure 4.S1. ^1H – ^{15}N HMBC solution NMR spectrum of the His DKP thermal condensation product after 160 °C/24 hr heating on FSN. The absence of peaks in the amine region (40-50 ppm) confirms this product has no free amines and is thus the DKP form.

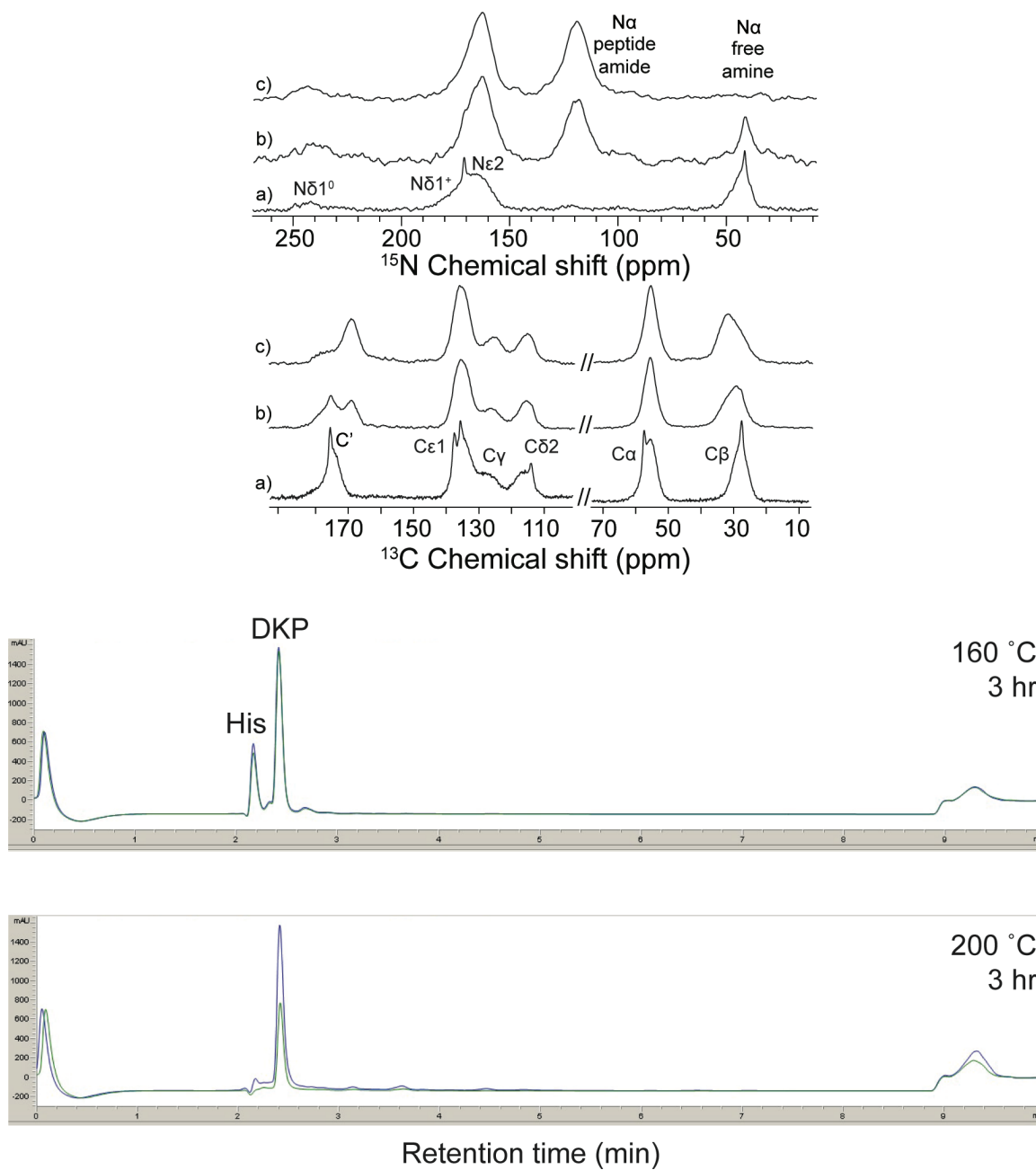


Figure 4.S2. (top) ^{13}C and ^{15}N CP-MAS SSNMR spectra of (a) His/FSN adsorption complexes in a dried state, (b) His/FSN after 160 °C/3 hr, and (c) His/FSN after 200 °C/3 hr. The protonation state of N δ 1 is indicated by the superscript. (bottom) HPLC of products after 160 °C/3 hr and 200 °C/3 hr thermal treatments. Green traces are the peptide supernatant, blue traces are dried and rehydrated.

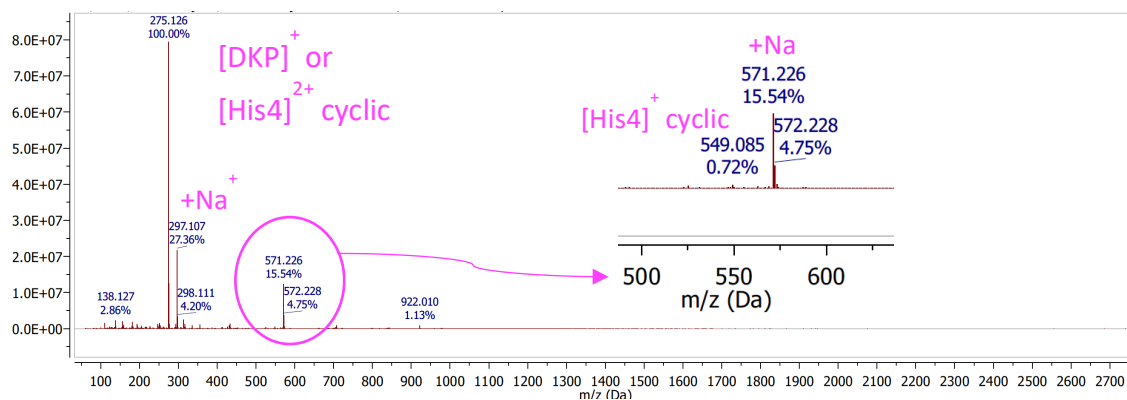


Figure 4.S3. MS-ESI Direct injection of the DKP fraction collected from HPLC after 160 °C/24 hr thermal treatment.

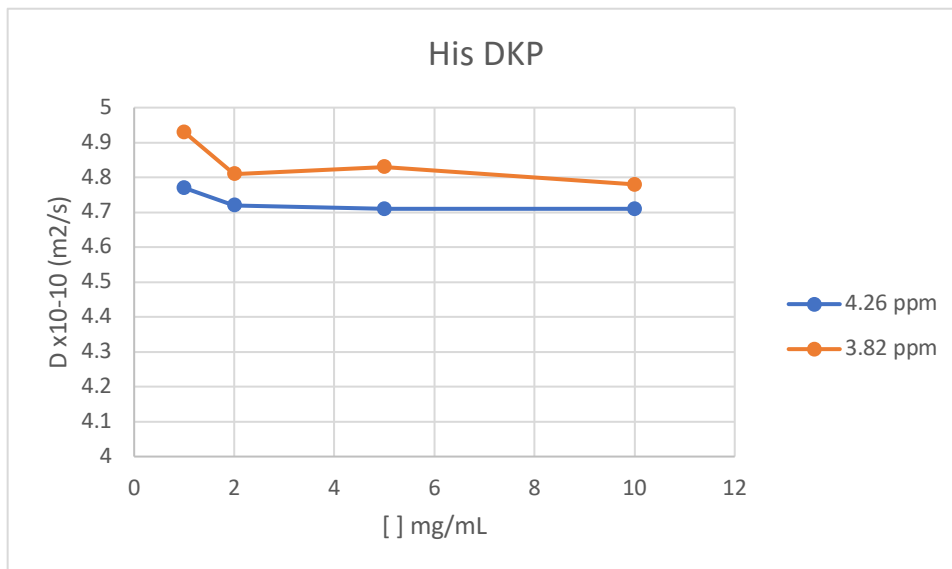
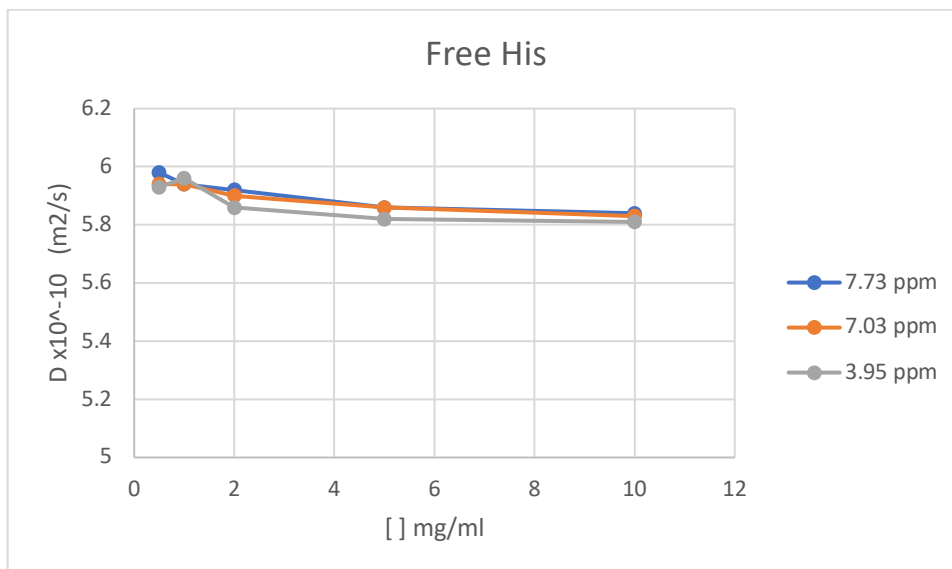


Figure 4.S4. Diffusion coefficients calculated from ¹H diffusion NMR experiments vs concentration.

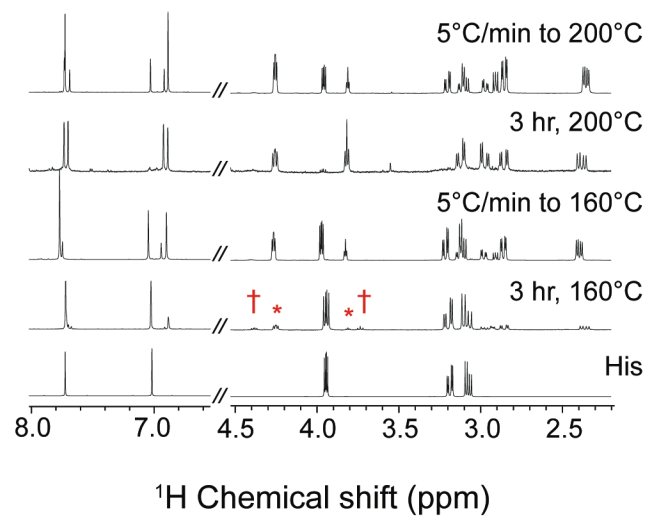


Figure 4.S5. ¹H solution NMR spectra of isothermal vs ramped thermal treatments on His/FSN-0.05M adsorptions. DKP peaks are indicated by the asterisk (*) and the additional His-His dipeptide product peaks are indicated by the dagger (†).

References

1. Lahav, N.; White, D.; Chang, S., Peptide formation in the prebiotic era: thermal condensation of glycine in fluctuating clay environments. *Science* **1978**, *201* (4350), 67-9.
2. Bujdak, J.; Rode, B. M., The Effect of Smectite Composition on the Catalysis of Peptide Bond Formation. *J Mol Evol* **1996**, *43* (4), 326-33.
3. Kuhlmann, A. M., The Second Most Abundant Element in the Earth's Crust. *JOM* **1963**, *15* (7), 502-505.
4. Pizzarello, S.; Huang, Y., The deuterium enrichment of individual amino acids in carbonaceous meteorites: A case for the presolar distribution of biomolecule precursors. *Geochim Cosmochim Acta* **2005**, *69* (3), 599-605.
5. Pizzarello, S.; Shock, E., The organic composition of carbonaceous meteorites: the evolutionary story ahead of biochemistry. *Cold Spring Harb Perspect Biol* **2010**, *2* (3), a002105.
6. Pizzarello, S.; Cronin, J. R., Alanine enantiomers in the Murchison meteorite. *Nature* **1998**, *394* (6690), 236.
7. Pizzarello, S., The Chemistry of Life's Origin: a Carbonaceous Meteorite Perspective. *Acc Chem Res* **2006**, *39* (4), 231-7.
8. Lambert, J. F.; Jaber, M.; Georgelin, T.; Stievano, L., A comparative study of the catalysis of peptide bond formation by oxide surfaces. *Phys Chem Chem Phys* **2013**, *15* (32), 13371-80.
9. Miller, S. L.; Urey, H. C., Organic compound synthesis on the primitive earth. *Science* **1959**, *130* (3370), 245-51.
10. Trifonov, E. N., The triplet code from first principles. *J Biomol Struct Dyn* **2004**, *22* (1), 1-11.
11. Forsythe, J. G.; Yu, S. S.; Mamajanov, I.; Grover, M. A.; Krishnamurthy, R.; Fernandez, F. M.; Hud, N. V., Ester-Mediated Amide Bond Formation Driven by Wet-Dry Cycles: A Possible Path to Polypeptides on the Prebiotic Earth. *Angew Chem Int Ed* **2015**, *54* (34), 9871-5.
12. Guo, C.; Jordan, J. S.; Yarger, J. L.; Holland, G. P., Highly Efficient Fumed Silica Nanoparticles for Peptide Bond Formation: Converting Alanine to Alanine Anhydride. *ACS Appl Mater Interfaces* **2017**, *9* (20), 17653-17661.
13. Bouchoucha, M.; Jaber, M.; Onfroy, T.; Lambert, J.-F.; Xue, B., Glutamic Acid Adsorption and Transformations on Silica. *J Phys Chem C* **2011**, *115* (44), 21813-21825.

14. Sakhno, Y.; Battistella, A.; Mezzetti, A.; Jaber, M.; Georgelin, T.; Michot, L.; Lambert, J. F., One Step up the Ladder of Prebiotic Complexity: Formation of Nonrandom Linear Polypeptides from Binary Systems of Amino Acids on Silica. *Chemistry* **2019**, *25* (5), 1275-1285.
15. Fitz, D.; Jakschitz, T.; Rode, B. M., The catalytic effect of L- and D-histidine on alanine and lysine peptide formation. *J Inorg Biochem* **2008**, *102* (12), 2097-102.
16. Shen, C.; Lazcano, A.; Oró, J., The Enhancement Activities of Histidyl-Histidine in Some Prebiotic Reactions. *J Mol Evol* **1990**, *31*, 445-452.
17. White, D. H.; Erickson, J. C., Catalysis of peptide bond formation by histidyl-histidine in a fluctuating clay environment. *J Mol Evol* **1980**, *16* (3-4), 279-90.
18. Shen, C.; Mills, T.; Oro, J., Prebiotic synthesis of histidyl-histidine. *J Mol Evol* **1990**, *31* (3), 175-9.
19. White, D. H., Theory for the origin of a self-reproducing chemical system by natural selection from short, random oligomers. *Origin of Life* **1981**, 399-404.
20. Stievano, L.; Piao, L. Y.; Lopes, I.; Meng, M.; Costa, D.; Lambert, J. F., Glycine and lysine adsorption and reactivity on the surface of amorphous silica. *Eur J Mineral* **2007**, *19* (3), 321-331.
21. Lambert, J.-F.; Stievano, L.; Lopes, I.; Gharsallah, M.; Piao, L., The fate of amino acids adsorbed on mineral matter. *Planet Space Sci* **2009**, *57* (4), 460-467.
22. Guo, C.; Holland, G. P., Alanine Adsorption and Thermal Condensation at the Interface of Fumed Silica Nanoparticles: A Solid-State NMR Investigation. *J Phys Chem C* **2015**, *119* (45), 25663-25672.
23. Basiuk, V. A., Condensation of vaporous amino acids in the presence of silica. Formation of bi- and tricyclic amidines. *Orig Life Evol Biosph* **1992**, *22* (6), 333-48.
24. Bujdak, J., The effect of reaction conditions on montmorillonite-catalysed peptide formation. *Catal Lett* **1996**, *37*, 267-272.
25. Fuchida, S.; Masuda, H.; Shinoda, K., Peptide formation mechanism on montmorillonite under thermal conditions. *Orig Life Evol Biosph* **2014**, *44* (1), 13-28.
26. Swanson, H. L.; Guo, C.; Cao, M.; Addison, J. B.; Holland, G. P., Probing the binding modes and dynamics of histidine on fumed silica surfaces by solid-state NMR. *Phys Chem Chem Phys* **2020**, *22* (36), 20349-20361.
27. Bertani, P.; Raya, J.; Bechinger, B., ¹⁵N chemical shift referencing in solid state NMR. *Solid State Nucl Mag* **2014**, *61-62*, 15-8.

28. Sinnaeve, D., The Stejskal-Tanner equation generalized for any gradient shape-an overview of most pulse sequences measuring free diffusion. *Concepts Magn Reson A* **2012**, *40A* (2), 39-65.
29. Mills, R., Self-Diffusion in Normal and Heavy Water in the Range 1-45. *J Phys Chem* **1973**, *77* (5), 685-688.
30. Morcombe, C. R.; Zilm, K. W., Chemical shift referencing in MAS solid state NMR. *J Magn Reson* **2003**, *162* (2), 479-86.
31. Hayashi, S.; Hayamizu, K., Chemical Shift Standards in High-Resolution Solid-State NMR (2) ¹⁵N Nuclei. *Bull Chem Soc Jpn* **1991**, *64* (2), 688-690.
32. Stephens, P. J.; Devlin, F. J.; Chabalowski, C. F.; Frisch, M. J., Ab Initio Calculation of Vibrational Absorption and Circular Dichroism Spectra Using Density Functional Force Fields. *J Phys Chem* **1994**, *98* (45), 11623-11627.
33. Wolinski, K.; Hinton, J. F.; Pulay, P., Efficient implementation of the gauge-independent atomic orbital method for NMR chemical shift calculations. *J Am Chem Soc* **2002**, *112* (23), 8251-8260.
34. Gervais, C.; Dupree, R.; Pike, K. J.; Bonhomme, C.; Profeta, M.; Pickard, C. J.; Mauri, F., Combined first-principles computational and experimental multinuclear solid-state NMR investigation of amino acids. *J Phys Chem A* **2005**, *109* (31), 6960-9.
35. Gervais, C.; Profeta, M.; Lafond, V.; Bonhomme, C.; Azais, T.; Mutin, H.; Pickard, C. J.; Mauri, F.; Babonneau, F., Combined ab initio computational and experimental multinuclear solid-state magnetic resonance study of phenylphosphonic acid. *Magn Reson Chem* **2004**, *42* (5), 445-52.
36. Arena, G.; Impellizzeri, G.; Maccarrone, G.; Pappalardo, G.; Sciotto, D.; Rizzarelli, E., Thermodynamic and ¹H NMR study of proton complex formation of histidine-containing cyclodipeptides in aqueous solution. *J Chem Soc Perkin trans* **1992**, (3), 371-376.
37. Bujdak, J.; Eder, A.; Yongyai, Y.; Faybikova, K.; Rode, B. M., Investigation on the mechanism of peptide chain prolongation on montmorillonite. *J Inorg Biochem* **1996**, *61* (1), 69-78.
38. Heyda, J.; Mason, P. E.; Jungwirth, P., Attractive Interactions between Side Chains of Histidine-Histidine and Histidine-Arginine-Based Cationic Dipeptides in Water. *J Phys Chem B* **2010**, *114*, 8744-8749.
39. Zyablov, A. N.; Baidicheva, O. V.; Kalach, A. V.; Selemenev, V. F., The Activation Energies of Viscous Flow and Diffusion Coefficients of Dipeptides and Amino Acids in Aqueous Solutions. *Russ J Phys Chem A* **2008**, *82* (2), 312-314.
40. Wishart, D. S.; Guo, A.; Oler, E.; Wang, F.; Anjum, A.; Peters, H.; Dizon, R.; Sayeeda, Z.; Tian, S.; Lee, B. L.; Berjanskii, M.; Mah, R.; Yamamoto, M.; Jovel, J.; Torres-

Calzada, C.; Hiebert-Giesbrecht, M.; Lui, V. W.; Varshavi, D.; Varshavi, D.; Allen, D.; Arndt, D.; Khetarpal, N.; Sivakumaran, A.; Harford, K.; Sanford, S.; Yee, K.; Cao, X.; Budinski, Z.; Liigand, J.; Zhang, L.; Zheng, J.; Mandal, R.; Karu, N.; Dambrova, M.; Schiöth, H. B.; Greiner, R.; Gautam, V., HMDB 5.0: the Human Metabolome Database for 2022. *Nucleic Acids Res* **2022**, *50* (D1), D622-d631.

41. Donohue, J.; Lavine, L. R.; Rollett, J. S., The crystal-structure of histidine hydrochloride monohydrate. *Acta Cryst* **1956**, *9*, 655-662.

42. Ben Ahmed, A.; Feki, H.; Abid, Y.; Boughzala, H.; Minot, C., Crystal studies, vibrational spectra and non-linear optical properties of L-histidine chloride monohydrate. *Spectrochim Acta A Mol Biomol Spectrosc* **2010**, *75* (1), 293-8.

43. Guo, C.; Holland, G. P., Investigating Lysine Adsorption on Fumed Silica Nanoparticles. *J Phys Chem C* **2014**, *118* (44), 25792-25801.

44. Mudunkotuwa, I. A.; Grassian, V. H., Histidine adsorption on TiO₂ nanoparticles: an integrated spectroscopic, thermodynamic, and molecular-based approach toward understanding nano-bio interactions. *Langmuir* **2014**, *30* (29), 8751-60.

Chapter 5

Future direction in prebiotic systems

Introduction

The work presented in this dissertation is aimed at developing techniques for high-resolution surface characterization of amorphous, dynamic systems and applying them to prebiotic models. Many types of natural and synthetic silica morphologies were analyzed, and FSN was found to be the best surface for catalyzing thermal condensation reactions of amino acids but there are still many other amorphous, glassy silica types that should be explored. This work has demonstrated that polymerization on the surface of silica is possible using only thermal exposure, and that low amounts of metal-dopant have little effect on amino acid adsorption and thermal condensation, even when the metal is incorporated near the surface (Chapter 3). The thermal decomposition of several prebiotic amino acids on FSN surfaces were analyzed by TGA (Chapter 4), and the following conclusions are drawn.

First, the side chain moiety has a large impact on adsorption. R-groups containing amines provide additional potential binding sites and interact with the SiO^- surface well. R-groups containing alcohols do not bind favorably and no indication of polymerization is observed through TGA. Non-polar amino acids display simple, characteristic decomposition profiles with a single thermal event in the thermal condensation region, and likely only bind to the surface through one contact point. Both positively and negatively charged R-groups have unique, convoluted thermal events and likely interact with the surface through a combination of contact points. Second, the protonation state of the amino acid during adsorption plays a large role in molecular assembly. His thermal events varied depending on the protonation state during adsorption, and it is reasonable to assume that protonation state would have a large effect on assembly for other charged amino acids. The protonation state directs molecular assembly, which then influences the progression of thermal condensation reactions and polymerization. Third, the substrate which also acts as the catalytic

agent is equally important in predicting the success of thermal condensation reactions (**Figure 5.1**). To promote these reactions, the substrate should have a large surface area and high hydroxyl content. Porosity was demonstrated to facilitate thermal condensation reactions, as evidenced by a shift to lower peak maximum temperatures (T_{\max}) on MSN/ala likely due to confinement and forced molecular interactions inside the pores (**Figure 5.1**). Many natural silica morphologies are porous and may facilitate thermal condensation reactions in a similar manner. Any material that contains ROS will likely promote these reactions as well, as we saw with FSN.

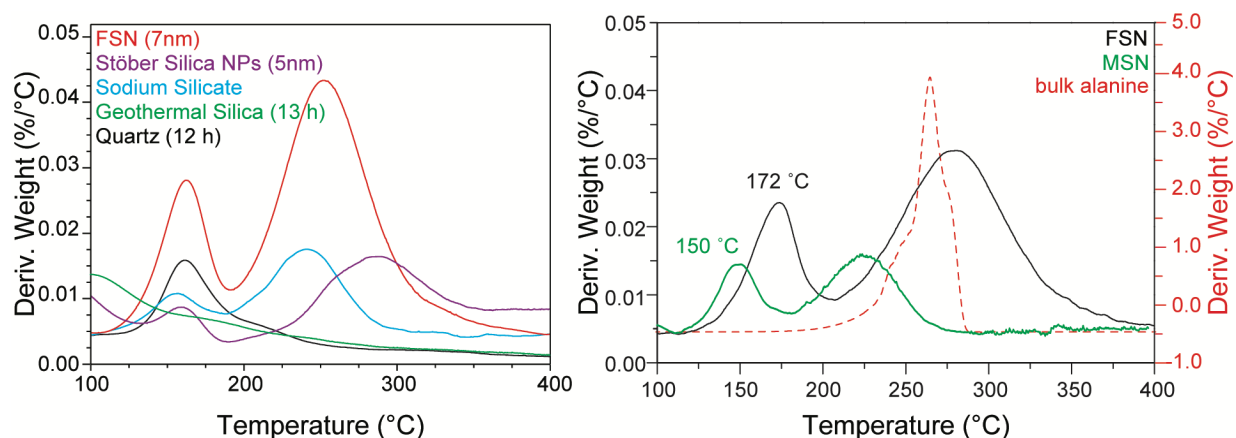


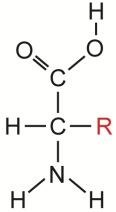
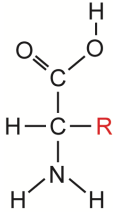
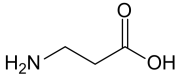
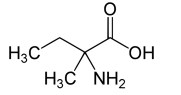
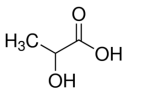
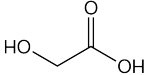
Figure 5.1. DTG of L-ala adsorbed on various silica substrates at 0.05M concentration. Geothermal silica and quartz were ball-milled for the number of hours in parenthesis.

This dissertation contributed to our fundamental understanding of thermal condensation reactions of amino acids on silica nanostructured surfaces. The future direction of this research should apply these findings to model prebiotic systems of increasing complexity. Notable contributions in origins of life research to increase oligomerization on metal oxide surfaces include

the use of wet/dry cycles,¹ ester-bond mediation,^{2, 3} binary mixtures,^{4, 5} and α -hydroxyacids or β -amino acids.⁶ The chronology of biogenic amino acids should also be considered when designing experiments.⁷ **Table 5.1** outlines a reasonable list of starting ligands, based on the information above. While FSN has proven to be the most reactive, other surfaces including glassy silica and porous silica should also be investigated.

The following project proposes an excellent starting place for any student wishing to continue this work. β -alanine is considered a prebiotic, non-biogenic amino acid that has been found in similar concentrations to L-alanine and glycine as produced in the Miller-Urey experiments and found in carbonaceous chondrites. β -ala has shown evidence of linear polymerization, in contrast to many other amino acids that preferentially form the DKP product. Preliminary results of a simple equimolar mixture of β -ala and L-ala are shared below to analyze if β -ala deters L-ala DKP formation and/or promotes the formation of heteropeptides. The techniques discussed below can be applied to investigate thermal condensation events of other binary systems adsorbed on silica surfaces.

Table 5.1. Prebiotic molecules to be investigated in future research (Y = Yes, N = No, R = Racemic).

Prebiotic Molecules	Biogenic	Present in Meteorites	Created in Miller-Urey Exp.	Molecular Structure
Glycine	Y	Y	Y	-H
D/L alanine	Y (L)	Y (R)	Y (R)	 -CH ₃
D/L aspartic acid	Y (L)	Y (R)	Y (R)	 -CH ₂ COOH
D/L glutamic acid	Y (L)	Y (R)	Y (R)	-(CH ₂) ₂ COOH
D/L valine	Y (L)	Y (R)	Y (?)	-CH(CH ₃) ₂
β-alanine	N	Y	Y	
D/L isovaline	N	Y (R)	Y (R)	
D/L Lactic acid	N	Y (?)	Y (?)	
Glycolic acid	N	Y	Y	

Experimental

Materials

FSN (~7 nm) with Brunauer, Emmett, and Teller (BET) surface area of $395 \pm 25 \text{ m}^2 \text{ g}^{-1}$ was purchased from Sigma-Aldrich. Natural abundance β-alanine (99%) and L-alanine (99%) were purchased from Fisher Scientific. Fully labeled U-[¹⁵N/¹³C]-β-alanine (98%) was purchased from Cambridge Isotope Laboratories, Inc. All materials were used as received.

Sample preparation

In a typical adsorption procedure, FSN were heated to 500 °C for at least 12 hours to activate the surface and remove impurities. Aqueous solutions of 0.03M β -ala or 0.03M β -ala and 0.03M L-ala were prepared at pH 6 in 25.0 mL aliquots using deionized millipore (DI) water. 375 mg FSN were added to the solution and the solution was stirred for 3 hr to facilitate amino acid adsorption. The samples were separated by centrifugation for 1 hr and the pellet was dried under vacuum at room temperature for no less than 48 hr. Isotopically enriched adsorptions were prepared using 5.00 mL aliquots and 75 mg FSN for SSNMR studies.

After drying, Ala/FSN adsorptions were homogenized into a fine powder and oligomerization was investigated through isothermal and cyclic heating procedures. In isothermal treatments, the samples were treated for 21 hr at 135 °C for β -ala or 140 °C for β /L-ala, washed and sonicated with DI water, and separated by centrifugation at 10k rpm for 1 hr. The solubilized peptide was collected, dried under vacuum, and resuspended in D₂O or 90:10 H₂O:D₂O for solution NMR analysis. Labeled adsorptions were heated in the MAS NMR rotor (uncapped) and analyzed with SSNMR immediately following thermal treatment prior to washing.

Lower temperatures were applied with repetitive thermal cycling using a Bio-Rad T100™ Thermal Cycler. The homogenized samples were placed in punctured PCR tubes to allow for ventilation and heated with a pre-programmed method. One cycle consisted of 12 hr at 90 °C and 12 hr at 25 °C. After 14 cycles, or two weeks, the adsorptions were removed from the surface by washing with DI water, sonicating, and centrifuging for 1 hr. The solubilized peptides were collected and dried under vacuum and resuspended in D₂O for solution NMR analysis. Labeled adsorptions were carefully packed into a rotor directly after the last cycle, capped, and analyzed with SSNMR prior to washing.

Solution NMR spectroscopy

Solution NMR experiments were performed with a 400 MHz Bruker Avance AV1 spectrometer equipped with a 5 mm H/X liquids probe. All samples were dissolved in 90:10 or 100% D₂O and referenced to a 10% DSS internal standard (0 ppm). ¹H 1D spectra were collected on 90:10 samples using nuclear Overhauser effect (NOE) transfer with pre-saturation during the recycle delay (d1) and mixing time to suppress water signals (Bruker pulse sequence noesypr1d or noesygppr1d). Typical acquisition parameters were 64 scans, 5 sec d1, 65k points, and 16 ppm spectral width (sw). Samples dissolved in 100% D₂O were analyzed with a simple ¹H pulse sequence with a 30° flip angle (Bruker, zg30), 16 scans, 5 sec d1, 65k points, and 20 ppm sw. Additional techniques were used for characterization of the thermal condensation product including ¹H – ¹³C heteronuclear single quantum correlation (HSQC), ¹H – ¹³C heteronuclear multiple bond correlation (HMBC), and ¹H – ¹H homonuclear correlation spectroscopy (COSY). ¹H – ¹³C HSQC (Bruker, hsqcedetgpsisp2.3 with bi_p5m4sp_4sp.2 decoupling) was collected with 32 or 64 scans, 1.5 sec d1, 2k points, 128 t1 points, and 14 ppm / 190 ppm sw in the direct/indirect dimensions. ¹H – ¹³C HMBC experiments (Bruker, hmbcgp12ndqf) were collected with 32 scans, 1.5 sec d1, 4k points, 200 complex t1 points, and 14 ppm / 240 ppm sw. ¹H – ¹H COSY (Bruker, cosygpqf) was collected with 8 or 64 scans, 1.5 sec d1, 2k points, 128 complex t1 points, and 14 ppm sw.

Solid-state NMR spectroscopy

SSNMR experiments were collected with a 600 MHz Bruker Avance IIIHD spectrometer equipped with a 1.9 mm triple resonance (¹H /¹³C/¹⁵N) probe with 30 kHz magic angle spinning (MAS). ¹³C Cross polarization experiments (CP-MAS) were collected using a 2.45 μs hard pulse

on ^1H , followed by a 2 ms ramped pulse (30%) with a radio frequency (rf) field strength of 118 kHz. Polarization transfer to ^{13}C was matched to the -1 Hartman Hann condition and ^1H decoupling at 115 kHz rf was applied during acquisition (Bruker, swftppm_13). A 5 sec d1, 300 ppm sw, and 4k scans were used. Spectra were processed with 50 Hz exponential line broadening and indirectly referenced to adamantane (^{13}C , 38.48 ppm).⁸ ^{15}N CP-MAS experiments were collected with initial ^1H $\pi/2$ pulse of 2.4 μs was applied followed by a 1.5 ms ramped pulse (30%) with a rf field strength of 103 kHz. Polarization transfer to ^{15}N was matched to the -1 Hartman Hann condition and high power ^1H decoupling at 117 kHz rf was applied during acquisition (Bruker, swftppm_13). A 3 sec d1 (5 sec in thermally treated samples), 400 ppm sw, and 4k scans were used. Spectra were processed with 100 Hz exponential line broadening and indirectly referenced to glycine (^{15}N , 31.6 ppm).⁹

Thermogravimetric analysis

TGA was conducted using a TA Instruments Q50 under steady N_2 (_g) flow (60 mL/min for furnace and 40 mL/min for balance). A sample mass of 10 – 15 mg was placed in the pan and equilibrated at room temperature under N_2 flow until a stable mass was reached. Data collection started at 25 °C and was heated at a rate of 5 °C/min to 600 °C. The first derivative (DTG) was applied to identify peak temperatures for each thermal transition using TA Universal Analysis software.

Results and Discussion

Thermal analysis

Many amino acids assembled on silica substrates condense to form peptide bonds after thermal treatment.^{1, 10-18} As discussed in the previous chapters, a DTG peak between 150 °C and 200 °C typically represents water loss from thermal condensation of neighboring amino acids. **Figure 5.2** shows DTG thermograms of L-ala/FSN, β -ala/FSN, and mixed β /L-ala/FSN adsorption complexes. The peak at 167 °C for L-ala/FSN is water loss from the formation of alanine anhydride, the diketopiperazine (DKP) product.¹⁹ The thermal condensation reaction occurs at \sim 30 °C lower temperature for β -ala/FSN with the thermal condensation reaction occurring at 139 °C. A shift to lower temperature indicates the reaction has a lower activation energy and occurs more readily. The thermal condensation peak is sharper and well resolved, which could indicate that β -ala adsorbs more uniformly on the FSN surface and the thermal condensation reaction occurs over a smaller temperature range.

L-ala forms DKP in nearly 99% efficiency after 3 hr thermal treatment at 170 °C.¹⁹ Both β /L-ala were adsorbed together from an equimolar mixture to investigate the possibility of heterogeneous peptide formation. The TC peak for the mixture appears at 144 °C (**Figure 5.2, grey**), between L-ala and β -ala TC peak maximums but shifted more towards β -ala. The degradation region displays a peak and broad shoulder that appear as a superposition of each individual amino acid. The mixture does not show individual thermal condensation events, but rather one TC event at 144 °C is observed which is close to the TC for the pure β -Ala adsorption. This illustrates that β -Ala has a large impact on L-Ala TC and is suggestive that the two amino acids couple during the TC event in the mixture.

A slower ramp rate (1 °C/min) was applied to deconvolute the degradation region. Slower temperature ramping causes T_{\max} to shift toward lower temperatures and increases resolution of areas that contain multiple thermal events. **Figure 5.3** shows that when a slower ramp is applied, the convoluted degradation region is clearly two distinct thermal events.

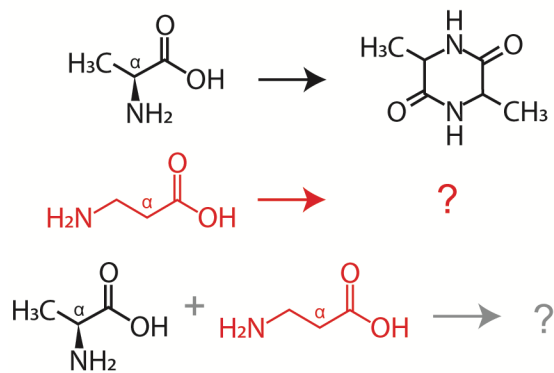
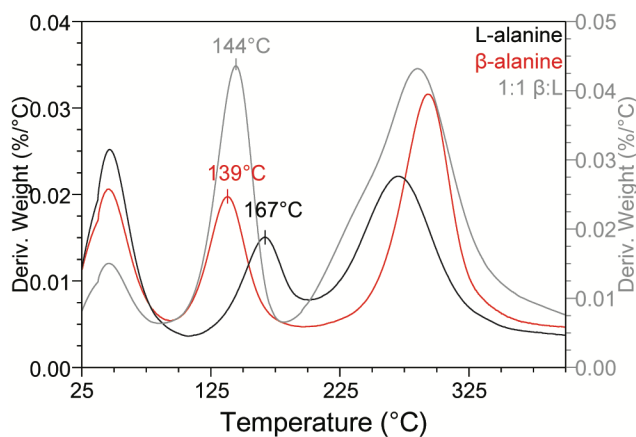


Figure 5.2. (top) DTG thermograms of β -ala/FSN-0.03M, L-ala/FSN-0.03M, and mixed (1:1) β /L-ala/FSN at 0.03M each. (bottom) Thermal condensation schemes of each reaction.

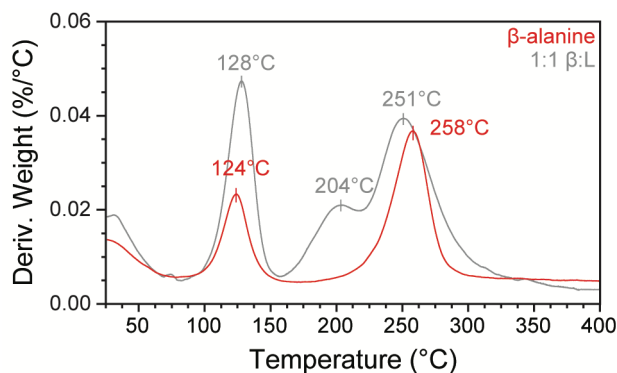


Figure 5.3. DTG thermograms using a slow (1 °C/min) ramp rate.

Adsorption and thermal condensation of β -ala/FSN

SSNMR experiments were performed on the adsorbed state before and after thermal treatment (**Figure 5.4**). C_{α} and C_{β} chemical environments are nearly equivalent and appear as a single resonance at 35.4 ppm in free β -ala. Adsorption to the FSN surface causes the electron density to shift due to the electron withdrawing effects of SiO^- interaction; C_{α} and C_{β} resonance are no longer chemically equivalent. A negligible chemical shift perturbation is observed for C' following adsorption on FSN compared to free β -ala. A small shift (<2 ppm) is observed in NH_2 after adsorption, likely from hydrogen bonding to the surface through this moiety.

Low temperature thermal treatment causes line broadening for all carbon sites and weak resonances become visible that are attributed to the formation of a peptide product. These weak resonances increase in population after higher temperature thermal treatment. After 135 °C/21 hr, C' and NH_2 groups are almost completely converted but the change is more apparent in ^{15}N CP-MAS where a clear change in chemical shift is observed as the chemical environment changes from free amine (~ 45 ppm) to peptide amide (~ 120 ppm). A small, broad resonance is still apparent in the amine region but is shifted downfield, which we attribute to the free amine terminus

of a linear peptide. All resonances broaden considerably after high temperature thermal treatment, which is commonly observed with ligands in “dry” environments due to reduced dynamics resulting in broadening due to chemical shift heterogeneity (a distribution in rigid binding environments at the interface).^{14, 20, 21}

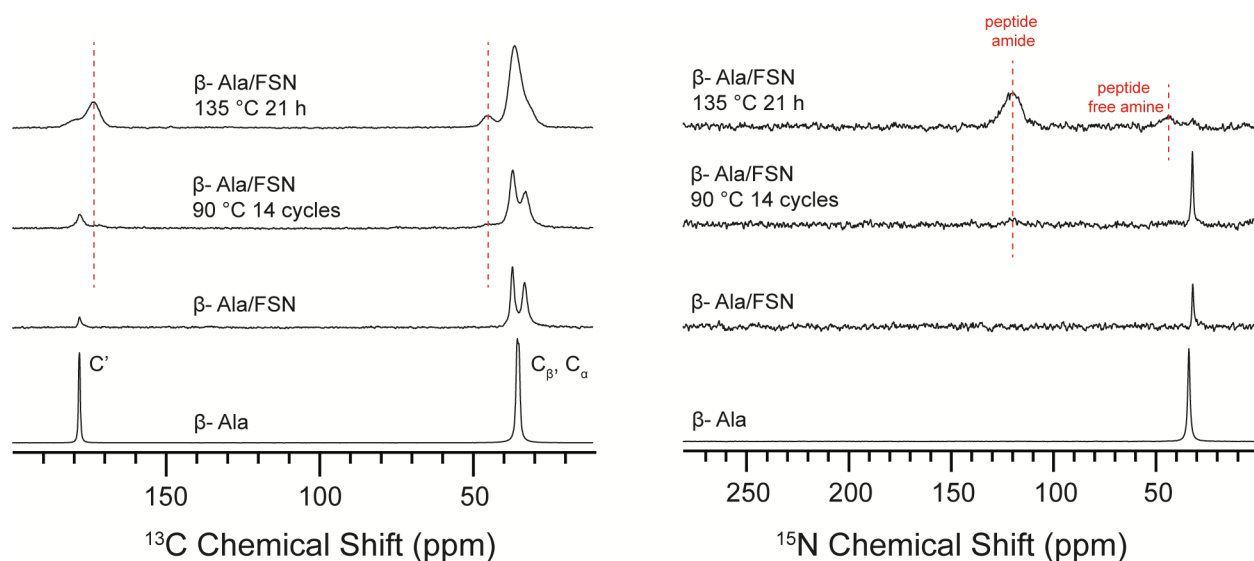


Figure 5.4. (left) ^{13}C and (right) ^{15}N CP-MAS NMR of free β -ala and FSN adsorptions before and after thermal treatments. Red dashed lines indicate the formation of peptide bonds.

Solution NMR experiments were performed to characterize the structure of the products after the high temperature thermal treatment where product yield was most favorable. Multiple 2-dimensional (2D) ^1H and ^{13}C correlation techniques were required for deconvolution as multiple populations are present even after high temperature thermal treatment. ^1H integration was also used to determine the total protons of the products in solution. A small population of unreacted β -ala, a small population of β -ala diketopiperazine (DKP), and the formation of β -ala tetramer were determined through $^1\text{H} - ^{13}\text{C}$ HSQC and $^1\text{H} - ^{13}\text{C}$ HMBC (**Figure 5.5**). This is a promising result

in origin of life research since it is difficult to overcome the kinetic and thermal stability of DKP which is the main product observed in thermal treatments of many biogenic amino acid on silica and alumina surfaces.^{10, 15-17, 19, 21, 22}

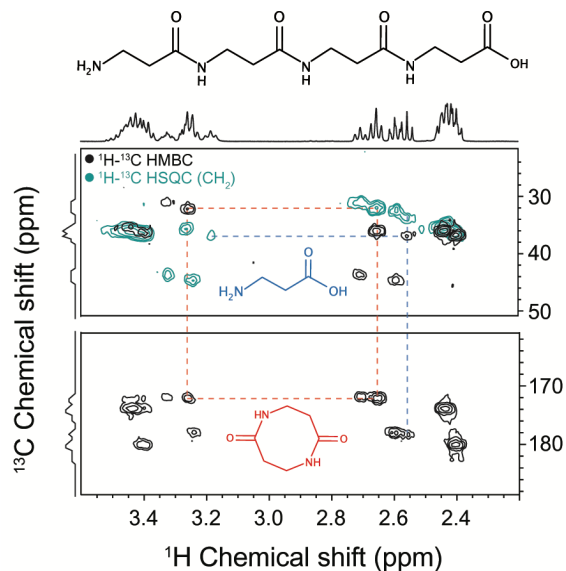


Figure 5.5. Multiplicity edited $^1\text{H} - ^{13}\text{C}$ HSQC and $^1\text{H} - ^{13}\text{C}$ HMBC 2D of β -ala/FSN after 135 °C/21 hr. The connectivity indicated by the red or blue dashed lines indicates the product in red or blue, respectively. Correlations not connected with dashed lines are from β -ala tetramer.

Adsorption and thermal condensation of β /L-ala/FSN mixtures

β /L-ala/FSN mixtures were characterized using similar techniques. Adsorption interactions were investigated using SSNMR and no changes were observed in the mixture compared to the individual amino acid adsorptions (**Figure 5.6**). This suggests that both amino acids are adsorbed, and no new resonances appear from intermolecular interactions. The total amino acid concentration of the mixture was 0.06M which is above the point of surface saturation so excess

free amino acid is expected as we saw in previous studies with L-Ala/FSN, L-Lys/FSN and L-His/FSN adsorptions.^{13, 14, 21} Excess L-ala is clearly present from the strong C_β resonance at 20.5 ppm in adsorbed and thermally treated states. The presence of excess β-ala is convoluted by C_α and C_β resonances of the adsorbed state but when exponential multiplication is turned off, ¹J_{CC} splitting is consistent in both samples at δ_C 35.4 ppm (~ 91 Hz) suggesting that free β-ala exists in the adsorbed mixture.

The chemical shift of L-ala C_β is well resolved across all samples shown in **Figure 5.6**, and residual free L-ala is clear even after thermal treatment at 140 °C/30 hr. Previous thermal condensation studies on this system have shown that FSN will catalyze the formation of L-ala DKP with ~99% efficiency after only 3 hr heating at 170 °C.¹⁹ The temperature used in this experiment was likely too low to induce L-ala DKP formation with high efficiency, and is likely the reason for residual free L-ala, despite prolonged thermal exposure. Negligible changes in chemical shift and line width are observed after low temperature thermal cycling, suggesting that little to no reaction occurred even after 2 weeks of repetitive exposure. All ¹³C and ¹⁵N resonances broaden considerably in the high temperature 140 °C/30 hr thermal treatment with full width at half maximum (FWHM) in the range of ~ 600-1000 Hz. This is likely due to a distribution of environments which results in chemical shift heterogeneity. The FWHM was within the same range for His sites upon removal of water layer,²¹ so large FWHM values do not conclusively indicate polymerization took place. However, the formation of a broad ¹⁵N resonance in the peptide amide region is clearly observed (~ 120 ppm) that does confirm the formation of peptide bonds.

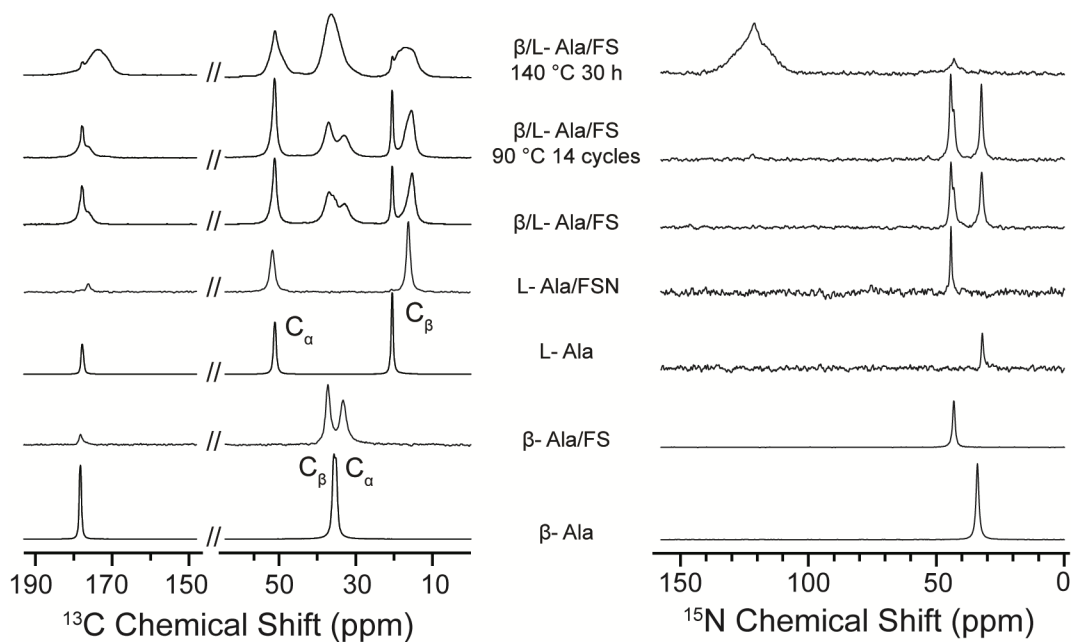


Figure 5.6. (left) ^{13}C and (right) ^{15}N CP-MAS of free β -ala and FSN adsorptions before and after thermal treatments.

Similarly, ^1H solution NMR of β /L-ala/FSN thermal condensation products are broadened considerably and contain trace amounts of unreacted L-ala and β -ala (**Figure 5.7**) L-ala DKP ^1H resonances are observed at 1.45 and 4.17 ppm in agreement with the literature,¹⁹ as well β -ala₄ groups at 2.43 and 3.43 ppm which indicate the presence of the linear peptide. Additionally, new ^1H resonances are observed at 1.33, 2.48, 3.92, and 4.58 ppm (**Figure 5.8**) so new products did form likely from the coupling of β - and L-ala but the secondary structure has yet to be determined. Further experiments are needed for complete structural analysis.

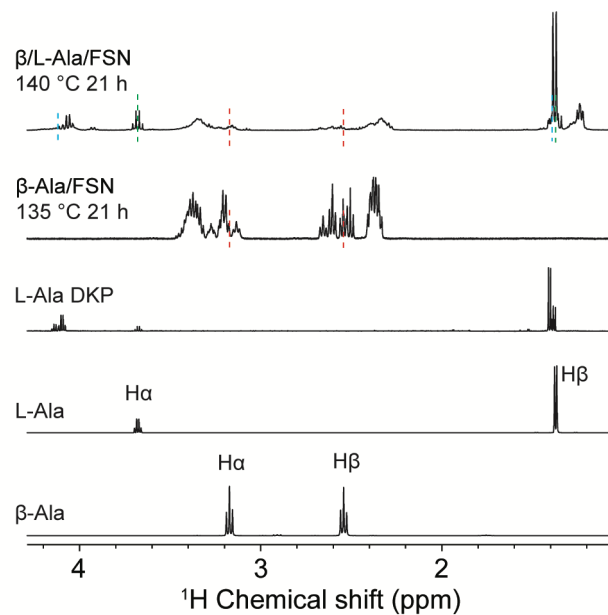


Figure 5.7. ^1H solution NMR of free β -ala, L-ala, L-ala DKP, and thermal condensation products formed from β -ala and β /L-ala adsorptions. Dashed lines indicate the chemical shifts of L-Ala DKP (blue), L-Ala (green), and β -Ala (red). β /L-Ala/FSN and L-Ala DKP were dissolved in D_2O , β -Ala/FSN, L-Ala, and β -Ala were dissolved in 90:10 $\text{H}_2\text{O}:\text{D}_2\text{O}$.

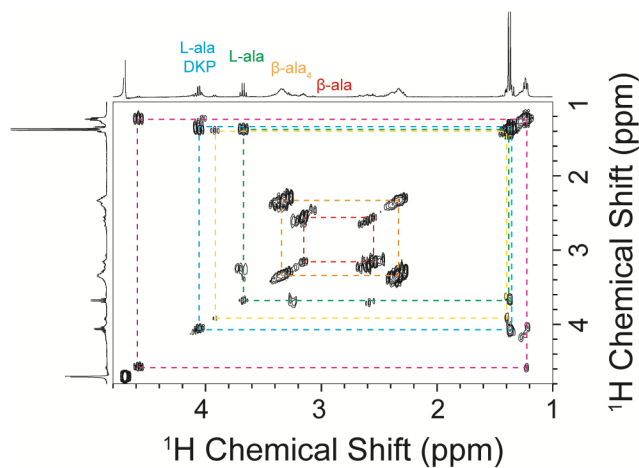


Figure 5.8. $^1\text{H} - ^1\text{H}$ COSY of β /L-ala/FSN after heating at $140\text{ }^\circ\text{C}/21\text{ hr}$. Pink and yellow dotted lines indicate new products.

Conclusions

β -ala/FSN characterizations were relatively straightforward. Binding was apparent from changes in chemical shifts and broadening in SSNMR spectra, and thermal condensation reactions at high and low temperature produced oligomerization up to β -ala₄. Simple solution NMR techniques were sufficient to characterize multiple components of β -ala/FSN thermal condensation. β /L-ala/FSN interactions were more difficult to characterize and any binding interaction between the two amino acids has yet to be determined. New ¹H resonances and correlations are observed in ¹H – ¹H COSY that are likely due to the coupling of β - and L-ala but further experiments are needed to comment on the structure. 2D solution NMR techniques can be applied to characterize the peptide product(s) although additional washing steps may be required to completely remove FSN from the peptide solution which is likely the source of a high degree of line broadening in **Figure 5.7**. 2D SSNMR techniques (¹³C – ¹³C dipolar assisted rotational resonance (DARR) with long contact times, ¹H – ¹³C – ¹⁵N double CP-MAS, and ¹H – ¹³C or ¹H – ¹⁵N heteronuclear correlation (HETCOR)) are recommended for interpreting molecular organization and perturbations for the thermally treated β /L-ala mixture.

This project provides preliminary results and demonstrates techniques to be used in future research projects. Solution and SSNMR offer complimentary pathways for characterizing the progression of polymerization reactions as they occur on surfaces, and analyzing the final structure of the peptide products. Together, they prove to be a valuable tool capable of identifying atomic-level interactions of molecular assembly on surfaces and the progression of thermally induced prebiotic chemical pathways.

Future directions

To continue the work started in this dissertation, it is recommended to start with the amino acids listed in **Table 5.1**. Once the individual amino acids and the thermal condensation products have been characterized (including longer thermal cycling possibly up to 12 weeks) binary mixtures should be investigated. Surprisingly less work has been done on investigating the polymerization of enantiomeric mixtures of amino acids on mineral oxide surfaces. The Miller-Urey experiments^{23, 24} and rigorous analysis of meteorite composition by Pizzarello et al²⁵⁻²⁹ have identified that amino acids were present in racemic mixtures in many prebiotic conditions. Separation and characterization of enantiomeric mixtures can be difficult since they have the same physical properties, but this work could potentially be high impact especially if the substrate is found to direct enantiomeric selection.

Other possible directions for future research are briefly listed here. The tertiary structure of the peptides formed by thermal condensation reactions, to the best of our knowledge, have not been investigated and could provide valuable insight to biological complexity. SSNMR paired with DFT modeling are suitable tools for studying tertiary structures. $^{13}\text{C} - ^{13}\text{C}$ through-space DARR and double quantum/single quantum (DQ/SQ) Incredible Natural Abundance Double QUAntum (INADEQUATE) through-bond methods can be used to determine peptide backbone folding at the interface from conformational dependent isotropic chemical shifts.³⁰⁻³⁵ $^1\text{H} - ^{13}\text{C}$ and $^1\text{H} - ^{15}\text{N}$ HETCOR techniques with ultra-fast MAS and proton-detection³⁶ can be used to probe hydrogen-bonding strength of amino acids and peptides at interfaces.³⁷ In addition to 3D structural analysis, peptide dynamics on nanostructured surfaces can be investigated with 2D $^2\text{H} - ^{13}\text{C}$ MAS methods which have been developed and pioneered by other members in our research group.³⁸⁻⁴⁰

Ultraviolet (UV) radiation could also be used as an alternative stimulus to drive oligomerization. Cosmic radiation would have been much stronger before the formation of the ozone layer. UV radiation has been shown to generate amino acids in laboratory simulations of icy interstellar analogues.^{41, 42} More recently, UV and pressure has been shown to polymerize D/L alanine into a linear dimer an order of magnitude more than the DKP formation.⁴³ Including an additional stimulus would provide a more comprehensive review of prebiotic polymerization on silica surfaces.

Lastly, we suggest an investigation of amino acids and/or peptides adsorbed on silica surfaces with fatty acids or simple lipids. Lipid membranes are an essential component of complex organisms today and will readily assemble on silica surfaces, independent of silica morphology.⁴⁴⁻
⁴⁶ Chemical and biological evolution would not have developed to its fullest extent without encapsulation and compartmentalization. Interestingly, fatty acids membranes are made more stable in the presence of prebiotic amino acids.⁴⁷ A myriad of experiments can be designed in this arena by varying amino acids, lipid composition, co- vs sequential adsorption, thermal treatments, wet/dry cycles, etc and provides an additional avenue with potential for high-impact results.

Acknowledgements

Haley L. Swanson would like to acknowledge support from NASA Fellowship 80NSSC19K0064. Many thanks to Dr. Lynn Rothschild for the spirited scientific discussion and guidance. The author would also like to acknowledge Dr. David Onofrei for help with NMR instrumentation. This chapter contains data that is unpublished.

References

1. Lahav, N.; White, D.; Chang, S., Peptide formation in the prebiotic era: thermal condensation of glycine in fluctuating clay environments. *Science* **1978**, *201* (4350), 67-9.
2. Forsythe, J. G.; Yu, S. S.; Mamajanov, I.; Grover, M. A.; Krishnamurthy, R.; Fernandez, F. M.; Hud, N. V., Ester-Mediated Amide Bond Formation Driven by Wet-Dry Cycles: A Possible Path to Polypeptides on the Prebiotic Earth. *Angew Chem Int Ed* **2015**, *54* (34), 9871-5.
3. McKee, A. D.; Solano, M.; Saydjari, A.; Bennett, C. J.; Hud, N. V.; Orlando, T. M., A Possible Path to Prebiotic Peptides Involving Silica and Hydroxy Acid-Mediated Amide Bond Formation. *Chembiochem* **2018**, *19* (18), 1913-1917.
4. Sakhno, Y.; Battistella, A.; Mezzetti, A.; Jaber, M.; Georgelin, T.; Michot, L.; Lambert, J. F., One Step up the Ladder of Prebiotic Complexity: Formation of Nonrandom Linear Polypeptides from Binary Systems of Amino Acids on Silica. *Chemistry* **2019**, *25* (5), 1275-1285.
5. Bujdák, J.; Rode, B. M., Preferential amino acid sequences in alumina-catalyzed peptide bond formation. *J Inorg Biochem* **2002**, *90*, 1-7.
6. Frenkel-Pinter, M.; Jacobson, K. C.; Eskew-Martin, J.; Forsythe, J. G.; Grover, M. A.; Williams, L. D.; Hud, N. V., Differential Oligomerization of Alpha versus Beta Amino Acids and Hydroxy Acids in Abiotic Proto-Peptide Synthesis Reactions. *Life (Basel)* **2022**, *12* (2).
7. Trifonov, E. N., The triplet code from first principles. *J Biomol Struct Dyn* **2004**, *22* (1), 1-11.
8. Morcombe, C. R.; Zilm, K. W., Chemical shift referencing in MAS solid state NMR. *J Magn Reson* **2003**, *162* (2), 479-86.
9. Hayashi, S.; Hayamizu, K., Chemical Shift Standards in High-Resolution Solid-State NMR (2) ¹⁵N Nuclei. *Bull Chem Soc Jpn* **1991**, *64* (2), 688-690.
10. Basiuk, V. A., Condensation of vaporous amino acids in the presence of silica. Formation of bi- and tricyclic amidines. *Orig Life Evol Biosph* **1992**, *22* (6), 333-48.
11. Bouchoucha, M.; Jaber, M.; Onfroy, T.; Lambert, J.-F.; Xue, B., Glutamic Acid Adsorption and Transformations on Silica. *J Phys Chem C* **2011**, *115* (44), 21813-21825.
12. Bujdak, J.; Eder, A.; Yongyai, Y.; Faybikova, K.; Rode, B. M., Investigation on the mechanism of peptide chain prolongation on montmorillonite. *J Inorg Biochem* **1996**, *61* (1), 69-78.
13. Guo, C.; Holland, G. P., Investigating Lysine Adsorption on Fumed Silica Nanoparticles. *J Phys Chem C* **2014**, *118* (44), 25792-25801.

14. Guo, C.; Holland, G. P., Alanine Adsorption and Thermal Condensation at the Interface of Fumed Silica Nanoparticles: A Solid-State NMR Investigation. *J Phys Chem C* **2015**, *119* (45), 25663-25672.
15. Lambert, J. F., Adsorption and polymerization of amino acids on mineral surfaces: a review. *Orig Life Evol Biosph* **2008**, *38* (3), 211-42.
16. Lambert, J. F.; Jaber, M.; Georgelin, T.; Stievano, L., A comparative study of the catalysis of peptide bond formation by oxide surfaces. *Phys Chem Chem Phys* **2013**, *15* (32), 13371-80.
17. Meng, M.; Stievano, L.; Lambert, J.-F., Adsorption and Thermal Condensation Mechanisms of Amino Acids on Oxide Supports. 1. Glycine on Silica. *Langmuir* **2004**, *20* (22), 914-923.
18. Ying, J.; Lin, R.; Xu, P.; Wu, Y.; Liu, Y.; Zhao, Y., Prebiotic formation of cyclic dipeptides under potentially early Earth conditions. *Sci Rep* **2018**, *8* (1), 936.
19. Guo, C.; Jordan, J. S.; Yarger, J. L.; Holland, G. P., Highly Efficient Fumed Silica Nanoparticles for Peptide Bond Formation: Converting Alanine to Alanine Anhydride. *ACS Appl Mater Interfaces* **2017**, *9* (20), 17653-17661.
20. Ben Shir, I.; Kababya, S.; Schmidt, A., Molecular Details of Amorphous Silica Surfaces Determine Binding Specificity to Small Amino Acids. *J Phys Chem C* **2014**, *118* (15), 7901-7909.
21. Swanson, H. L.; Guo, C.; Cao, M.; Addison, J. B.; Holland, G. P., Probing the binding modes and dynamics of histidine on fumed silica surfaces by solid-state NMR. *Phys Chem Chem Phys* **2020**, *22* (36), 20349-20361.
22. Fuchida, S.; Masuda, H.; Shinoda, K., Peptide formation mechanism on montmorillonite under thermal conditions. *Orig Life Evol Biosph* **2014**, *44* (1), 13-28.
23. Bada, J. L., New insights into prebiotic chemistry from Stanley Miller's spark discharge experiments. *Chem Soc Rev* **2013**, *42* (5), 2186-96.
24. Miller, S. L.; Urey, H. C., Organic compound synthesis on the primitive earth. *Science* **1959**, *130* (3370), 245-51.
25. Pizzarello, S., The Chemistry of Life's Origin: a Carbonaceous Meteorite Perspective. *Acc Chem Res* **2006**, *39* (4), 231-7.
26. Pizzarello, S.; Cooper, G. W.; Flynn, G. J., The nature and distribution of organic material in carbonaceous chondrites and interplanetary dust particles. *Meteorites and the Early Solar System II*.
27. Pizzarello, S.; Cronin, J. R., Alanine enantiomers in the Murchison meteorite. *Nature* **1998**, *394* (6690), 236.

28. Pizzarello, S.; Huang, Y.; Alexandre, M. R., Molecular asymmetry in extraterrestrial chemistry: Insights from a pristine meteorite. *Proc Natl Acad Sci U S A* **2008**, *105* (10), 3700-4.
29. Pizzarello, S.; Shock, E., The organic composition of carbonaceous meteorites: the evolutionary story ahead of biochemistry. *Cold Spring Harb Perspect Biol* **2010**, *2* (3), a002105.
30. Holland, G. P.; Creager, M. S.; Jenkins, J. E.; Lewis, R. V.; Yarger, J. L., Determining Secondary Structure in Spider Dragline Silk by Carbon-Carbon Correlation Solid-state NMR Spectroscopy. *J. Am. Chem. Soc.* **2008**, *130* (30), 9871-9877.
31. Holland, G. P.; Jenkins, J. E.; Creager, M. S.; Lewis, R. V.; Yarger, J. L., Quantifying the Fraction of Glycine and Alanine in β -sheet and Helical Conformations in Spider Dragline Silk using Solid-state NMR. *Chem. Commun.* **2008**, (43), 5568-5570.
32. Izdebski, T.; Akhenblit, P.; Jenkins, J. E.; Yarger, J. L.; Holland, G. P., Structure and Dynamics of Aromatic Residues in Spider Silk: 2D Carbon Correlation NMR of Dragline Fibers. *Biomacromolecules* **2010**, *11* (1), 168-174.
33. Jenkins, J. E.; Creager, M. S.; Butler, E. B.; Lewis, R. V.; Yarger, J. L.; Holland, G. P., Solid-state NMR evidence for elastin-like beta-turn structure in spider dragline silk. *Chemical Communications* **2010**, *46* (36), 6714-6716.
34. Jenkins, J. E.; Creager, M. S.; Lewis, R. V.; Holland, G. P.; Yarger, J. L., Quantitative Correlation between the Protein Primary Sequences and Secondary Structures in Spider Dragline Silks. *Biomacromolecules* **2010**, *11* (1), 192-200.
35. Jenkins, J. E.; Sampath, S.; Butler, E.; Kim, J.; Henning, R. W.; Holland, G. P.; Yarger, J. L., Characterizing the secondary protein structure of black widow dragline silk using solid-state NMR and X-ray diffraction. *Biomacromolecules* **2013**, *14* (10), 3472-83.
36. Holland, G. P.; Cherry, B. R.; Jenkins, J. E.; Yarger, J. L., Proton-detected heteronuclear single quantum correlation NMR spectroscopy in rigid solids with ultra-fast MAS. *Journal of Magnetic Resonance* **2010**, *202* (1), 64-71.
37. Holland, G. P.; Mou, Q.; Yarger, J. L., Determining hydrogen-bond interactions in spider silk with ^1H - ^{13}C HETCOR fast MAS solid-state NMR and DFT proton chemical shift calculations. *Chem Commun (Camb)* **2013**, *49* (59), 6680-2.
38. Shi, X.; Yarger, J. L.; Holland, G. P., Elucidating proline dynamics in spider dragline silk fibre using ^2H - ^{13}C HETCOR MAS NMR. *Chem Commun (Camb)* **2014**, *50* (37), 4856-9.
39. Shi, X. Y.; Yarger, J. L.; Holland, G. P., ^1H - ^{13}C HETCOR MAS NMR for indirect detection of ^1H -2 quadrupole patterns and spin-lattice relaxation rates. *Journal of Magnetic Resonance* **2013**, *226*, 1-12.

40. Shi, X.; Holland, G. P.; Yarger, J. L., Molecular dynamics of spider dragline silk fiber investigated by 2H MAS NMR. *Biomacromolecules* **2015**, *16* (3), 852-9.
41. Bernstein, M. P.; Dworkin, J. P.; Sandford, S. A.; Cooper, G. W.; Allamandola, L. J., Racemic amino acids from the ultraviolet photolysis of interstellar ice analogues. *Nature* **2002**, *416* (6879), 401-403.
42. Muñoz Caro, G. M.; Meierhenrich, U. J.; Schutte, W. A.; Barbier, B.; Segovia, A. A.; Rosenbauer, H.; Thiemann, W. H.-P.; Brack, A.; Greenberg, J. M., Amino acids from ultraviolet irradiation of interstellar ice analogues. *Nature* **2002**, 403-406.
43. Sugahara, H.; Mimura, K., Peptide synthesis triggered by comet impacts: A possible method for peptide delivery to the early Earth and icy satellites. *Icarus* **2015**, *257*, 103-112.
44. Joemetsa, S.; Spustova, K.; Kustanovich, K.; Ainla, A.; Schindler, S.; Eigler, S.; Lobovkina, T.; Lara-Avila, S.; Jesorka, A.; Gozen, I., Molecular Lipid Films on Microengineering Materials. *Langmuir* **2019**, *35* (32), 10286-10298.
45. Koksals, E. S.; Liese, S.; Kantarci, I.; Olsson, R.; Carlson, A.; Gozen, I., Nanotube-Mediated Path to Protocell Formation. *ACS Nano* **2019**, *13* (6), 6867-6878.
46. Mornet, S.; Lambert, O.; Duguet, E.; Brisson, A., The formation of supported lipid bilayers on silica nanoparticles revealed by cryoelectron microscopy. *Nano Lett* **2005**, *5* (2), 281-5.
47. Cornell, C. E.; Black, R. A.; Xue, M.; Litz, H. E.; Ramsay, A.; Gordon, M.; Mileant, A.; Cohen, Z. R.; Williams, J. A.; Lee, K. K.; Drobny, G. P.; Keller, S. L., Prebiotic amino acids bind to and stabilize prebiotic fatty acid membranes. *Proc Natl Acad Sci USA* **2019**, *116* (35), 17239-17244.